

QUASAR STRUCTURE FROM MICROLENSING IN  
GRAVITATIONALLY LENSED QUASARS

DISSERTATION

Presented in Partial Fulfillment of the Requirements for  
the Degree Doctor of Philosophy in the  
Graduate School of The Ohio State University

By

Christopher Warren Morgan

\*\*\*\*\*

The Ohio State University

2008

Dissertation Committee:

Christopher S. Kochanek, Adviser

Darren L. DePoy

Andrew Gould

Approved by

---

Adviser

Astronomy Graduate Program

## ABSTRACT

I analyze microlensing in gravitationally lensed quasars to yield measurements of the structure of their continuum emission regions. I first describe our lensed quasar monitoring program and RETROCAM, the auxiliary port camera I built for the 2.4m Hiltner telescope to monitor lensed quasars.

I describe the application of our Monte Carlo microlensing analysis technique to SDSS 0924+0219, a system with a highly anomalous optical flux ratio. For an inclination angle  $i$ , I find an optical scale radius  $\log[(r_s/\text{cm})\sqrt{\cos i/0.5}] = 14.8^{+0.3}_{-0.4}$ . I extrapolate the best-fitting light curves into the future to find a roughly 45% probability that the anomalous image (D) will brighten by at least an order of magnitude during the next decade.

I expand our method to make simultaneous estimates of the time delays and structure of HE1104–1805 and QJ0158–4325, two doubly-imaged quasars with microlensing and intrinsic variability on comparable time scales. For HE1104–1805 I find a time delay of  $\Delta t_{AB} = t_A - t_B = 162.2^{+6.3}_{-5.9}$  days and estimate a scale radius of  $\log[(r_s/\text{cm})\sqrt{\cos i/0.5}] = 15.7^{+0.4}_{-0.5}$  at  $0.2\mu\text{m}$  in the rest frame. I

am unable to measure a time delay for QJ0158–4325, but the scale radius is  $\log[(r_s/\text{cm})\sqrt{\cos i/0.5}] = 14.9 \pm 0.3$  at  $0.3\mu\text{m}$  in the rest frame.

I then apply our Monte Carlo microlensing analysis technique to the optical light curves of 11 lensed quasar systems to show that quasar accretion disk sizes at  $2500\text{\AA}$  are related to black hole mass ( $M_{BH}$ ) by  $\log(R_{2500}/\text{cm}) = (15.7 \pm 0.16) + (0.64 \pm 0.18) \log(M_{BH}/10^9 M_\odot)$ . This scaling is consistent with the expectation from thin disk theory ( $R \propto M_{BH}^{2/3}$ ), but it implies that black holes radiate with relatively low efficiency,  $\log(\eta) = -1.54 \pm 0.36 + \log(L/L_E)$  where  $\eta = L/(\dot{M}c^2)$ . These sizes are also larger, by a factor of  $\sim 3$ , than the size needed to produce the observed  $0.8\mu\text{m}$  quasar flux by thermal radiation from a thin disk with the same  $T \propto R^{-3/4}$  temperature profile.

Finally, I analyze the microlensing of the X-ray and optical emission of the lensed quasar PG 1115+080. I find that the effective radius of the X-ray emission is  $1.3_{-0.5}^{+1.1}$  dex smaller than that of the optical emission. I find a weak trend supporting models with low stellar mass fractions near the lensed images in mild contradiction to inferences from the stellar velocity dispersion and the time delays.

For Caleb, Charlotte and, especially, Luke...

## ACKNOWLEDGMENTS

I wish to thank my wife Christy for her love and support during this difficult but very rich phase of our lives. Many others would have given up on me a long time ago, but she has always supported my dream. Asking her to marry me was the best decision I've ever made - I could not imagine a better life partner.

I'm very thankful to my parents, Ed and Judy Morgan, for encouraging my interest in astronomy as a boy. Now that I am a parent myself, it is clear to me that the home environment I enjoyed as a child has everything to do with my current success. I am very grateful for their enabling influence.

I humbly acknowledge the profound influence of Evan Gnam, a friend of mine from my undergraduate years at Vanderbilt. He invested countless hours helping me through problem sets, challenging my opinions and vetting my thought process. Following his example, I set my own academic goals very high. I can say with full confidence that I would not be where I am today without his influence in my life. My undergraduate adviser, Richard Haglund, also deserves recognition for his patient instruction and guidance.

My mother-in-law, Judy Cellio, worked tirelessly to support my family after the birth of our first child, Caleb. Many people are forced to put family plans on hold (or give them up entirely) in favor of their academic careers. She permitted us to do both simultaneously; I will be grateful for this for the rest of my life.

Chris Kochanek has been an exceptional adviser. I came to graduate school after seven years in the U.S. Navy, so I spent the first few years searching for the science that interested me. Chris gave me direction, and he was willing to let me work on (and sometimes screw up) top-tier problems, rather than forcing me to labor in obscurity during the learning phase. I am also very thankful to him for continuing to work with me after my move to Annapolis. It would be my great honor to continue to be associated with Chris Kochanek.

At Ohio State, I'm also very thankful to Rick Pogge, Darren DePoy, Andy Gould and Nick Morgan. All of them made irreplaceable contributions to my graduate education. It simply wouldn't have happened without them. At the U.S. Naval Academy, Jeff Larsen, Elise Albert and Daryl Hartley have been very supportive. To my non-scientist friends in Columbus and Annapolis, thanks for asking nice questions about my brand of science and this inscrutable document.

## VITA

August 25, 1973 ..... Born – Bridgeport, CT, USA

1995 ..... B.S. Physics, Vanderbilt University

2005 ..... M.S. Astronomy,  
The Ohio State University

2002 – 2005 ..... Graduate Research Associate,  
The Ohio State University

2002 – 2003 ..... Distinguished University Fellow,  
The Ohio State University

2003 – 2004 ..... Price Instrumentation Fellow,  
Department of Astronomy,  
The Ohio State University

2005 – 2008 ..... Master Instructor, Department of Physics,  
United States Naval Academy

## PUBLICATIONS

### Research Publications

1. C.W Morgan, M.E. Eyler, C.S. Kochanek, N.D. Morgan and E.E. Falco,  
“Simultaneous Estimation of Time Delays and Quasar Structure”, *ApJ*, 676, 80,  
(2008)
2. J. Yoo, J. Miralda-Escudé, D.H. Weinberg, Z. Zheng, and C.W Morgan,  
“The Most Massive Black Holes in the Universe: Effects of Mergers in Massive  
Galaxy Clusters”, *ApJ*, 662, 62, (2007)

3. J. Fohlmeister, C.S. Kochanek, E.E. Falco, J. Wambsganss, N.D. Morgan, C.W. Morgan, E.O. Ofek, D. Maoz, C.R. Keeton, J.C. Barentine, G. Dalton, J. Demibicky, W. Ketzebach, R. McMillan and C.S. Peters, “A Time Delay for the Cluster–Lensed Quasar SDSS J1004+4112”, *ApJ*, 662, 62, (2007)
4. C.W. Morgan, C.S. Kochanek, N.D. Morgan and E.E. Falco, “Microlensing of the Lensed Quasar SDSS0924+0219”, *ApJ*, 647, 874, (2006).
5. C.W. Morgan, P.L. Byard, D.L. DePoy, M. Derwent, C.S. Kochanek, J.L. Marshall, T.P. O’Brien and R.W. Pogge, “RETROCAM: A Versatile Optical Imager for Synoptic Studies”, *AJ*, 129, 2504, (2005).
6. D.L. DePoy, B. Atwood, S.R. Belville, D.F. Brewer, P.L. Byard, M. Derwent, J.L. Marshall, J.A. Mason, C.W. Morgan, T.P. O’Brien, P.S. Osmer, D.P. Pappalardo, R.W. Pogge, D.P. Steinbrecher, E.J. Teiga and D.H. Weinberg, “A Multiple–Object Double Spectrograph for the Large Binocular Telescope”, *SPIE*, 5492, 452, (2004)
7. A. Gould and C.W. Morgan, “Transit Target Selections Using Reduced Proper Motions”, *ApJ*, 585, 1056, (2003).

## FIELDS OF STUDY

Major Field: Astronomy

## TABLE OF CONTENTS

Abstract . . . . .	ii
Dedication . . . . .	iv
Acknowledgments . . . . .	v
Vita . . . . .	vii
List of Tables . . . . .	xii
List of Figures . . . . .	xiv
<b>Chapter 1 Introduction . . . . .</b>	<b>1</b>
1.1 Quasars and Gravitational Lensing . . . . .	1
1.2 Relation to Previous Work . . . . .	5
1.3 Scope of the Dissertation . . . . .	8
<b>Chapter 2 The Retractable Optical Camera for Monitoring (RETROCAM) . . . . .</b>	<b>12</b>
2.1 Motivation . . . . .	12
2.2 RETROCAM Specifications and Configuration . . . . .	14
2.2.1 Optomechanical Design . . . . .	14
2.2.2 Data Acquisition and Instrument Control Software . . . . .	17
2.3 Performance and Usage . . . . .	19
2.3.1 Commissioning and Testing . . . . .	19
2.3.2 Sample Results . . . . .	21

2.4	Conclusions and Discussion . . . . .	22
<b>Chapter 3 Microlensing of the Lensed Quasar SDSS 0924+0219 . .</b>		<b>31</b>
3.1	Introduction . . . . .	31
3.2	HST Observations and Mass Models . . . . .	34
3.2.1	HST Observations . . . . .	34
3.2.2	Macro Models and Substructure . . . . .	37
3.3	Microlensing . . . . .	39
3.3.1	Monitoring Data and Microlensing . . . . .	39
3.3.2	Microlensing Models . . . . .	41
3.3.3	Quasar Structure . . . . .	45
3.3.4	Expectations for the Future Behavior of SDSS0924+0219 . . .	49
3.4	Conclusions . . . . .	50
<b>Chapter 4 Simultaneous Estimation of Time Delays and Quasar Structure . . . . .</b>		<b>69</b>
4.1	Introduction . . . . .	69
4.2	Observations and Models . . . . .	72
4.3	Joint Monte Carlo Analysis . . . . .	75
4.4	Results . . . . .	77
4.5	Discussion and Conclusions . . . . .	81
<b>Chapter 5 The Quasar Accretion Disk Size – Black Hole Mass Relation</b>		<b>96</b>
5.1	Introduction . . . . .	96
5.2	Data and Analysis . . . . .	98
5.3	Results . . . . .	102

5.4	Discussion . . . . .	106
<b>Chapter 6 X-Ray and Optical Microlensing in the Lensed Quasar PG 1115+080 . . . . . 113</b>		
6.1	Introduction . . . . .	113
6.2	<i>Hubble Space Telescope</i> Observations, <i>Chandra</i> and Optical Monitoring Data . . . . .	117
6.3	Microlensing Models . . . . .	119
6.4	Results and Discussion . . . . .	124
<b>Chapter 7 Prospects for Future Work . . . . . 139</b>		
7.1	Multi-wavelength Monitoring and Quasar Emission Profiles . . . . .	139
7.2	The Structure of Quasar X-Ray Emission Regions . . . . .	140
7.3	The Mass Profiles of Lens Galaxies . . . . .	141
<b>Bibliography . . . . .</b>		<b>142</b>

## LIST OF TABLES

3.1	HST Astrometry and Photometry of SDSS0924+0219 . . . . .	63
3.2	Macroscopic Lens Mass Models . . . . .	64
3.3	SDSS 0924+0219 Light curves . . . . .	65
3.3	SDSS 0924+0219 Light curves . . . . .	66
3.3	SDSS 0924+0219 Light curves . . . . .	67
3.3	SDSS 0924+0219 Light curves . . . . .	68
4.1	QJ0158–4325 Light curves . . . . .	89
4.1	QJ0158–4325 Light curves . . . . .	90
4.1	QJ0158–4325 Light curves . . . . .	91
4.1	QJ0158–4325 Light curves . . . . .	92
4.1	QJ0158–4325 Light curves . . . . .	93
4.2	HST Astrometry and Photometry of QJ0158–4325 and HE1104–1805	94
4.3	Lens Galaxy Mass Models . . . . .	95
5.1	Measured and Derived Quantities . . . . .	112
6.1	HST Astrometry and Photometry of PG1115+080 . . . . .	133
6.2	PG1115+080 Lens Galaxy Mass Models . . . . .	134
6.3	PG1115+080 Optical Light Curves . . . . .	135
6.3	PG1115+080 Optical Light Curves . . . . .	136
6.3	PG1115+080 Optical Light Curves . . . . .	137

6.3 PG1115+080 Optical Light Curves . . . . .	138
---	-----

## LIST OF FIGURES

1.1	Example magnification pattern - QJ0158–4325 image B (1 of 1). . . .	11
2.1	RETROCAM schematic (1 of 7). . . . .	24
2.2	MIS and RETROCAM prism configuration (2 of 7). . . . .	25
2.3	RETROCAM external configuration (3 of 7). . . . .	26
2.4	The RETROCAM Graphical User Interface (GUI) (4 of 7). . . . .	27
2.5	RETROCAM flatness histogram (5 of 7). . . . .	28
2.6	Sample image: NGC 7714/7715 (6 of 7). . . . .	29
2.7	Sample image: Q 01420–100 (7 of 7). . . . .	30
3.1	<i>HST</i> <i>H</i> -band image (1 of 11). . . . .	52
3.2	Substructure model (2 of 11). . . . .	53
3.3	Substructure model (3 of 11). . . . .	54
3.4	<i>R</i> -band lightcurves (4 of 11). . . . .	55
3.5	Five best fits to lightcurve data (5 of 11). . . . .	56
3.6	Effective source plane velocity distribution (6 of 11). . . . .	57
3.7	Average stellar mass $\langle M \rangle$ distribution (7 of 11). . . . .	58
3.8	Constraints on $M_{BH}$ and $\dot{M}$ (8 of 11). . . . .	59
3.9	Scaled source size $\hat{r}_s$ distribution (9 of 11). . . . .	60
3.10	Source size $r_s$ distribution (10 of 11). . . . .	61
3.11	Future behavior of SDSS 0924+0219 (11 of 11). . . . .	62

4.1	QJ 0158–4325 $R$ -band lightcurves and best fit (1 of 6) . . . . .	83
4.2	Time delay of HE 1104–1805 (2 of 6) . . . . .	84
4.3	Source size $r_s$ probability distribution for HE 1104–1805 (3 of 6) . . . .	85
4.4	QJ 0158–4325 time delay probability distribution - limited extrapolation (4 of 6) . . . . .	86
4.5	QJ 0158–4325 time delay probability distribution - unlimited extrapolation (5 of 6) . . . . .	87
4.6	Source size $r_s$ probability distribution for QJ 0158–4325 (6 of 6) . . . .	88
5.1	Inclination-corrected accretion disk size $R_{2500}$ versus black hole mass $M_{BH}$ (1 of 3) . . . . .	109
5.2	Results of power-law fit to $R_{2500}$ and $M_{BH}$ (2 of 3) . . . . .	110
5.3	Thin disk flux size estimates vs. microlensing size estimates (3 of 3) . .	111
6.1	PG 1115+080 optical and X-ray flux ratios and best fit (1 of 5) . . . .	128
6.2	Continuation of Fig.6.1 (2 of 5) . . . . .	129
6.3	Probability distribution for PG 1115+080 optical/X-ray source size ratios (3 of 5) . . . . .	130
6.4	PG 1115+080 X-ray and optical continuum source sizes (4 of 5) . . . .	131
6.5	Probability distribution for $f_{M/L}$ (5 of 5) . . . . .	132

# CHAPTER 1

## INTRODUCTION

### 1.1. QUASARS AND GRAVITATIONAL LENSING

Since Maarten Schmidt's (1963) discovery of the high-redshift nature of quasars a half century ago, an enormous effort has been made to understand quasar accretion disk physics. Nevertheless, the Shakura & Sunyaev (1973) thin disk model and its variants continue to be used regularly, despite a large number of more sophisticated alternatives. It may be that the Shakura & Sunyaev (1973) model is used with such high frequency because of its analytical tractability, but much of its current usage can be attributed to lingering uncertainties about quasar accretion disks. In the era of their discovery, the nature of quasars caused much confusion because they were indistinguishable from point sources, hence "quasi-stellar" objects. Shortly following Schmidt's discovery, the time-variability of quasars began to be characterized, providing the first estimate of the physical size of quasar continuum emission regions. The luminosity of some quasars has been observed to vary significantly on timescales of days (or tens of days in some systems). This would imply a maximum size for the central engine of  $r_{max} \approx c\Delta t = 8 \times 10^{16}$  cm for  $\Delta t = 1$  month. Given

this relatively small physical size, the angular extent of a typical accretion disk is on micro-arcsecond ( $\mu\text{sec}$ ) scales, well below the angular resolution limit of any conventional telescopes.

Not all telescopes are conventional, however. In some rare cases nature has provided a phenomenon to probe these very small angular scales, gravitational lensing. Thanks to large-scale surveys such as the Sloan Digital Sky Survey (York et al. 2000), the number of positively identified quasars is now much larger than  $10^5$  and will continue to rise. Of these  $\sim 10^5$  known quasars, approximately 100 are known to be gravitationally lensed. I will use the remainder of this chapter to summarize the state of the field and to explain how we exploit this natural phenomenon to study the central engines of quasars. I conclude the chapter with a summary of the scope of this Dissertation.

If a point source of light, a point mass in free space (or any spherically symmetric mass distribution) and an observer are perfectly aligned, General Relativity (GR) predicts that the observer will see the light from the point source as a circle surrounding the point mass (the lens). This circle is commonly referred to as the ‘‘Einstein Ring’’, the angular radius of which is given by

$$\theta_E = \sqrt{\frac{4GM_{lens}}{c^2} \frac{D_{LS}}{D_{OL}D_{OS}}} \quad (1.1)$$

where  $D_{LS}$  is the distance from the lens to the source,  $D_{OL}$  is the distance from observer to lens and  $D_{OS}$  is the distance from observer to source. On cosmological scales, these distances become angular diameter distances. This simple model provides a context for understanding gravitationally lensed quasars, but in the case of quasars the distribution of mass in the lens is triaxial (asymmetric) and the alignment is never perfect. These differences lead to the formation of multiple images of the same source rather than a circular Einstein ring, although in many cases an elliptical Einstein ring from the quasar host galaxy is visible. Circular lens galaxy potentials lead to the formation of 2 images, and 4 image systems are the result of elliptical (or other non-circular) lens galaxy potentials. An additional very faint central image is expected in both cases but is rarely observed (Winn et al. 2004).

The intrinsic variability of quasars permits several useful measurements in gravitationally lensed systems. Differences in optical path length and gravitational time dilation from the potential of the lens galaxy cause the source variability to appear at different times in each image. A measurement of the time delay between the appearance of this variability in the multiple images can be used to simultaneously constrain the Hubble constant  $H_0$  (Refsdal 1964) and the distribution of dark matter in the lens galaxy (Kochanek 2005). The light rays of each image typically pass through some portion of the lens galaxy, often in the transition zone between the stellar-dominated inner regions and the dark matter halo. On their way through the galaxy, the photon trajectories are deflected by the gravitational fields

from individual stars and the smoothly distributed dark matter. If the source-plane projection of the Einstein radius of a lens galaxy star is of the same order or larger than the quasar continuum source, then the star is capable of temporarily magnifying (or de-magnifying) an image. Since relative motion exists between source, lens galaxy and observer, and the stars themselves have an orbital velocity dispersion about the center of the lens galaxy, the local magnification pattern changes and its source-plane projection moves as a function of time. Hence, we expect the flux of each quasar image to vary as the source crosses gradients in the magnification pattern. Unlike the intrinsic variability, however, microlensing variability is uncorrelated between images.

Given the stellar column density in a typical lens galaxy, each image can be magnified (or de-magnified) by the gravitational potential of many stars. Since we cannot resolve the stars in the vicinity of each image individually, we treat them statistically using magnification patterns. Using a variant of the ray-shooting technique (e.g. Schneider et al. 1992), we compute the source-plane projection of the combined magnification patterns from a physically plausible ensemble of lens galaxy stars. I show an example of a  $4096 \times 4096$  magnification pattern for image A of the lensed quasar QJ0158–4325 in Figure 1.1. This magnification pattern combines the effects of the gravitational potential from 135 stars and the global shear  $\gamma$  and convergence  $\kappa$  from the macroscopic (“strong”) lensing properties of the lens galaxy.

We have undertaken a lensed quasar monitoring campaign for  $\sim 30$  lensed quasars, motivated to measure time delays and to analyze the signal from microlensing. The monitoring data is valuable for a variety of other programs (e.g. peculiar velocity studies, galactic mass measurements, studies of galaxy evolution and the interstellar medium in lens galaxies), but it is the microlensing phenomenon I exploit for the majority of measurements reported in this dissertation. Since the timescale for microlensing and its amplitude depend on mass of stars in the lens galaxy, the size of the quasar emission source and relative velocities between the two, the observed microlensing signal can be analyzed to extract information about all three of these quantities. In this way, gravitational microlensing probes scales much smaller than the angular resolution limit of any conventional telescope.

## 1.2. RELATION TO PREVIOUS WORK

The deflection of light rays by gravitational fields was predicted by Einstein (1916), and was confirmed just three years later by astrometric observations of a background star near the limb of the sun during a solar eclipse (Dyson, Eddington & Davidson 1920). For most 20th century scientists, gravitational lensing was considered to be a powerful observable confirmation of GR, but its utility as a tool to study the universe was not put to use until the discovery of the first gravitationally lensed quasar (Walsh, Carswell & Weymann 1979).

At present, gravitational lensing is in use on Galactic and cosmological scales. Within the Galaxy, the MACHO project (Alcock et al. 1995, 2000) has constrained the properties of the dark matter halo by all but eliminating of the possibility of massive compact halo objects (MACHOs). OGLE (Udalski et al. 1997) has detected large numbers of microlensing events toward the Galactic bulge, and follow-up of these events has lead to discovery of extra-solar planets (e.g. Beaulieu et al. 2006; Gould et al. 2006).

The discovery of the first gravitationally lensed quasar (Walsh, Carswell & Weymann 1979), Q0957+561, marked the effective birth date of gravitational lensing as an separate astronomical community. Over the next twenty years, a few tens of lensed quasars were discovered, often serendipitously, as a part of independent small-scale surveys or during observational follow-up of catalogs of known quasars. However, it is large-scale surveys such as the Sloan Digital Sky Survey (SDSS) (York et al. 2000) and the Cosmic Lens All-Sky Survey (CLASS) (Browne et al. 2003; Myers et al. 2003) that have enabled the recent bloom in lensed quasar discoveries. To date, 100 lensed quasars are now known, and the list will continue to increase in length.

Historically, measuring time delays has been the primary motivation for monitoring lensed quasars. In fact, this remains one of the primary motivations for our lensed quasar monitoring program (see Kochanek et al. 2006, for a description),

but in this work we mainly concern ourselves with the use of quasar microlensing as a tool to study the properties of lens galaxies and quasar emission regions.

The potential for observing microlensing in Q 0957+561 was recognized immediately after its discovery by Chang & Refsdal (1979), and its usefulness as a probe of quasar structure was proposed shortly thereafter by Kayser, Refsdal & Stabell (1986). The first detection of quasar microlensing (Irwin et al. 1989), however, was in the lensed quasar Q 2237+0305 (Huchra et al. 1985). Given its unusual geometry (the lens galaxy is a low-redshift spiral), Q 2237+0305 has a short timescale for microlens caustic crossings ( $t_{cross} \approx 1$  year), making it a logical choice for a number of early monitoring campaigns and microlensing studies. In the first quantitative interpretations of a specific microlensing event, Wambsganss, Paczyński & Schneider (1990) and Rauch & Blandford (1991) used microlensing in two images of Q 2237+0305 to place an upper boundary on the optical size of that quasar’s accretion disk. Investigations of this system culminated with the introduction of Kochanek’s (2004) quantitative light curve microlensing analysis technique. Kochanek’s method employs a Monte Carlo lightcurve fitting routine which yields simultaneous measurements of the average mass star in the lens galaxy  $\langle M \rangle$  and the size of the quasar’s accretion disk at one or multiple wavelengths by Bayesian maximum likelihood analysis.

Mortonson et al. (2005) used a microlensing model to analyze the influence of different quasar emission profiles on microlensing, and they found that microlensing

effectively measures a disk's half-light radius and does little to discriminate between emission models. Recently, Keeton et al. (2006) used microlensing of the Broad Line Region (BLR) in SDSS 0924+0219 to place an upper boundary on the accretion disk size in SDSS0924+0219, and Pooley et al. (2006) used a comparison of anomalous X-ray and optical flux ratios to set a lower limit on the optical size of the accretion disk of PG 1115+080. Pooley et al. (2007) then applied a similar technique to a set of 10 quadruply lensed quasars to estimate the size of their optical emission regions. In all of these recent surveys, sizes estimated by microlensing seem to indicate quasar accretion disk sizes that are  $\sim 3 - 30$  times larger than the thin disk Shakura & Sunyaev (1973) sizes necessary to reproduce the observed fluxes. When compared to theoretical thin disk sizes as predicted by black hole mass, however, the microlensing estimates are marginally consistent.

### 1.3. SCOPE OF THE DISSERTATION

In Chapter 2, I discuss RETROCAM, the instrument I designed and built for our lensed quasar monitoring program, the data from which are used in the science described in the remaining chapters. In Chapter 3, I describe the application of our microlensing analysis technique to the lensed quasar with the most spectacular optical flux ratio anomaly, SDSS 0924+0219. I also predict the future behavior of this system, specifically the time frame over which I expect the flux ratios to

return to the value predicted by the macroscopic lens model. In Chapter 5, I use our microlensing analysis technique to attempt a time delay measurement in QJ 0158-4325, a system in which the microlensing is so severe that traditional polynomial fitting methods fail. I successfully test a joint Monte Carlo analysis technique on a system with a known delay, HE 1104-1805, to yield simultaneous time delay and accretion disk size estimates. I was unsuccessful in measuring the time delay of QJ0158-4325, but I was still able to measure to size of its accretion disk, nonetheless. In Chapter 5, I apply the microlensing analysis technique to 11 lensed quasars, and I find a strong correlation between accretion disk size at optical wavelengths and the mass of the central black hole. I find that the microlensing size measurements are marginally consistent with the predictions of thin disk theory (Shakura & Sunyaev 1973) for an Eddington-limited accretion disk radiating with 10% efficiency, but I confirm the findings of Pooley et al. (2007) and others that microlensing measurements of optical accretion disk sizes are  $\sim 0.3$  dex larger than sizes implied by their measured flux and thin disk theory. In Chapter 6, I complement the optical lightcurve of PG1115+080 with two epochs of X-ray data from the *Chandrasekhar X-Ray Observatory (Chandra)*, and I use our Monte Carlo analysis technique to simultaneously estimate the size of its optical and X-ray continuum emission regions. Finally, in Chapter 7, I discuss the prospects for future science from our ongoing lensed quasar monitoring campaign.

Chapter 2 has been published in *The Astronomical Journal* and chapters 3 and 4 have been published as individual articles in *The Astrophysical Journal*. Chapters 5 and 6 are manuscripts in the final stages of preparation for submission, but the results are preliminary. Final results will be published in *The Astrophysical Journal*.



Fig. 1.1.— Microlensing magnification pattern for image B of the lensed quasar QJ0158–4325 (4096x4096 pixels) for a stellar mass fraction  $\kappa_*/\kappa = 0.78$ . The magnification pattern displayed here has an outer scale of  $20\theta_E$ .

## CHAPTER 2

# THE RETRACTABLE OPTICAL CAMERA FOR MONITORING (RETROCAM)

### 2.1. MOTIVATION

In an era of 8 meter-class telescopes, the potential for smaller telescopes to make significant scientific contributions can easily be overlooked. In fact, many institutions are ending longstanding relationships with smaller observatories in favor of fewer numbers of nights at larger telescopes. It is clear, however, that dedicated programs on 1–2m class telescopes can still have enormous scientific impact either by conducting large homogeneous surveys such as the Sloan Digital Sky Survey (SDSS) (York et al. 2000) or by creative exploration of the time domain. In particular, large scale variability studies have enormous potential: Galactic microlensing studies such as MACHO (Alcock et al. 2000), EROS (Derue et al. 1999) and OGLE (Udalski et al. 1997) have placed constraints on the composition and structure of the galaxy. Dense time-sampling of gamma-ray burst (GRB) afterglows and supernovae has led to the likely conclusion that the GRB phenomenon is a by-product of supernova events (Matheson et al. 2003). The importance of variable star monitoring and its

influence on the cosmic distance scale (e.g. Alcock et al. 1995) is well known. Time delay measurements from monitoring multiply imaged quasars constrain the Hubble constant and the structure of galaxy halos in the important transition region between the baryon dominated inner regions and the dark matter dominated outer regions (Kochanek 2005). Additionally, the uncorrelated variability due to microlensing of the images can be used to constrain the fraction of the transition region surface mass density in stars, the mean mass of these stars and the size and structure of the quasar accretion disk (Kochanek 2004).

Rarely do programs of this type require an entire night of telescope time; in fact, many of these variability studies require less than one hour per night of observing time. Unfortunately, traditional scheduling and time-consuming instrument changes make it virtually impossible to pursue such programs at most observatories. Some observatories have overcome this problem with queue or remote observing, but most observatories have multiple primary instruments, some of which are spectrographs with no imaging capability. Hence, consistent synoptic surveys are difficult to accomplish. At some telescopes, the presence of auxiliary ports and bent foci have permitted relatively simple solutions to this problem. The Auxiliary Port Camera (AUX)<sup>1</sup> on the 4.2 meter William Herschel Telescope at La Palma is an excellent example of such a system.

---

<sup>1</sup>Additional information about AUX can be found at <http://www.ing.iac.es/Astronomy/instruments/aux/index.html>.

RETROCAM, the RETRactable Optical CAmera for Monitoring, is a solution to this problem for the MDM Observatory 2.4m Hiltner telescope. Its primary advantage is that it can be used concurrently with any of the observatory's spectrographs and all but one of its imagers. We initially undertook this project to build a camera for monitoring gravitationally lensed quasar systems, and we will demonstrate RETROCAM's suitability for this task. We will also show that it is capable of much more than this; the primary purpose for this paper is to discuss how RETROCAM's design and capabilities provide an enormous potential for a variety of exciting scientific programs.

## 2.2. RETROCAM SPECIFICATIONS AND CONFIGURATION

### 2.2.1. OPTOMECHANICAL DESIGN

RETROCAM is installed in the 2.4m Hiltner Telescope's Multiple Instrument System (MIS) at the MDM Observatory on Kitt Peak, Arizona. The MIS was originally conceived as a multi-function device to provide spectral calibration lamps, an intensified video finder camera, and an x-y stage for the telescope's autoguiding system camera. Our design preserved the comparison lamp and guider functions, and replaced the antiquated finder camera (a non-functioning intensified vidicon) with a science-quality imager whose quick readout time permits it to also serve as a finder camera, thus maintaining the full original functionality of the MIS and

greatly improving its sensitivity. The layout of the MIS and RETROCAM is shown in Figure 1. Light from the telescope is sent to RETROCAM by reflection from a reflective optic that travels into the telescope's beam along two rails. We suppress scattered light with a threaded baffle tube and field stop assembly. The light then passes through a filter wheel equipped with four filters (g,r,i, and z) from the SDSS set (Fukugita et al. 1996) and one open position.

RETROCAM uses an Apogee Instruments, Inc. Alta E-Series<sup>2</sup> CCD camera with the E2V CCD55-20 array. The CCD has  $22.5\mu\text{m}$  pixels in a  $1152\times 770$  array. When installed on the 2.4m Hiltner Telescope with the  $f/7.5$  secondary mirror, the pixel scale is  $0.259$  arcsec pixel<sup>-1</sup>. The array reads out in  $\sim 6$  sec with  $13.4$  e<sup>-</sup> pixel<sup>-1</sup> readout noise at a gain of  $3.0$  e<sup>-</sup> DN<sup>-1</sup>. The camera employs a two-stage Peltier Thermoelectric Cooler (TEC) capable of maintaining a differential temperature of  $45^\circ\text{C}$  with only ambient air cooling. The detector is normally maintained at  $-20.0 \pm 1^\circ\text{C}$  and operates with a dark current of  $2.5$  e<sup>-</sup> sec<sup>-1</sup> pixel<sup>-1</sup> at this temperature. At the sky brightness levels typically seen at MDM in the g,r,i and z bands, noise for all but the shortest exposures is dominated by the contribution from the night sky. The camera is mounted on a manually adjustable focusing mechanism that is not meant for frequent adjustment; the focus was adjusted during installation to conjugate the focus of the telescope's most commonly used spectrograph. The

---

<sup>2</sup><http://www.ccd.com/alta.html>

observer accomplishes precise focusing on a nightly basis using the telescope's secondary mirror.

As shown in Figures 2.1, 2.2 and 2.3, the “Finder” section of the MIS is located above the guider section. As a result, when the folding optic is in place it casts a shadow on a significant fraction of the guide field. In order to maintain the ability to guide during RETROCAM exposures, the folding optic was made as small as possible, preserving  $\sim 100$  arcmin<sup>2</sup> of available guide field that is vignetted by  $< 20\%$ . The original MIS design used the back of the finder mirror to reflect light from the calibration lamps into the spectrographs below. In order to preserve this function while removing the need for a bulky mounting frame, we selected a BK7 prism with an aluminized hypotenuse as our folding optic. The stiffness of the prism allows it to be mounted using the vertical face only. Light from the telescope reflects directly off of the aluminized surface, while light from calibration lamps is sent downward into the primary instrument via the prism's internal reflection path. A weakness of this design is that BK7 attenuates the calibration lamp light by  $\sim 40\%$  at  $4000\text{\AA}$  compared to the previous design, so longer comparison lamp exposure times are necessary. We consider this to be of minimal impact, given the relatively short times typically required for comparison lamp exposures. Spectral quality is otherwise unaffected.

RETROCAM's relatively small field of view greatly simplified the overall optical design. No field flattener or off-axis correction lenses were necessary to produce a design Strehl Ratio  $>70\%$  across the entire field of view.

## 2.2.2. DATA ACQUISITION AND INSTRUMENT CONTROL

### SOFTWARE

The Apogee Alta E-Series CCD camera uses an embedded 100-baseT network interface, which is connected directly to the MDM mountain network via a fiber-optic ethernet repeater mounted on the telescope. The filter wheel we use is an Optec, Inc.<sup>3</sup> Intelligent Filter Wheel (IFW). This filter wheel holds up to five 2-inch diameter filters, and can be operated remotely via an RS-232 serial port using a simple command language provided by Optec. We access this interface via a Control<sup>4</sup> DeviceMaster RTS 4-port network serial port server mounted directly on the MIS box, making the IFW a network-addressable device. We connect this to the mountain network using the same fiber repeater line that services the Alta CCD camera.

The data acquisition software for the Alta camera runs on a Linux workstation located in the 2.4-m control room. The user interface is a custom Tcl/Tk application that is based on a slightly modified version of Apogee drivers for Linux, using code

---

<sup>3</sup><http://www.optecinc.com/>

<sup>4</sup><http://www.control.com/>

provided by Dave Mills<sup>5</sup>. Our graphical user interface (GUI) is based on Mills' original `gui.tcl` script, but substantially modified to incorporate remote control of the Optec IFW filter wheel via the network port server, and to provide other RETROCAM-specific functions (e.g., TEC control). Data from RETROCAM are written to the hard drive on the Linux workstation in standard FITS format. The data acquisition system also provides a simple TCP-socket interface for remote command operation from other hosts. A screenshot of the beta-release version of the RETROCAM data acquisition GUI is shown in Figure 2.4. This version of the system is being used during the initial deployment phase, and will be updated based on user feedback from actual use at the telescope.

The RETROCAM data-acquisition system queries the 2.4m Telescope Control System for the relevant pointing information, and derives its UT time/date information from the data-acquisition computer's clock, which is synchronized with the Kitt Peak mountain network time server. The software is GUI-based but incorporates a simple scripting language, allowing sequenced focus offset and dithering commands to the Telescope Control System coupled with camera exposure sequences. This remote command capability permits a high degree of automation which in turn improves the efficiency of observations with RETROCAM.

---

<sup>5</sup>Version 1.1. See <http://sourceforge.net/projects/apogee-driver/> for the most recent version of Mills' driver.

## 2.3. PERFORMANCE AND USAGE

### 2.3.1. COMMISSIONING AND TESTING

RETROCAM was installed in August of 2004 and commissioned in September of 2004. We measured a total system (RETROCAM + telescope optics) throughput of 54% in the r band using the original Kodak CCD. In the r-band, the camera will register  $3.11 \times 10^5 \text{ e}^- \text{ sec}^{-1}$  from an  $r = 12.0$  magnitude star. When we replaced the front-side illuminated Kodak CCD is replaced by the thinned, back-illuminated E2V CCD, the efficiency improved by a factor of  $\sim 1.4$ .

We evaluated the flatness of the RETROCAM optical system (folding optic + filter + CCD) by measuring the system's response to the flux from a SDSS standard star (Smith et al. 2002) in a uniform 5x6 grid on the CCD. First, dark current and bias frames were subtracted from each exposure. Next, we measured the number of detected photons in each image using the Image Reduction and Analysis Facility (IRAF) *qphot* aperture photometry routine. We divided the standard deviation of this sample by the mean and found that  $\sigma_{sample}/\mu_{sample} = 0.0057$ . Hence, RETROCAM is flat to within 0.6% across the entire field of view without application of a flat field correction. Now, the expected value of  $\sigma_{sample}/\mu_{sample}$  due to photon flux Poisson noise is  $5.7 \times 10^{-4}$ , which is an order of magnitude smaller than what we find. However, it is unlikely that the common procedure of dividing

by a normalized flat field (sky or dome flat) will help us approach this theoretical flatness limit. For example, to reach within a factor of three of the theoretical limit, a flat field would need a  $S/N \approx 600$  and would need to have no systematic (scattered light, etc.) effects greater than  $\sim 0.1\%$ . Obtaining a flat field with such a high  $S/N$  and without systematic errors is quite difficult in practice. As a result, applying a standard flat field correction to RETROCAM images will likely introduce more error than it will remove.

We tested this flat field hypothesis by generating a night sky flat using median combination of a large number of equal length exposures. We normalized this flat and applied it to the SDSS standard star images. We then re-performed the measurement described above and found that  $\sigma_{sample}/\mu_{sample}$  increased to 0.011, an increase of nearly a factor of two. This effect is demonstrated graphically in Figure 2.5. Despite the relatively small number of data points (30), the histogram of the measurements before flattening is obviously narrower than the histogram of the flux measurements following application of the flat field. We assert that the remarkable flatness of the RETROCAM system is yet another quality which makes it an ideal detector for synoptic studies, since time-consuming flat field corrections will be unnecessary for most projects.

In the standard RETROCAM observing procedure, a primary observer uses the telescope with the instrument of their choice for the majority of the night. At a mutually convenient time, the on-site observer takes 15 minutes to reconfigure the

telescope and collect data for a dedicated RETROCAM monitoring project, then resumes where they left off with very little time lost to their own program. None of the settings of the primary instrument have been changed, allowing a rapid return to the primary observing plan. One complication to this simple plan is that not all primary instruments at the MDM 2.4m are parfocal. RETROCAM was installed and adjusted to be parfocal with the Boller and Chivens CCD spectrograph<sup>6</sup>. We have measured the secondary mirror focus offsets between RETROCAM and the other primary instruments at the observatory. A table of these offsets is provided to the observer to improve the efficiency of the focusing procedure. In an attempt to optimize the efficiency and accuracy of the lensed quasar monitoring project, future improvements to the RETROCAM control software will automate the insertion of the prism, focus offsets, guide star selection, image capture and system restoration.

### 2.3.2. SAMPLE RESULTS

An example of RETROCAM's high image quality is shown in Figure 2.6 - an image of NGC 7714/15 taken in the r band on 2004 August 25. The image of NGC 7714/15 ( $V = 13.3$  mag) was taken under 1.0 arcsec seeing conditions. Figure 2.7 shows an r band image of the gravitationally lensed quasar system Q01420-100 taken 2004 October 2 under 1.1 arcsec seeing conditions. The images are separated by 2.4

---

<sup>6</sup>More information about CCDS can be found at <http://www.astronomy.ohio-state.edu/MDM/CCDS/>.

arcsec. The brighter image has  $R \approx 16.6$  mag and the fainter image has  $R \approx 18.7$  mag. Diffuse light from the lens galaxy can be seen between the two images.

## 2.4. CONCLUSIONS AND DISCUSSION

This paper describes the RETROCAM instrument, and demonstrates that it is fully capable of executing the function for which it was designed, but we believe that it will reap returns far beyond lensed quasar monitoring. RETROCAM represents a significant improvement in the capabilities of the MDM observatory in the following ways: (1) It provides the capability to take science quality images and spectra of the same object on the same night. (2) It provides an imager which is nearly always available for targets of opportunity - supernovae, gamma ray bursts, microlensing events, etc. (3) Its field of view and performance are comparable to most of the direct imagers at the observatory. For many projects, RETROCAM could be used instead of these imagers, reducing the frequency of primary instrument changes and freeing the observatory staff for other activities. RETROCAM will not completely replace these other imagers since it cannot be easily outfitted with observer-supplied filters.

RETROCAM is currently in use for several variability studies. C. Morgan and Kochanek are monitoring a sample of gravitationally lensed quasar systems.

A. Gould is using RETROCAM to collect data for the Ångstrom Project<sup>7</sup>, a microlensing study of the M31 bulge. We expect that other members of the MDM consortium will begin other programs soon. RETROCAM represents an important step forward in the design and operational paradigms of the MDM Observatory. Its design could easily be reproduced at other observatories for relatively low cost. The availability of commercial “off the shelf” high quality CCD cameras with network capability has greatly simplified this task.

---

<sup>7</sup>More information on the Ångstrom Project can be found at <http://www.astro.livjm.ac.uk/Angstrom/>.

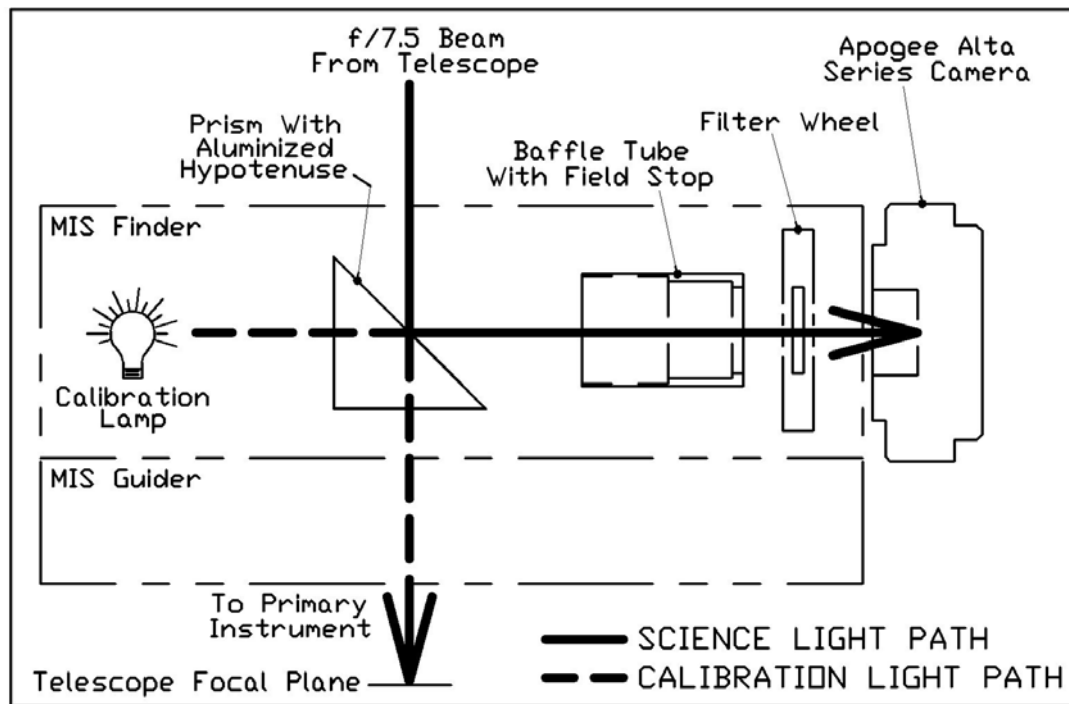


Fig. 2.1.— A schematic of the RETROCAM and Multiple Instrument System (MIS) optical paths. With the RETROCAM prism inserted, light from the telescope is reflected orthogonally into the camera. Light from MIS calibration lamps is directed to the primary instrument below via the prism's internal reflection path.

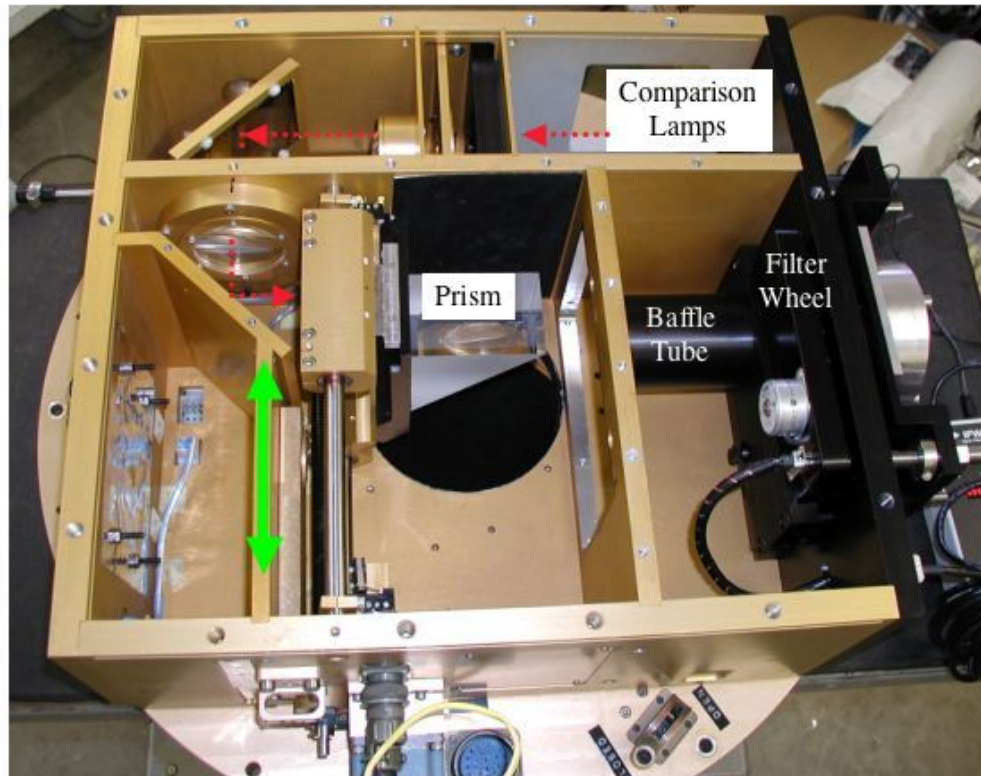


Fig. 2.2.— Upside-down internal photograph of the MIS finder section during RETROCAM installation. The prism is shown in the fully inserted position. The circular aperture beneath the prism allows light from the telescope to enter the MIS. The prism travels in and out of the optical beam along a set of stainless steel rails. The baffle tube and filter wheel assembly are fastened to the side wall of the MIS (right side of photo). Compartments in the top of the image house spectral comparison lamps and optics. The red line indicates the comparison lamp light path. The green arrow indicates prism's direction of motion.

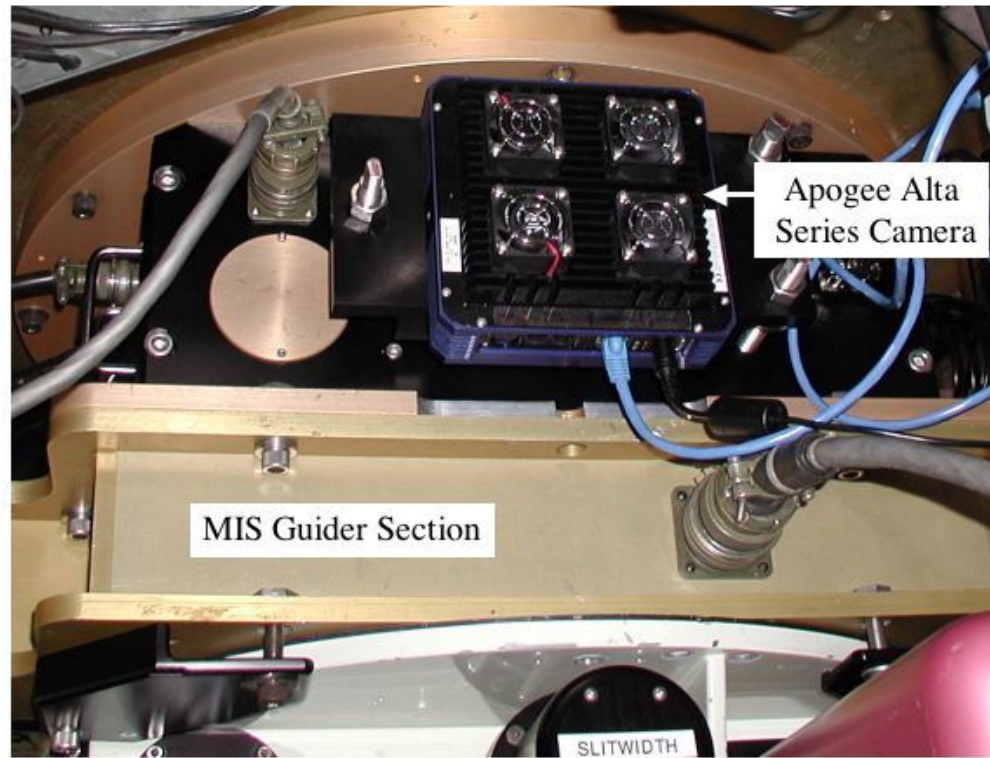


Fig. 2.3.— Right: Photograph of RETROCAM following installation on the 2.4m Hiltner telescope. The MIS guider is contained in the gold anodized section of the MIS located beneath the camera. The white painted structure at the bottom of the photograph is the Boller and Chivens CCD Spectrograph (CCDS).

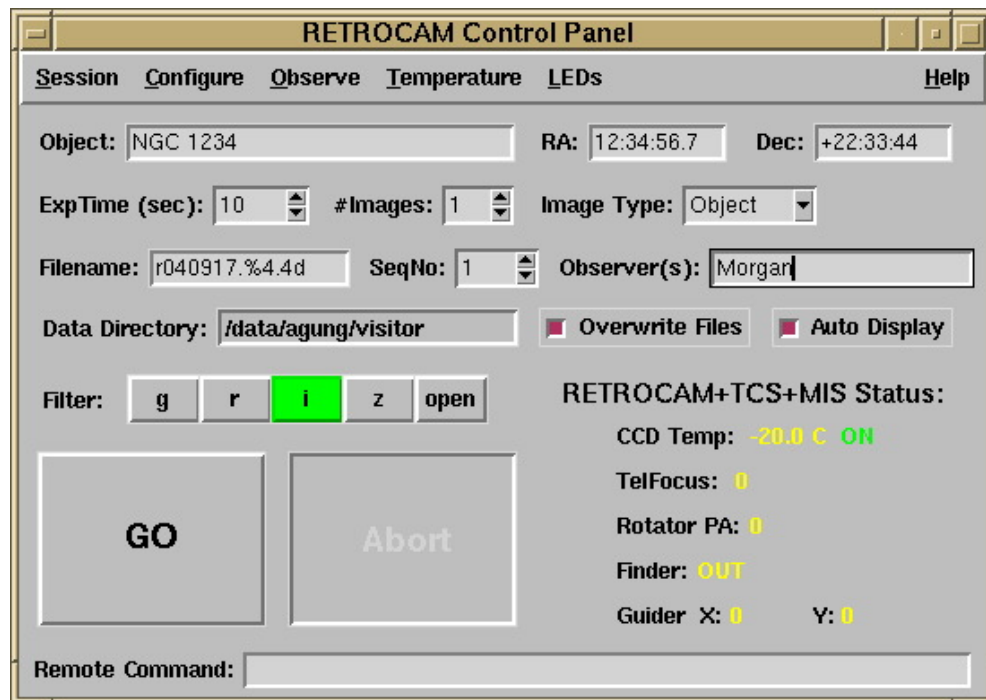


Fig. 2.4.— The RETROCAM Graphical User Interface (GUI).

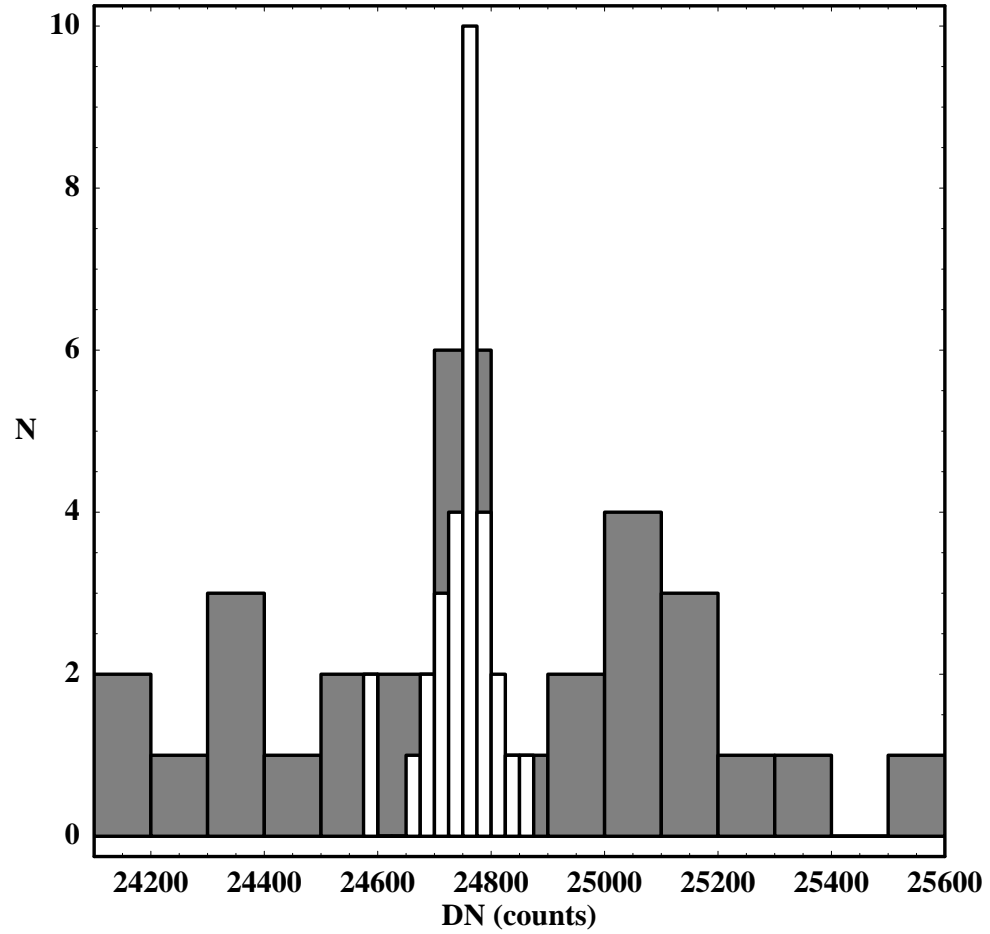


Fig. 2.5.— A histogram of photometric measurements of the SDSS standard star SA 113 339. Measurements were made at locations in a uniform 5x6 grid on the detector. White bars: the ensemble of aperture photometric measurements made prior to flat field correction. Gray bars: The ensemble of aperture photometric measurements following flat field correction.

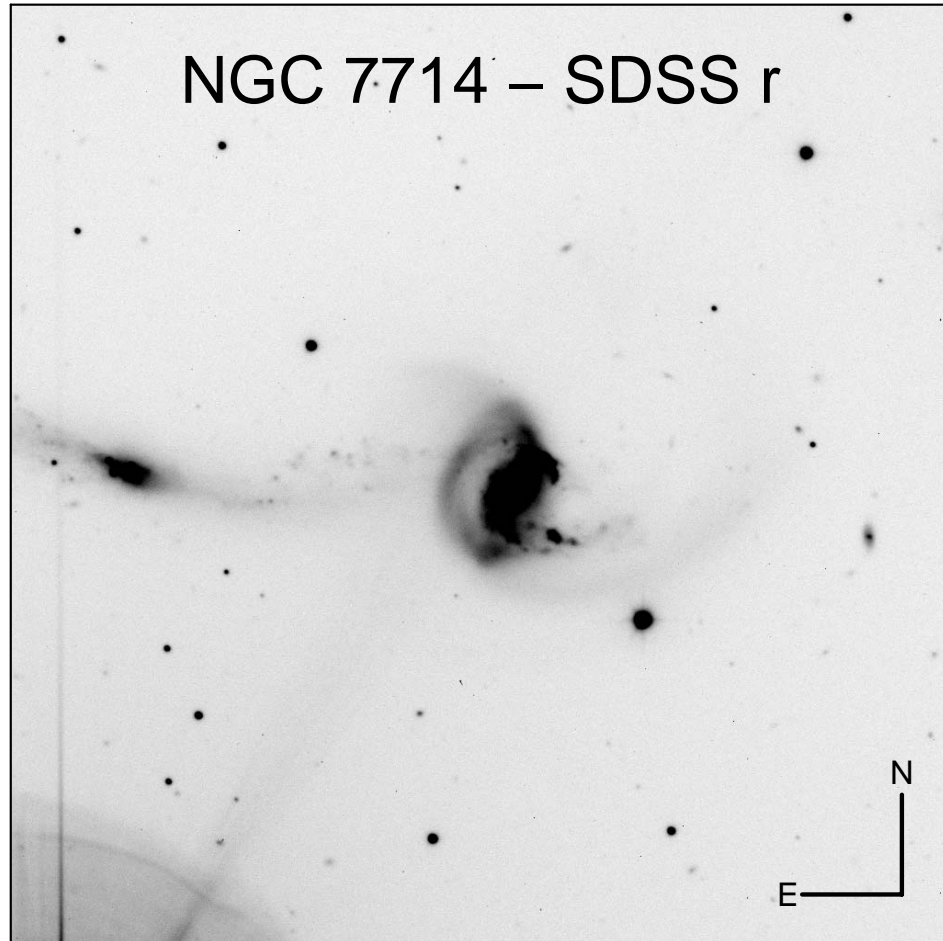


Fig. 2.6.— An SDSS r band image of NGC 7714 and NGC 7715 taken on 25 August 2004. Orientation axes are 30 arcsec in length.

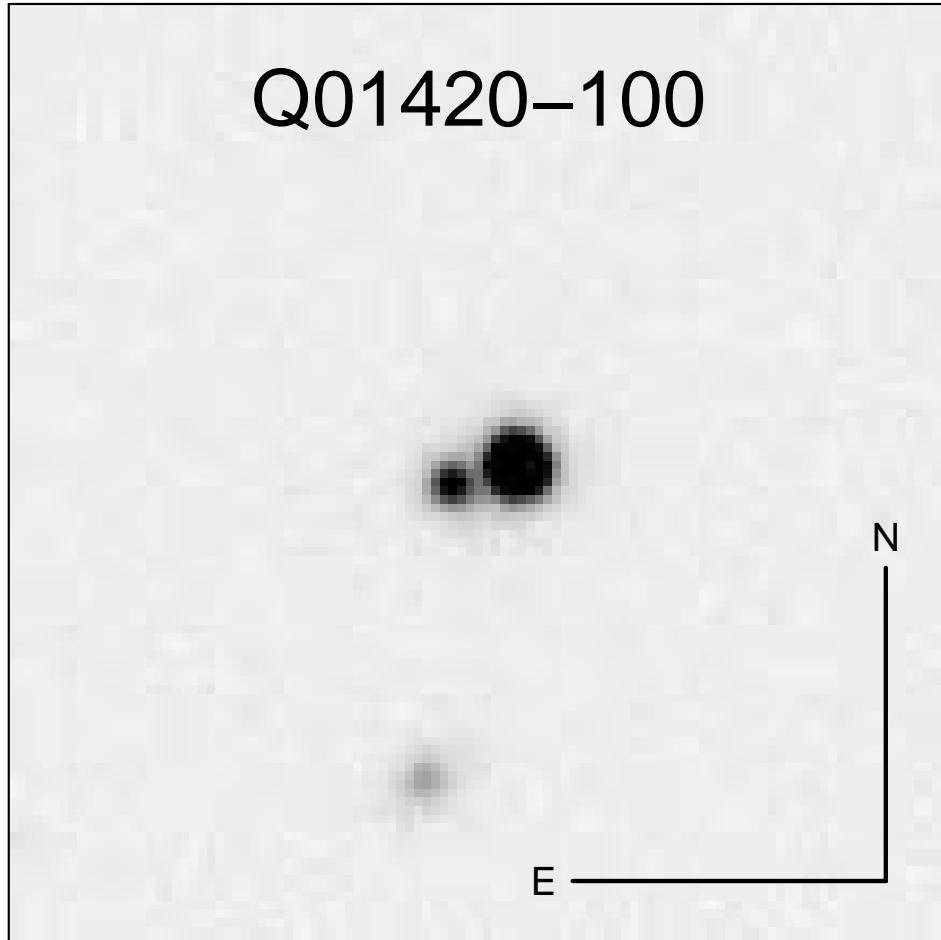


Fig. 2.7.— An image of the gravitationally lensed quasar system Q01420–100 taken with RETROCAM on 2 October 2004. The two images are separated by 2.4 arcsec. Orientation axes are 10 arcsec in length. Some diffuse light from the lens galaxy can be seen between the two images. This image was taken under 1.1 arcsec seeing conditions.

## CHAPTER 3

# MICROLENSING OF THE LENSED QUASAR SDSS 0924+0219

### 3.1. INTRODUCTION

In the standard Cold Dark Matter (CDM) galaxy model, early-type galaxies are composite objects. Their mass is dominated by an extended dark matter halo that surrounds the luminous stars of the visible galaxy; any remaining baryons are left as hot gas (White & Rees 1978). The halos grow by mergers with other halos, with a small fraction of the accreted smaller halos surviving as satellite halos (“sub-structure”) orbiting in the larger halos, but the mass fraction in these satellites is uncertain (Moore et al. 1999, Klypin et al. 1999, Gao et al. 2004, Taylor & Babul 2005 and Zentner et al. 2005 ). There is increasing evidence from time delay measurements (e.g. Kochanek et al. 2006) and stellar dynamical observations (e.g. locally, Romanowsky et al. 2003, and in lenses Treu & Koopmans 2002, Treu et al. 2006), that the density structure of some early-type galaxies on scales of  $1-2R_e$  is heterogeneous, but this needs to be changed from a qualitative assessment to

something more quantitative. Thus the detailed balance between stars, dark matter and substructure (luminous or dark) remains a matter of debate.

One approach to addressing these problems is to monitor variability in gravitational lenses. Variability in lenses arises from two sources. Correlated variability between the images due to fluctuations in the source flux allows the measurement of the time delays  $\Delta t$  between the quasar images, which constrain the combination  $\Delta t \propto (1 - \langle \kappa \rangle)/H_0$  of the surface density near the lensed images  $\langle \kappa \rangle = \langle \Sigma \rangle/\Sigma_c$  and the Hubble constant  $H_0$  to lowest order (Kochanek 2002).<sup>1</sup> By measuring the surface density near the lensed images, we can strongly constrain the radial mass profile of the lens. Uncorrelated variability between the images is a signature of microlensing by stars in the lens galaxy. Microlensing can constrain the mass distribution because the statistics of the variations depend on the fraction of the local density in stars (Schechter & Wambsganss 2002). In addition to providing an estimate of the surface density in stars near the lensed images, microlensing can also be used to estimate the mean stellar mass in the lens and to determine the structure of quasar accretion disks. Understanding microlensing is also required to improve estimates of the substructure mass fraction in radio-quiet lenses, because most other quasar source components are affected by both substructure and microlensing. In

---

<sup>1</sup>The dimensionless surface density  $\kappa$  is the surface density  $\Sigma$  divided by the critical surface density  $\Sigma_c \equiv c^2 D_{OS}/4\pi G D_{OL} D_{LS}$ , where  $D_{OL}$ ,  $D_{OS}$  and  $D_{LS}$  are the angular diameter distances between the Observer, Lens and Source.

order to use time variability in lenses to probe these astrophysical problems, we have undertaken a program to monitor roughly 25 lenses in several optical and near-IR bands. The first results of the program and a general description of our procedures are presented in Kochanek et al. (2006).

In this chapter we study the four-image  $z_s = 1.52$  quasar lens SDSS 0924+0219 (Inada et al. 2003) using  $V$ ,  $I$  and  $H$ -band Hubble Space Telescope (*HST*) observations and the results from two seasons of monitoring the system in the  $R$ -band. The lens galaxy is a fairly isolated  $z_l = 0.393$  (Ofek et al. 2005) early-type galaxy. The most remarkable feature of this lens is that it shows a spectacular flux ratio anomaly between the A and D images. These two images are merging at a fold caustic with a flux difference of nearly 3 magnitudes when they should have approximately equal fluxes by symmetry (Keeton et al. 2005). Keeton et al. (2006) recently measured the flux ratios in the  $\text{Ly}\alpha$  line and the adjacent continuum, finding that the anomaly is weaker in the emission line but still present. This indicates that the anomaly is partly due to microlensing, since the expected size difference between the broad line region and the optical continuum emission region should matter for microlensing but be irrelevant for substructure. Unfortunately, the continued existence of the anomaly in the emission line means either that the broad line region is not large enough to eliminate the effects of microlensing or that the flux ratio anomaly in SDSS0924+0219 is due the combined effects of microlensing and substructures.

We present the HST data in §3.2 as well as a series of mass models for the system consisting of the observed stellar distribution embedded in a standard dark matter halo. In §3.3 we present the light curves and model them using the Monte Carlo methods of Kochanek (2004). The analysis allows us to estimate the mean stellar mass in the lens galaxy, the size of the quasar accretion disk and the mass of the black hole powering the quasar. In §3.3.4 we present our predictions for the expected variability of this source over the next decade. Finally, we summarize our findings in §3.4. All calculations in this chapter assume a flat  $\Lambda$ CDM cosmology with  $h = 0.7$ ,  $\Omega_M = 0.3$  and  $\Omega_\Lambda = 0.7$ .

## 3.2. HST OBSERVATIONS AND MASS MODELS

In this section we discuss the HST observations and our mass model fits to the astrometric and photometric measurements.

### 3.2.1. HST OBSERVATIONS

We observed the lens in the  $V$ - (F555W),  $I$ - (F814W) and  $H$ -bands (F160W) using *HST*. The  $\sim 4380$  sec  $V$ -band and the  $\sim 4600$  sec  $I$ -band images were obtained as eight dithered sub-images with the Wide Field Channel (WFC) of the Advanced Camera for Surveys (ACS) on 2003 November 18. The 5120 sec  $H$ -band image was obtained as eight dithered sub-images on 2003 November 23 using the Near-Infrared

Camera and Multi-Object Spectrograph (NICMOS). The ACS data were reduced using the *pyraf multidrizzle* package, and the NICMOS data were reduced using *nicred* (see Lehár et al. 2000). We focus on the results from the new  $H$ -band image, shown in Fig. 3.1. The four quasar images, the central lens galaxy and an Einstein ring image of the quasar host galaxy can easily be seen.

We fit the  $H$ -band image using a photometric model consisting of four point sources and a de Vaucouleurs model for the lens galaxy. We modeled the lensed host galaxy as an exponential disk, using a singular isothermal ellipsoid (SIE) mass model for the lens galaxy. We also tried a de Vaucouleurs lens galaxy mass model, but doing so caused no significant change in the quality of the lensed host galaxy photometric fit (see Peng et al. 2006, for a discussion of systematic issues in modeling lensed host galaxies). The fits were done with *imfitfits* (see Lehár et al. 2000) using a range of bright PSF models, with the PSF producing the best overall fit being adopted for the final results. We then use the  $H$ -band fit as our reference, and we hold the astrometry and model structure fixed for the  $V$ - and  $I$ -band photometric fits. In Table 3.1, we present astrometric and photometric measurements for the system. Our fits to the lens astrometry and photometry are consistent with those of Keeton et al. (2006) and Eigenbrod et al. (2005).

The lens in SDSS 0924+0219 is an early-type galaxy with effective radius  $R_e = 0''.31 \pm 0''.02$ , axis ratio  $q = 0.92 \pm 0.02$ , major axis position angle  $\theta_e = -27 \pm 8^\circ$  (East of North) and colors  $V - I = 1.44 \pm 0.07$  and  $V - H = 3.60 \pm 0.05$ . Following

the technique of Rusin & Kochanek (2005), we performed a Fundamental Plane (FP) analysis of the lens to determine if its observed properties fall on the track of the expected Mass-to-Light (M/L) evolution with redshift for elliptical galaxies (Rusin et al. 2003). Assuming that a nominal early-type galaxy undergoes a starburst phase at high redshift and then evolves passively thereafter, we expect elliptical galaxies to show a steady increase in M/L with decreasing redshift. If the SDSS0924+0219 lens galaxy is to lie on the present-day FP, then it requires a  $\Delta \log(M/L)$  evolution of  $-0.42 \pm 0.03$  from  $z = 0.393$  to  $z = 0$ . This is steeper than the mean value for lens galaxies around that redshift,  $\Delta \log(M/L) = -0.22 \pm 0.04$ , implying that the lens has a smaller than average M/L. Note, however, that Treu et al. (2006) find a faster evolution than Rusin et al. (2003), which would be consistent with the value we find for SDSS0924+0219.

One remarkable feature in this lens is how the stars (or a small satellite) in the lens galaxy have provided a natural coronagraph at the location of image D. The quasar flux is suppressed by roughly an order of magnitude, making it very easy to see into the central regions of the host galaxy. We obtain a good fit with a host having a scale length of  $0''.11 \pm 0''.01$ , axis ratio of  $0.74 \pm 0.05$  and magnitude of  $H = 20.56 \pm 0.14$  mag. For comparison, we estimate an unmagnified magnitude of  $H = 20.40 \pm 0.20$  mag for the quasar. We also attempted a de Vaucouleurs model fit to the host galaxy, but we found that doing this resulted in a negligible change in the overall quality of fit. We are not able to discriminate between host galaxy

models. We extracted the Einstein ring curve of the lens (Kochanek et al. 2001) to use as one of the constraints on the mass models.

Images A, B and C have similar  $I - H$  and  $V - I$  colors, while image D is significantly redder in  $I - H$  but of similar color in  $V - I$ . This is similar to the expected pattern for dust extinction, since an 0.5 mag difference in  $I - H$  should correspond to a 0.15 mag difference in  $V - I$  for an  $R_V = 3.1$  extinction curve shifted to the redshift of the lens. On the other hand, the Einstein ring image of the host galaxy does not show color trends near the D image, which strongly argues against dust as the origin of the color differences. Moreover the significant differences between the A/D flux ratio in  $\text{Ly}\alpha$  as compared to the continuum (Keeton et al. 2006), means that microlensing must be a significant contributor to the anomalous flux ratio.

### 3.2.2. MACRO MODELS AND SUBSTRUCTURE

We modeled the lens galaxy as the sum of a de Vaucouleurs model with scale length  $R_e = 0''.31$  embedded in an NFW (Navarro, Frenk & White 1996) model with a break radius  $r_c = 10''.0$ . The de Vaucouleurs and NFW models were ellipsoids constrained by the axis ratio and orientation of the lens galaxy in the  $H$ -band images, and we included an external shear to model any additional perturbations from the lens environment or along the line of sight. We constrained the mass model

with the astrometry of the quasar images and the Einstein ring curve derived from the  $H$ -band images (Kochanek et al. 2001) using the GRAVLENS (Keeton 2001) software package. We required the NFW and de Vaucouleurs components to be perfectly concentric, but we permitted the combined model to move within  $0''.01$  of the measured galaxy center in order to optimize the fit. As described in detail by Kochanek (2005), it is not possible to determine the radial mass profile of the lens using these constraints, although it can be done using other constraints such as a time delay or stellar velocity dispersion measurement. Given this degeneracy, we generated a sequence of models parameterized by  $0 \leq f_{M/L} \leq 1$ , the fractional mass of the de Vaucouleurs component compared to a constant M/L model ( $f_{M/L} = 1$ ). As expected, there is no significant difference in how well models with  $0 < f_{M/L} \leq 1$  fit the constraints with the exception of pure dark matter models ( $f_{M/L} \lesssim 0.1$ ) that predict a detectable, fifth or odd quasar image near the center of the Einstein ring. The convergence, shear and  $\kappa_*/\kappa$  for the range of  $f_{M/L}$  at each image location is presented in Table 3.2.

Although much of the anomalous A/D flux ratio must be due to microlensing based on the smaller anomaly observed in the emission lines, we explored the extent to which the anomaly could be created by small satellites of the lens galaxy rather than by stars. For these tests we modeled the main lens as a singular isothermal ellipsoid (SIE) and then added a low-mass pseudo-Jaffe model as a perturber. We assigned the perturber Einstein radii of either  $0''.01$  or  $0''.003$  and tidal truncation

radii of  $0''.1$  and  $0''.06$ , respectively. Figures 3.2 and 3.3 show the goodness of fit,  $\chi^2/N_{DOF}$ , as a function of the perturber's position, where we fit both the astrometric constraints from the quasar image positions and the flux ratios from the  $H$ -band *HST* data. While the more massive satellite with an Einstein radius of  $0''.01$  has difficulty adjusting the flux ratio without violating the astrometric constraints, the lower mass satellite can do so if properly positioned. Such a satellite would have a mass of  $\sim 10^{-5}$  that of the primary lens, roughly corresponding to the mass scale of globular clusters. While the emission line flux ratios largely rule this out as a complete explanation for SDSS 0924+0219, substructure could explain the continued existence of an anomaly in the emission line flux ratios. We include this calculation as an illustration that substructure can lead to anomalies as extreme as are observed here.

### 3.3. MICROLENSING

#### 3.3.1. MONITORING DATA AND MICROLENSING

We have obtained somewhat more than two seasons of  $R$ -band monitoring data for SDSS 0924+0219. Our analysis procedures are described in detail in Kochanek et al. (2006), so we provide only a brief summary here. We measure the flux of each quasar image relative to a sample of reference stars in each frame. We keep the relative positions of the components fixed, using the *HST* astrometry for the

lensed components, and derive the PSF model and quasar flux for each epoch by simultaneously fitting the lens and the reference stars. The PSF is modeled by 3 nested, elliptical Gaussian components. The galaxy is included in the model at a constant flux which we determine by fitting all the data as a function of the galaxy flux and then adopting the galaxy flux that produces the best fit to the complete data set. We confirm that the lens galaxy flux is approximately constant at each epoch by examination of the residual galaxy flux after subtraction of the best-fit models, and we find no evidence for variability during our three seasons of monitoring.

Most of our observations were obtained at the queue-scheduled SMARTS 1.3m using the ANDICAM optical/infrared camera (DePoy et al. 2003).<sup>2</sup> Additional observations were obtained at the Wisconsin-Yale-Indiana (WIYN) observatory using the WIYN Tip-Tilt Module (WTTM) <sup>3</sup>, the 2.4m telescope at the MDM Observatory using the MDM Eight-K <sup>4</sup>, Echelle and RETROCAM <sup>5</sup> (Morgan et al. 2005) imagers, the 3.5m APO telescope using Spicam and the 6.5m Magellan Baade telescope using IMACS (Bigelow et al. 1999). Images taken under seeing conditions worse than 1".5 were discarded. We also added the photometry from Inada et al. (2003) to extend our baseline to nearly four years for the microlensing calculations.

---

<sup>2</sup><http://www.astronomy.ohio-state.edu/ANDICAM/>

<sup>3</sup>[http://www.wiyn.org/wttm/WTTM\\_manual.html](http://www.wiyn.org/wttm/WTTM_manual.html)

<sup>4</sup><http://www.astro.columbia.edu/~arlin/MDM8K/>

<sup>5</sup><http://www.astronomy.ohio-state.edu/MDM/RETROCAM>

The  $R$ -band light curves are displayed in Fig. 3.4, and the data are presented in Table 3.3.

In Fig. 3.4, we also show the *HST*  $V$ -band photometry scaled to the best-fit  $R$ -band monitoring magnitude of Image A on the observation date. In the *HST* data, image D is  $\sim 1$  mag fainter relative to image A than our estimate on nearly the same date. After considerable experimentation, we concluded that our flux for image D may be contaminated by image A, although we found no correlation between the A/D flux ratio and the seeing. Nonetheless, we include estimates of seeing at each observation epoch in Table 3.3. In the calculations that follow we will use both our image D light curve as observed and an image D light curve shifted 1 mag fainter to agree with the *HST* flux ratio. The shift had little effect on our results in § 3.3.2–3.3.4.

In our mass models, the longest expected delay for the system is  $\sim 10$  days for  $H_0 = 72 \text{ km s}^{-1} \text{ Mpc}^{-1}$ . We see little evidence for correlated variability between the images on these time scales, so we cannot measure the time delays. For the present study, it seems safe to simply ignore the time delays.

### 3.3.2. MICROLENSING MODELS

For each of our macro models, parameterized by  $f_{M/L}$ , we generated 8 random realizations of the expected microlensing magnification patterns for each image. We

used patterns with an outer dimension of  $20R_e$  where  $R_e = 5.7 \times 10^{16} \langle M/M_\odot \rangle^{1/2}$  cm is the Einstein radius for the average mass star. The map dimensions were  $8192^2$ , so we can model source sizes down to  $3 \times 10^{-3}R_e$ . The stars used to create the patterns were drawn from a Salpeter IMF with a dynamic range in mass of a factor of one hundred. We modeled the accretion disk of the quasar as a standard, face-on thin disk model (Shakura & Sunyaev 1973) with a scale length of  $r_s = \hat{r}_s \langle M/M_\odot \rangle^{1/2}$  where the microlensing behavior is determined by the source size scaled by the mean mass of the microlenses,  $\hat{r}_s$ . We have chosen to use a thin disk model because it provides a context for interpreting the results, but Mortonson et al. (2005) have shown that  $r_s$  can simply be interpreted as the typical half-light radius for any choice of emission profile. We do, however, neglect the central hole in the disk emissivity to avoid the introduction of an additional parameter. We fit the light curves using the Monte Carlo method of Kochanek (2004). In this method, large numbers of trial light curves are randomly generated and fitted to the observed light curves. Bayesian statistical methods are used to combine the resulting distributions of  $\chi^2$  values for the fits to the light curves to obtain probability distributions for the model parameters.

We are interested in models where microlensing is responsible for any deviations of the image flux ratios from the lens model, so we assumed that the flux ratios of the macro model were correct up to a systematic uncertainty of 0.05 mag for images A–C and 0.1 mag for image D. We also allowed for an 0.02 mag systematic

uncertainty in the photometry of images A–C and an 0.1 mag systematic uncertainty in the photometry of image D. These errors were added because the point-to-point scatter in the light curves is somewhat broader than the formal uncertainties in the photometry. With these assumptions, we have no difficulty finding light curves that fit the data well, with  $\chi^2/N_{DOF} \approx 1.0$ . We generated  $10^5$  trial light curves for each source size, magnification pattern and mass model. Several example light curves which provide good fits to the data are shown in Fig. 3.5. For each reasonable fit to the light curves, defined by  $\chi^2/N_{DOF} \leq 2.3$ , we also generated an extrapolated light curve extending for an additional ten years beyond the last data point of the third season (2005 December 14; HJD 2453719). We also repeated all the calculations shifting the image D light curve 1 mag fainter to match the HST observations, finding few changes in the results.

In order to convert the results from Einstein radius units, where all physical scales depend on the mean mass of the microlenses  $\langle M/M_\odot \rangle$ , we must assume either a probability distribution for the actual velocities or a prior for the mean stellar mass. Our velocity model includes the  $176 \text{ km s}^{-1}$  projected velocity of the CMB dipole onto the plane of the lens, a probability distribution for the one-dimensional peculiar velocity dispersion of galaxies at  $z_l$  with rms value of  $164 \text{ km s}^{-1}$  and a one-dimensional stellar velocity dispersion in the lens galaxy of  $219 \text{ km s}^{-1}$  based on the Einstein radius of the lens and an isothermal lens model. As discussed in detail by Kochanek (2004), the lens galaxy peculiar velocity dispersion and stellar

velocity dispersion estimates are dependent upon the selected cosmology. We have chosen the standard flat concordance cosmology ( $\Omega_M = 0.3$  and  $\Omega_\Lambda = 0.7$ ) for our estimates. We also consider the consequences of using a limited range for the mean stellar mass of  $0.1 \leq \langle M/M_\odot \rangle < 1.0$ .

Figures 3.6 and 3.7 show the results for the system motions and the lens galaxy stellar mass estimate. The large flux ratio anomalies combined with the limited amount of observed variability means that the effective velocity in the system must be relatively low. We find that  $280 \text{ km s}^{-1} \lesssim \hat{v}_e \lesssim 749 \text{ km s}^{-1}$  (68% confidence), and this changes little if we adjust the D image light curve to be 1 mag fainter. If we compare the effective velocity distribution to our model for the possible distribution of physical velocities (Fig. 3.6), we can estimate the mean microlens mass since the two velocities are related by  $\hat{v}_e = v_e/\langle M/M_\odot \rangle^{1/2}$ . The broad range permitted for  $\hat{v}_e$  translates into a broad range for the stellar mass estimates, with  $0.02 M_\odot \lesssim \langle M \rangle \lesssim 1.0 M_\odot$  (68% confidence). The low mass solutions correspond to large sources with high effective velocities and the high mass solutions correspond to small sources with low effective velocities.

We were somewhat surprised to find that the present data do not distinguish between the lens models at all because we had based our expectations on the (Schechter & Wambsganss 2002) picture in which models with low  $\kappa_*/\kappa$  dominate the probability of finding a faint saddle point image like D. We found instead that the probability distribution for  $f_{M/L}$  is basically flat. This result is little affected by

imposing the prior on the permitted mass range of the microlenses or by adjusting the image D light curve to be 1 mag fainter. In comparison, the microlensing models for SDSS 0924+0219 by Keeton et al. (2006) strongly favored models with low  $\kappa_*/\kappa$ . We believe the differences between the results are due to our use of finite-sized sources, which significantly enhance the probability of large demagnifications relative to large magnifications because the high magnification regions (caustics) are more affected by finite source sizes. Another source of differences is that we are analyzing a more strongly constrained problem by requiring that the models fit the observed light curves rather than simply fit the instantaneous flux ratios.

### 3.3.3. QUASAR STRUCTURE

One objective of our monitoring program is to study the structure of quasar accretion disks. We start by estimating the black hole mass using the  $M_{BH}$ , Mg II line width, luminosity relations of McLure & Jarvis (2002) and Kollmeier et al. (2006). We measured the Mg II(2800Å) line width in spectra obtained by Ofek et al. (2005) following the procedures detailed in Kollmeier et al. (2006), and we estimated the magnification-corrected continuum luminosity at 3000Å,  $L_\lambda(3000\text{Å})$ , using a power law fit to our HST data. For the McLure & Jarvis (2002) calibration we find a black hole mass of  $M_{BH} = (6.3 \pm 1.5) \times 10^7 M_\odot$ , and for the (Kollmeier et al. 2006) calibration we find  $M_{BH} = (7.3 \pm 2.4) \times 10^7 M_\odot$ . We adopt the estimate based on the Kollmeier et al. (2006) calibration. Similarly, we

estimate that the magnification-corrected bolometric luminosity of the quasar is  $L_{bol} = (2.7 \pm 1.3) \times 10^{45} \text{ erg s}^{-1}$  where we follow Kaspi et al. (2000) in assuming that  $L_{bol} \simeq 9 \times \lambda L_{\lambda}(5100\text{\AA})$ . This bolometric luminosity corresponds to an accretion rate  $\dot{M} = (0.48 \pm 0.24)\eta_{0.1}^{-1}M_{\odot} \text{ yr}^{-1}$ , where  $\eta = 0.1\eta_{0.1}$  is the radiative efficiency of the accretion. Fig. 3.8 summarizes these “classical” constraints on the quasar.

The new constraint we obtain from the microlensing observations is on the size  $r_s$  of the quasar, which we can also estimate using our accretion disk model and the observed flux. A standard thin disk model (Shakura & Sunyaev 1973) radiates as a black body with a temperature profile of  $T = T_s(R/r_s)^{-3/4}$ , and the scale length we measure should correspond to the point in the disk where the temperature corresponds to the rest-frame wavelength of the filter band pass. For our  $R$ -band data (2770\AA in the quasar rest frame), our scale length corresponds to the point where  $T_s(r_s) \simeq 5.2 \times 10^4 \text{ K}$ . If the viscous energy release is radiated locally and we are well removed from the Schwarzschild radius, then the disk temperature and scale length are related to the black hole mass  $M_{BH}$  and accretion rate  $\dot{M}$  by

$$\sigma T_s^4 = 3GM_{BH}\dot{M}/8\pi r_s^3 \tag{3.1}$$

(Shakura & Sunyaev 1973), so a measurement of  $r_s$  constrains the product  $M_{BH}\dot{M}$ . One means of estimating  $r_s$  is to simply compute what it must be to produce the

observed  $R$ -band flux. Again assuming a standard, face-on thin disk, the emission profile is

$$I(R) \propto \left[ \exp \left( (R/r_s)^{3/4} \right) - 1 \right]^{-1} \quad (3.2)$$

(Shakura & Sunyaev 1973). Assuming that the disk radiates locally as a blackbody, we integrate this emission profile over the physical extent of the disk to estimate its specific luminosity  $L_{\nu,em}$  in the rest frame. Incorporating the system's geometry and correcting for redshift effects, we convert  $L_{\nu,em}$  to  $F_{\lambda,obs}$ , the specific flux in the observed frame. We then solve  $F_{\lambda,obs}$  for  $r_s$  to yield

$$r_{s\lambda,obs} = 2.83 \times 10^{15} \frac{1}{\sqrt{\cos i}} \left( \frac{D_{OS}}{r_H} \right) \left( \frac{\lambda_{obs}}{\mu\text{m}} \right)^{3/2} 10^{-0.2(M_{\lambda_{obs}} - 19)} h^{-1} \text{ cm}, \quad (3.3)$$

where  $M_{\lambda,obs}$  is the observed magnitude,  $D_{OS}/r_H$  is the angular diameter distance to the quasar in units of the Hubble radius and  $i$  is the disk inclination angle, assumed to have an average value  $\langle i \rangle = 60^\circ$ . For SDSS 0924+0219, we find an unmagnified *HST*  $I$ -band magnitude  $I = 21.24 \pm 0.25$  mag, yielding the scale radius at the redshifted center of the *HST*  $I$ -band,  $r_{sI,obs} = 6.3 \pm 1.6 \times 10^{14}$  cm. Assuming the  $T^{-4/3}$  scaling of thin disk theory, we estimate an  $R$ -band disk size of  $r_{sR,obs} = 5.0 \pm 1.3 \times 10^{14}$  cm. We show the resulting constraint on  $M_{BH}\dot{M}$  in Fig. 3.8.

Micro lensing tests this theoretical calculation because the amplitude of the microlensing variability is controlled by the projected area of the source that smooths the magnification patterns. Fig. 3.9 shows our estimate of the scaled  $R$ -band source

size  $\hat{r}_s$ , which is related to the physical source size by  $r_s = \hat{r}_s \langle M/M_\odot \rangle^{1/2}$ . The source must be quite compact relative to the Einstein radius of the typical microlens, with an exact bound that is presently difficult to determine because of the limited level of observed variability. We face two technical problems in extending Fig. 3.9 to smaller source sizes. The first problem is that our analysis code is presently limited to  $8192^2$  magnification patterns, so when using an outer dimension large enough to produce a reasonable statistical representation of the magnification patterns it is difficult to resolve such small scales. The second problem is that even if we could resolve the smallest scales, we would find that the probability distribution flattens and becomes constant at small scale lengths. This occurs because the differences between small smoothing lengths are detectable only during caustic crossings – if our light curves do not extend to within a source size of a caustic, there is little effect from using a still smaller source size. Complete convergence at small scales will require a light curve with caustic crossings.

Despite these problems, we can estimate the physical source size of the accretion disk reasonably well because there is a fairly strong degeneracy between the scaled source size  $\hat{r}_s$ , the scaled velocity  $\hat{v}_e$  and the microlens mass scale  $\langle M/M_\odot \rangle$  in the sense that more compact sources require smaller scaled velocities which implies a larger microlens mass scale for the conversion to the physical source size (see Kochanek 2004). Fig. 3.10 shows the estimates of the physical size  $r_s$  both with and without the prior on the microlens masses. Reassuringly, the results depend

only weakly on the prior. Nonetheless, will adopt the results with the mass prior:  $3.0 \times 10^{14} \text{ cm} \lesssim r_s \lesssim 1.4 \times 10^{15} \text{ cm}$  at 68% confidence. This is consistent with our earlier estimate from the continuum flux but is a weaker constraint on  $M_{BH}\dot{M}$ , as shown in Fig. 3.8.

### 3.3.4. EXPECTATIONS FOR THE FUTURE BEHAVIOR OF SDSS0924+0219

For each light curve which passed a threshold of  $\chi^2/N_{DOF} \leq 2.3$ , we generated a light curve for a period of ten years beyond our most recent observation. For each image, we then tracked the maximum change in the brightness in both the positive and negative directions on 1, 3 and 10 year time scales. The normalized, cumulative distributions of these maximum changes are shown in Fig. 3.11. One of the more obvious predictions of Fig. 3.11 is that images A and B are likely to remain constant while images C and D are likely to become brighter. One of the original motivations of this study was to estimate the time scale on which the flux ratio anomaly would vanish as D moved out of a low-magnification region and became brighter. Here we find an approximately 12% chance that it will brighten by at least a factor of 2 in the course of the next year and a roughly 45% chance that it will brighten by more than an order of magnitude over the next decade. For the separate calculation in which we lowered the flux of all points on the image D light curve by +1 magnitude,

we predict a 9% probability of image D brightening by a factor of two during the next year, and a 53% chance that image D will brighten by a factor of ten during the next ten years.

Our expectation that D brightening would be the means of solving the anomaly was based on the preconception that D was a de-magnified saddle point in a model with a small ratio between the stellar and total surface densities  $\kappa_*/\kappa$ . Schechter & Wambsganss (2002) demonstrated that in this regime there is an appreciable probability of strongly de-magnifying saddle point images like D. Our results confirm this finding.

### 3.4. CONCLUSIONS

During the course of our monitoring campaign we have observed uncorrelated variability in the four images of SDSS 0924+0219, evidence that microlensing is occurring in this system. Furthermore, our models demonstrate that microlensing is a viable explanation for the system's anomalous flux ratios. This study does not rule out the alternative hypothesis that dark matter substructure contributes to the anomaly, but it does firmly establish the presence of microlensing variability and the ability of microlensing to explain the anomaly. As we continue to monitor SDSS 0924+0219, we expect to eventually measure the time delay, thereby restricting the range of permissible halo models, and to steadily reduce the uncertainties in the

estimated mean stellar mass, accretion disk structure and black hole mass. At some point over the next few years, we should also see dramatic changes in the fluxes of the merging images.

We can also begin to compare microlensing estimates of the structure of quasar accretion disks. In our original study (Kochanek 2004), we modeled the significantly more luminous, but very similar redshift, quasar Q2237+0305 ( $M_V = -25.8 \pm 0.5$  versus  $M_V = -21.7 \pm 0.7$  after correcting for magnification). As we would expect from accretion disk theory, the microlensing analyses indicate that the more luminous quasar has a significantly larger scale ( $r_s \simeq 4.1 \times 10^{15}$  cm versus  $r_s \simeq 6.9 \times 10^{14}$  cm) and black hole mass ( $M_{BH} \simeq 1.1 \times 10^9 M_\odot$  versus  $1.3 \times 10^8 M_\odot$ ). The next step is to combine the microlensing analyses of many lenses to explore these correlations in detail and to use the wavelength dependence of the microlensing variability to study the structure of individual disks. This next step should be possible very shortly.

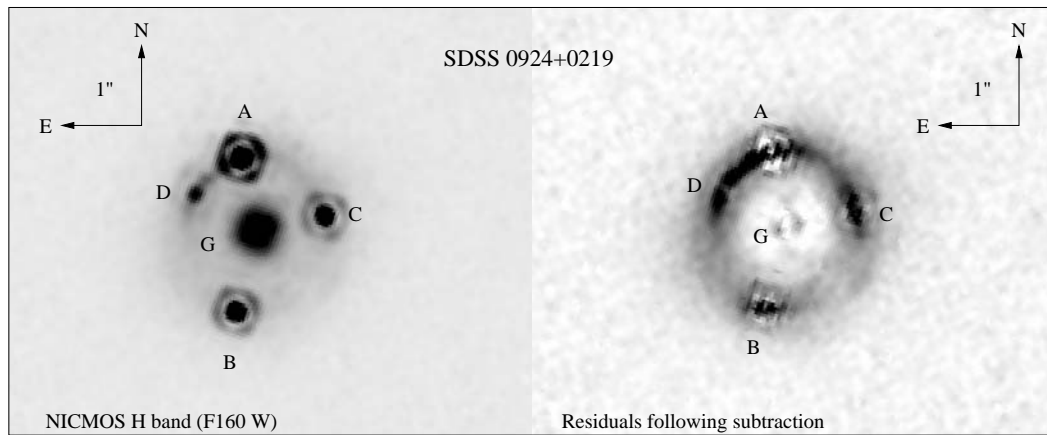


Fig. 3.1.—  $H$ -band images of SDSS0924+0219. The left panel shows the original image. Note that image D shows the Airy ring of a point source and is markedly fainter than image A. The right panel shows  $H$ -band residual near each quasar image after subtracting the four quasar images and the lens galaxy to make the Einstein ring image of the quasar host galaxy more visible. The noisy residuals near each image are largely due to small errors in the PSF models.

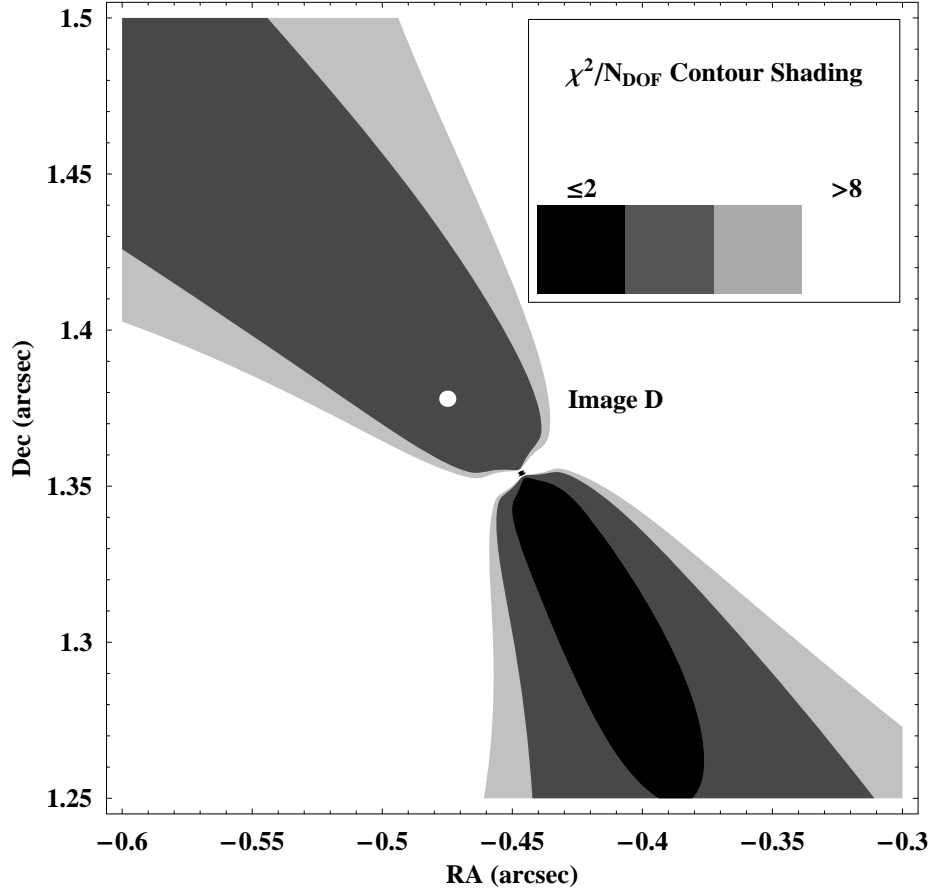


Fig. 3.2.— Substructure model for the SDSS0924+0219 flux ratio anomaly. Shown are the regions where a pseudo-Jaffe model with an Einstein radius of  $0''.01$  can remove the A/D flux ratio anomaly without significantly worsening the constraints on the quasar image positions or the Einstein ring. The main lens is modeled as a singular isothermal ellipsoid (SIE) and the pseudo-Jaffe models are tidally truncated at  $0''.1$ . The position of image D is indicated with a white point.  $\chi^2$  contours are indicated in the figure legends.

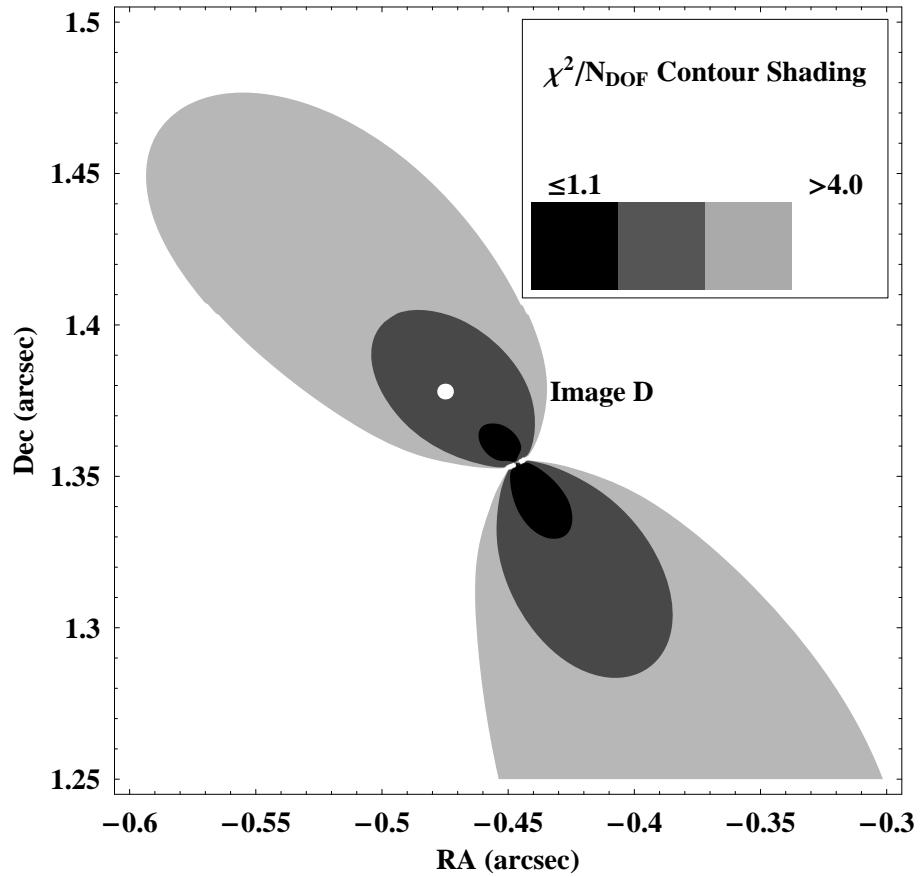


Fig. 3.3.— Same as Fig. 3.2, except the pseudo-Jaffe structure has an Einstein radius of  $0''.003$  and is tidally truncated at  $0''.06$ .

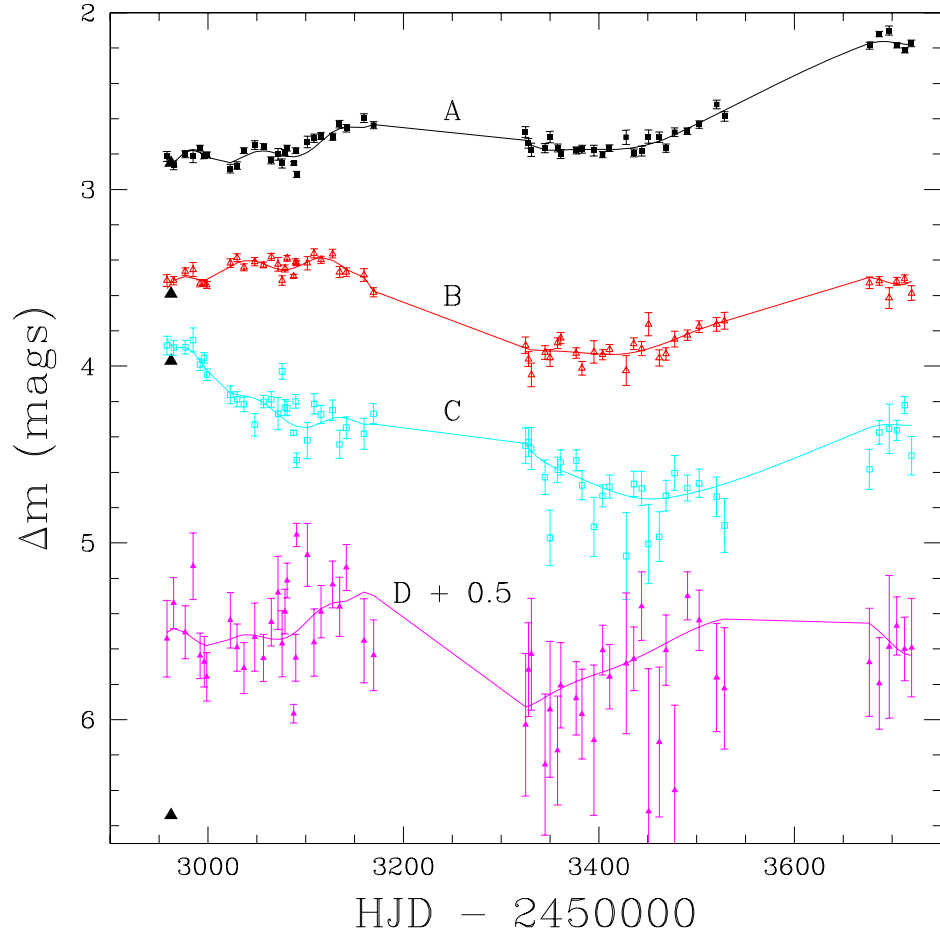


Fig. 3.4.— SDSS0924+0219 *R*-band light curves for images A–D. The data points for image D are offset to improve their visibility. The curves are derived from a joint, high-order polynomial fit for the source light curve combined with lower order polynomials for the microlensing variability of each image (see Kochanek 2005 for details). Symbols: Image A—solid squares, Image B—open triangles, Image C—open squares and Image D—solid triangles. The large solid triangles at 2962 days are the HST *V*-band photometry referenced to Image A.

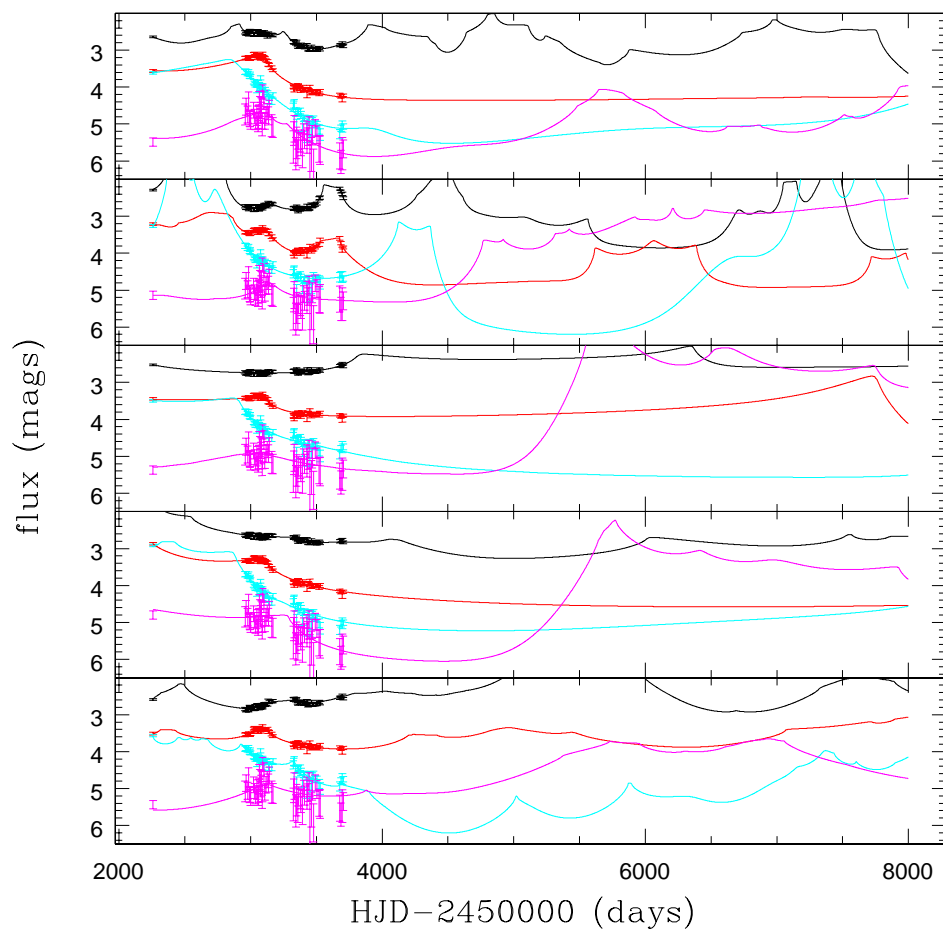


Fig. 3.5.— The five best fitting *R*-band light curves extrapolated for an additional 10 years across their magnification patterns. In order to show the “goodness of fit” of the theoretical microlensing lightcurves, we plot as points the observed image flux minus our model for the intrinsic variability of the source. In most of these light curves we see a brightening of images D and C.

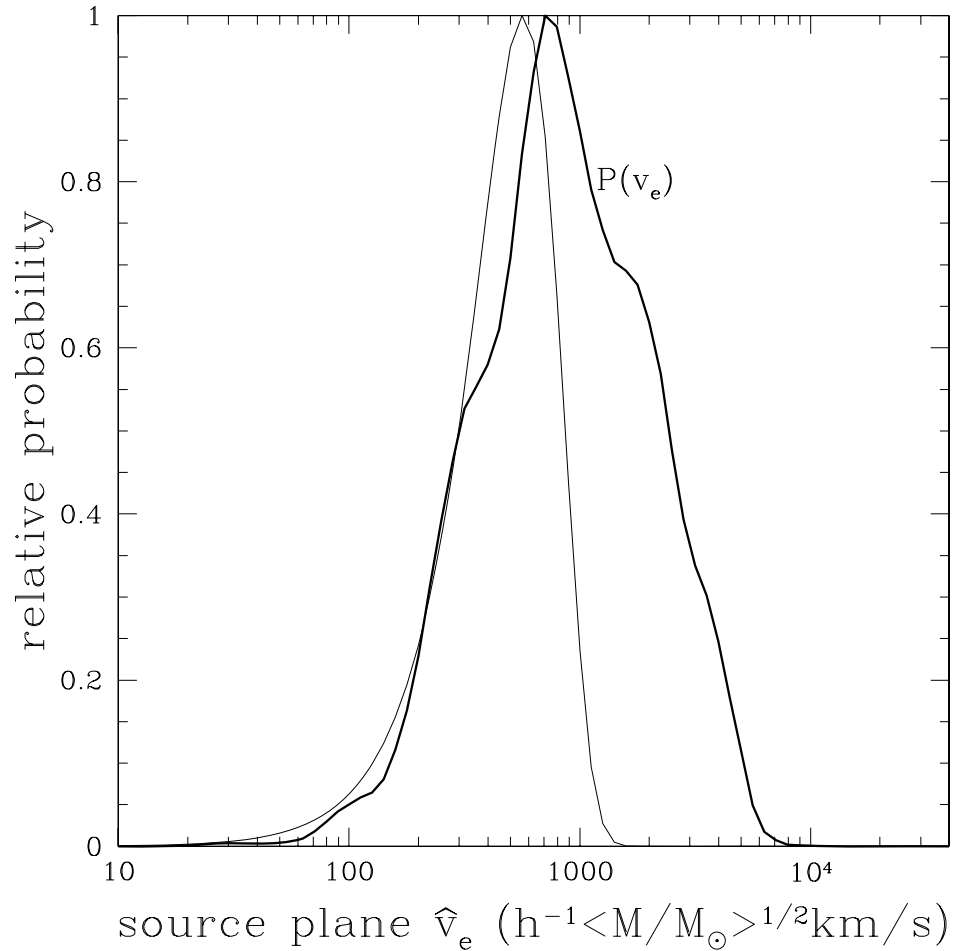


Fig. 3.6.— Normalized probability distribution for the effective source plane velocity ( $\hat{v}_e$ , heavy solid line) as compared to our estimated probability distribution for the true source plane effective velocity  $v_e$  (light solid line). Since the average microlens mass  $\langle M \rangle$  is related to the two velocities by  $\hat{v}_e \propto v_e / \langle M \rangle^{1/2}$ , high (low) ratios of  $\hat{v}_e / v_e$  correspond to low (high) mass microlenses.

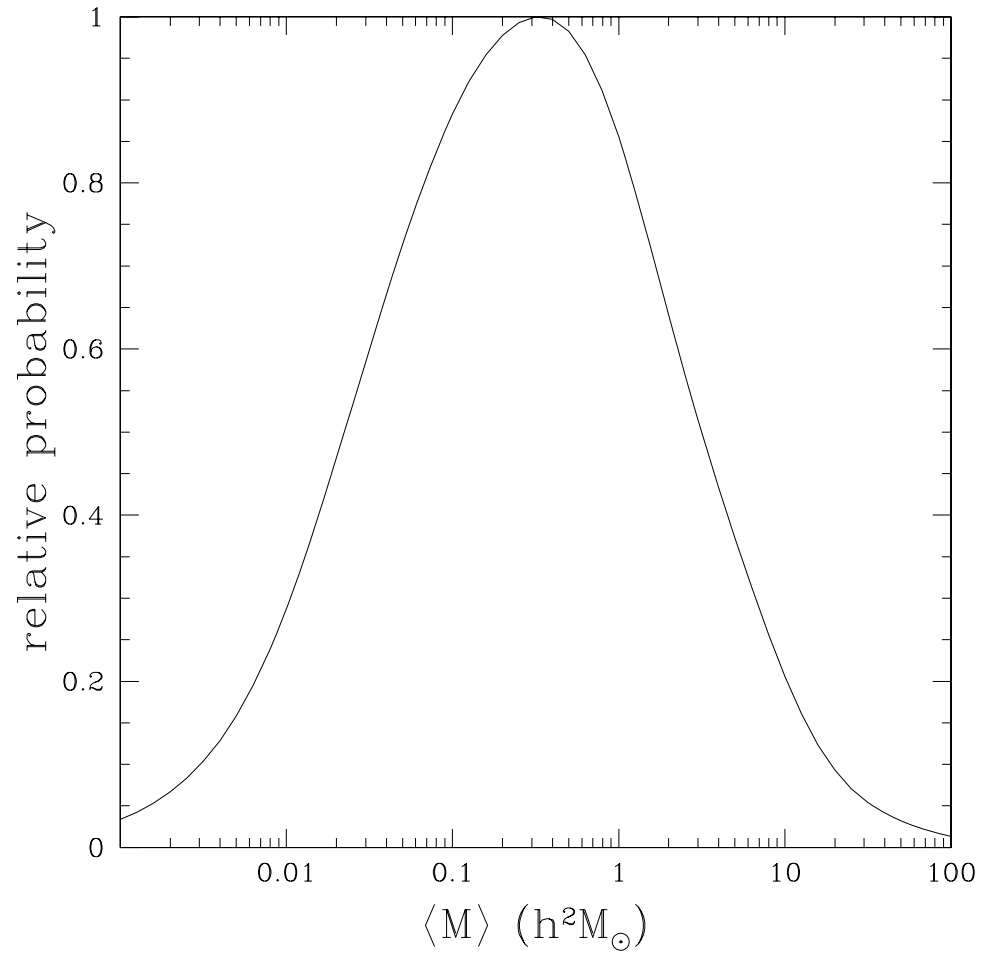


Fig. 3.7.— Probability distribution for the average stellar mass  $\langle M \rangle$  in the lens galaxy. The uncertainty is relatively large because  $\langle M \rangle \propto v_e^{-2}$ , but it is consistent with normal stellar populations.

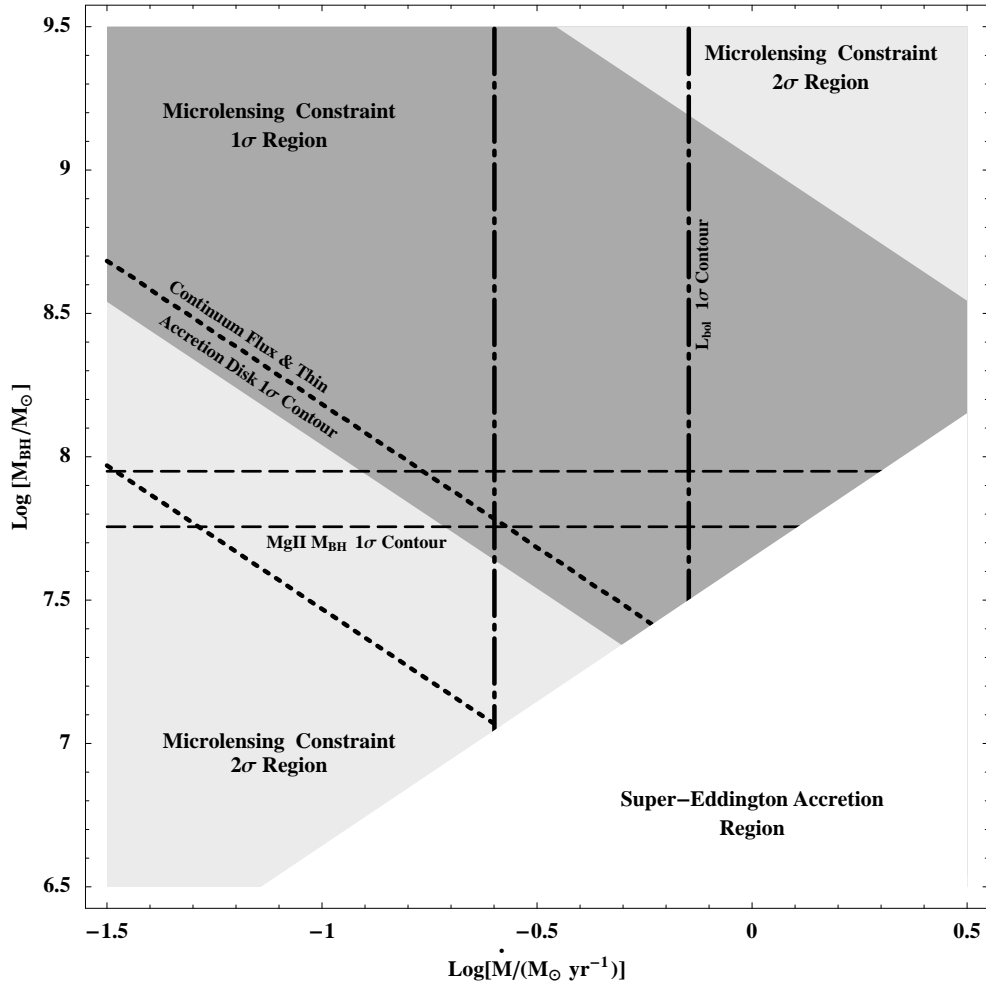


Fig. 3.8.— Constraints on the mass and accretion rate of the SDSS0924+0219 quasar. The dashed horizontal lines show the estimated black hole mass based on the Mg II 2800Å emission line width. The vertical dash-dotted lines show the estimated accretion rate assuming a radiative efficiency of 10% and the Kaspi et al. (2000) method for estimating the bolometric luminosity. The dotted lines show the constraint on the product  $M_{BH}\dot{M}$  from the continuum flux and thin accretion disk theory. The shaded regions show the constraint on the product  $M_{BH}\dot{M}$  from the microlensing data with a prior of  $0.1 M_{\odot} < \langle M \rangle < 1.0 M_{\odot}$  on the mean mass of the microlenses. The accretion is super-Eddington in the lower right corner, so we terminated the constraints on the line where  $L = L_{Edd}$ . All values plotted are scaled to  $h = 0.7$ .

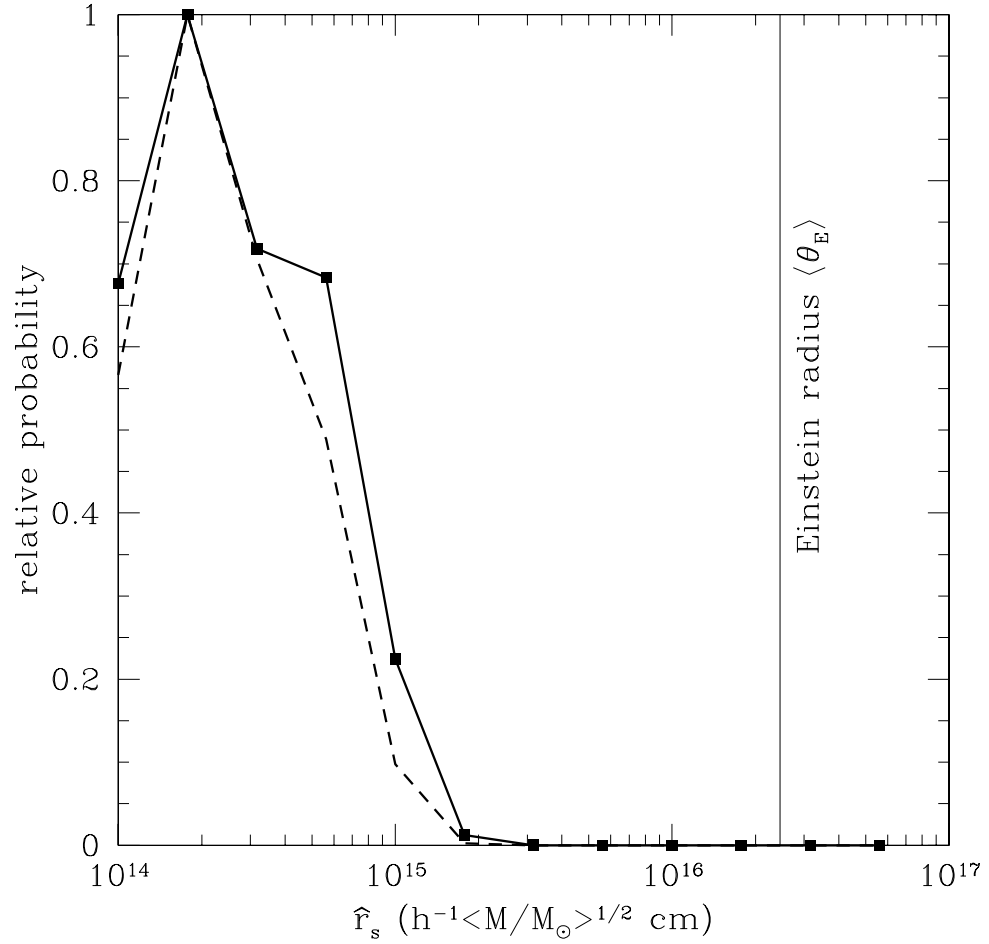


Fig. 3.9.— Probability distributions for the scaled source size  $\hat{r}_s$ . The heavy dashed line shows the estimate for  $\hat{r}_s$  including a prior of  $0.1 M_\odot < \langle M \rangle < 1.0 M_\odot$  on the mass of the stars. The vertical line shows the Einstein Radius  $\langle \theta_E \rangle$  of the average mass star.

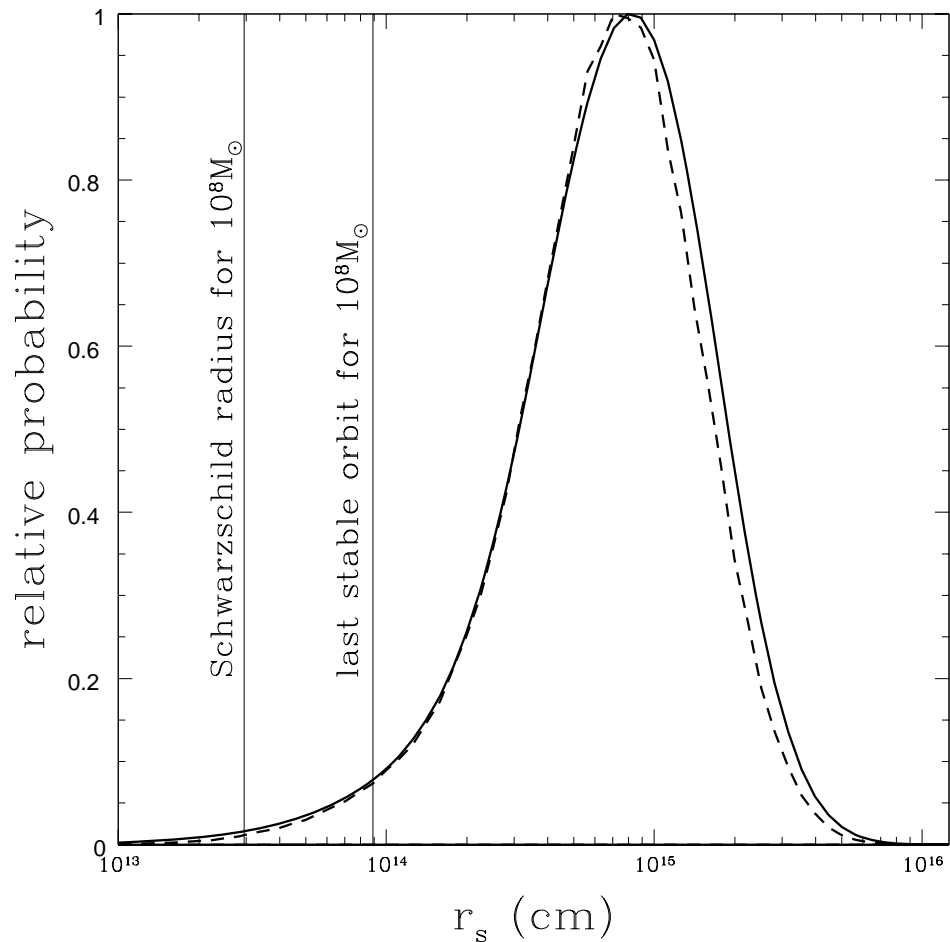


Fig. 3.10.— Probability distributions for the physical source size  $r_s$ . The dashed curve shows the estimate for  $r_s$  with a prior of  $0.1 M_\odot < \langle M \rangle < 1.0 M_\odot$  on the mean mass of the microlenses. The vertical line shows the Schwarzschild radius  $R_{BH} = 2GM_{BH}/c^2$  of a  $10^8 M_\odot$  black hole. The last stable orbit for a Schwarzschild black hole is at  $3R_{BH}$ .

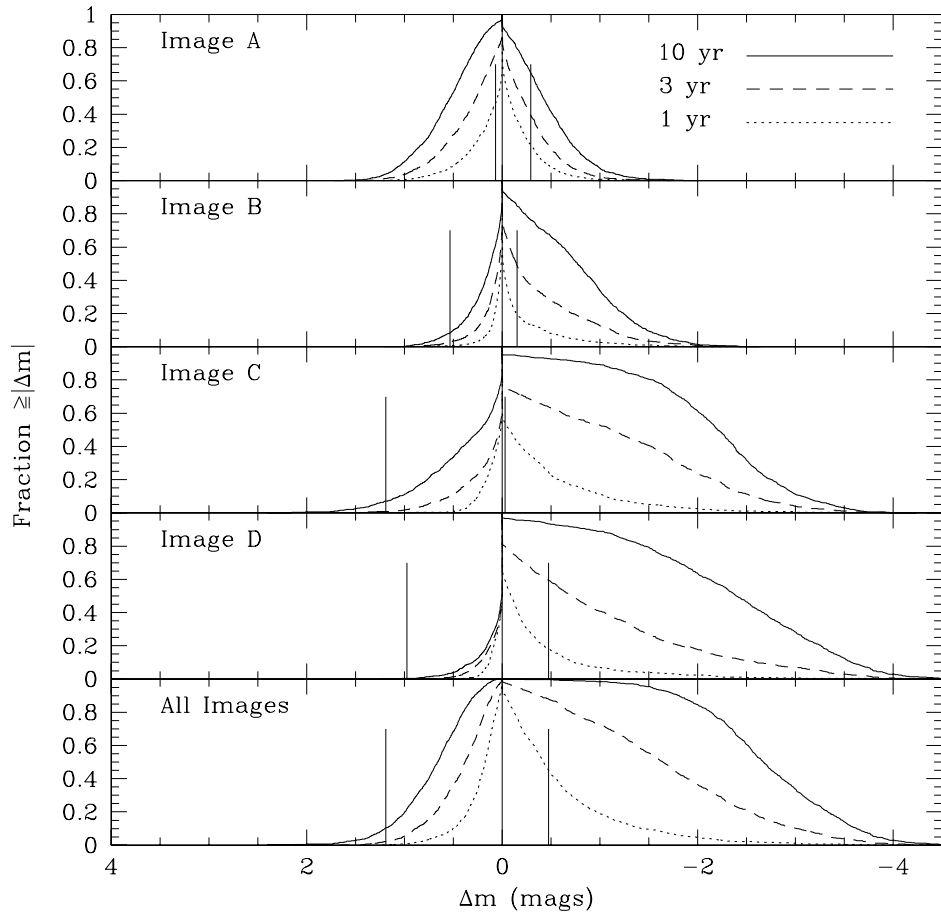


Fig. 3.11.— Fraction of light curves with  $\chi^2/N_{DOF} < 2.3$  that undergo a change in magnification larger than  $\Delta m$  magnitudes towards either brighter (right) or fainter (left) fluxes after one (dotted), three (dashed) or ten (solid) years. The vertical lines show the largest observed  $\Delta m$  for our present light curves.

Component	Astrometry		$\Delta\text{Dec}$	H=F160W	Photometry	
	$\Delta\text{RA}$				I=F814W	V=F555W
A	$\equiv 0$	$\equiv 0$	$\equiv 0$	$17.96 \pm 0.02$	$18.77 \pm 0.05$	$19.61 \pm 0.01$
B	$+0''.061 \pm 0''.003$	$-1''.805 \pm 0''.003$	$-1''.805 \pm 0''.003$	$18.87 \pm 0.03$	$19.64 \pm 0.07$	$20.36 \pm 0.05$
C	$-0''.968 \pm 0''.003$	$-0''.676 \pm 0''.005$	$-0''.676 \pm 0''.005$	$19.22 \pm 0.02$	$20.22 \pm 0.09$	$20.74 \pm 0.09$
D	$+0''.536 \pm 0''.003$	$-0''.427 \pm 0''.003$	$-0''.427 \pm 0''.003$	$20.64 \pm 0.06$	$22.00 \pm 0.22$	$22.94 \pm 0.13$
G	$-0''.183 \pm 0''.004$	$-0''.858 \pm 0''.004$	$-0''.858 \pm 0''.004$	$17.23 \pm 0.04$	$19.39 \pm 0.06$	$20.83 \pm 0.03$

Table 3.1. *HST* Astrometry and Photometry of SDSS0924+0219

$f_{M/L}$	Convergence $\kappa$				Shear $\gamma$				$\kappa_*/\kappa$			
	A	B	C	D	A	B	C	D	A	B	C	D
0.1	0.74	0.71	0.77	0.75	0.24	0.21	0.29	0.28	0.020	0.018	0.024	0.021
0.2	0.67	0.65	0.70	0.67	0.30	0.26	0.37	0.36	0.042	0.038	0.050	0.044
0.3	0.61	0.59	0.64	0.61	0.35	0.30	0.44	0.43	0.061	0.055	0.072	0.062
0.4	0.53	0.51	0.56	0.53	0.42	0.36	0.53	0.52	0.11	0.10	0.13	0.11
0.5	0.47	0.45	0.49	0.46	0.48	0.41	0.61	0.60	0.15	0.14	0.17	0.15
0.6	0.40	0.38	0.44	0.41	0.54	0.45	0.69	0.67	0.19	0.18	0.23	0.20
0.7	0.31	0.29	0.35	0.31	0.62	0.51	0.80	0.77	0.34	0.32	0.38	0.34
0.8	0.25	0.23	0.29	0.26	0.67	0.55	0.88	0.84	0.45	0.42	0.50	0.46
0.9	0.17	0.16	0.22	0.18	0.73	0.61	0.96	0.92	0.72	0.70	0.77	0.73
1.0	0.13	0.12	0.17	0.13	0.77	0.64	1.02	0.98	1.00	1.00	1.00	1.00

Note. — Convergence  $\kappa$ , shear  $\gamma$  and the fraction of the total surface density composed of stars  $\kappa_*/\kappa$  at each image location for the series of macroscopic mass models.

Table 3.2. Macroscopic Lens Mass Models

HJD	$\chi^2/N_{dof}$	Seeing	QSO A	QSO B	QSO C	QSO D	$\langle \text{Stars} \rangle$
2957.814	0.70	1''22	2.812 ± 0.028	3.515 ± 0.033	3.883 ± 0.054	5.041 ± 0.217	-0.032 ± 0.003
2964.789	0.65	1''42	2.864 ± 0.024	3.516 ± 0.024	3.895 ± 0.042	4.840 ± 0.144	0.004 ± 0.003
2976.775	0.64	1''31	2.800 ± 0.020	3.464 ± 0.022	3.892 ± 0.039	5.006 ± 0.149	-0.001 ± 0.003
2984.721	0.56	1''20	2.811 ± 0.036	3.453 ± 0.040	3.852 ± 0.068	4.632 ± 0.189	-0.037 ± 0.003
2991.791	0.79	1''08	2.766 ± 0.016	3.531 ± 0.019	3.991 ± 0.033	5.138 ± 0.128	0.012 ± 0.003
2995.932	1.82	1''20	2.785 ± 0.012	3.507 ± 0.013	3.928 ± 0.022	5.147 ± 0.105	0.084 ± 0.002
2998.787	1.31	0''94	2.804 ± 0.014	3.541 ± 0.017	4.047 ± 0.029	5.258 ± 0.120	0.027 ± 0.003
3022.797	1.82	1''09	2.882 ± 0.019	3.417 ± 0.018	4.161 ± 0.037	4.937 ± 0.116	0.015 ± 0.003
3029.751	2.13	0''90	2.865 ± 0.014	3.386 ± 0.015	4.187 ± 0.029	5.092 ± 0.092	0.021 ± 0.003
3036.673	0.70	0''99	2.780 ± 0.016	3.441 ± 0.019	4.216 ± 0.042	5.209 ± 0.144	0.004 ± 0.003
3047.794	0.94	1''31	2.749 ± 0.024	3.408 ± 0.024	4.331 ± 0.063	5.033 ± 0.193	-0.013 ± 0.003
3055.689	0.68	1''13	2.819 ± 0.009	3.555 ± 0.012	4.206 ± 0.020	5.353 ± 0.071	-0.025 ± 0.002
3056.744	0.80	1''11	2.757 ± 0.016	3.428 ± 0.017	4.201 ± 0.036	5.152 ± 0.133	0.016 ± 0.003
3064.680	1.30	1''08	2.836 ± 0.018	3.381 ± 0.018	4.187 ± 0.039	4.948 ± 0.119	0.010 ± 0.003
3065.805	0.61	1''28	2.832 ± 0.018	3.389 ± 0.017	4.179 ± 0.039	4.560 ± 0.091	0.080 ± 0.002
3071.649	0.53	1''08	2.800 ± 0.033	3.423 ± 0.039	4.269 ± 0.092	4.782 ± 0.206	-0.044 ± 0.003
3075.774	4.24	1''07	2.828 ± 0.012	3.491 ± 0.013	4.005 ± 0.022	5.046 ± 0.091	0.053 ± 0.002
3078.586	0.57	1''14	2.791 ± 0.019	3.446 ± 0.020	4.234 ± 0.045	4.888 ± 0.128	0.007 ± 0.003
3080.834	0.56	1''31	2.797 ± 0.017	3.419 ± 0.016	4.268 ± 0.041	4.742 ± 0.098	-0.002 ± 0.003
3087.648	1.49	0''86	2.770 ± 0.007	3.408 ± 0.008	4.294 ± 0.012	5.384 ± 0.043	0.188 ± 0.003

(cont'd)

Table 3.3. SDSS 0924+0219 Light curves

Table 3.3—Continued

HJD	$\chi^2/N_{dof}$	Seeing	QSO A	QSO B	QSO C	QSO D	$\langle \text{Stars} \rangle$
3089.599	1.11	1"04	2.781 ± 0.016	3.409 ± 0.017	4.198 ± 0.036	5.150 ± 0.126	0.011 ± 0.003
3090.666	0.79	1"50	2.833 ± 0.018	3.336 ± 0.013	4.450 ± 0.041	4.372 ± 0.066	0.168 ± 0.003
3101.623	0.60	1"20	2.732 ± 0.033	3.417 ± 0.037	4.420 ± 0.103	4.567 ± 0.179	-0.049 ± 0.003
3108.511	2.18	1"02	2.710 ± 0.016	3.361 ± 0.018	4.213 ± 0.039	5.063 ± 0.129	0.009 ± 0.003
3115.562	1.11	1"19	2.697 ± 0.019	3.398 ± 0.020	4.273 ± 0.049	4.889 ± 0.140	0.003 ± 0.003
3127.473	0.88	0"92	2.702 ± 0.020	3.364 ± 0.025	4.249 ± 0.058	4.735 ± 0.133	-0.022 ± 0.003
3134.453	0.79	0"91	2.631 ± 0.021	3.467 ± 0.031	4.442 ± 0.080	4.861 ± 0.167	-0.035 ± 0.003
3141.510	0.82	1"10	2.653 ± 0.021	3.467 ± 0.025	4.348 ± 0.060	4.638 ± 0.131	-0.018 ± 0.003
3159.468	0.69	1"07	2.596 ± 0.024	3.484 ± 0.035	4.382 ± 0.087	5.053 ± 0.238	-0.044 ± 0.003
3169.462	0.79	1"28	2.635 ± 0.020	3.582 ± 0.025	4.269 ± 0.057	5.135 ± 0.200	-0.012 ± 0.003
3324.813	0.42	1"44	2.675 ± 0.030	3.882 ± 0.047	4.450 ± 0.099	5.528 ± 0.404	-0.032 ± 0.003
3327.800	0.74	1"46	2.740 ± 0.027	3.960 ± 0.042	4.429 ± 0.083	5.217 ± 0.265	-0.016 ± 0.003
3330.766	0.74	1"45	2.776 ± 0.037	4.050 ± 0.067	4.466 ± 0.118	5.129 ± 0.317	-0.038 ± 0.003
3344.723	0.89	1"43	2.767 ± 0.026	3.923 ± 0.039	4.628 ± 0.096	5.754 ± 0.399	-0.018 ± 0.003
3349.758	0.56	1"49	2.703 ± 0.032	3.953 ± 0.048	4.971 ± 0.157	5.441 ± 0.384	-0.020 ± 0.003
3357.714	1.08	1"26	2.765 ± 0.021	3.869 ± 0.029	4.586 ± 0.069	5.674 ± 0.297	0.003 ± 0.003
3360.767	1.57	1"14	2.799 ± 0.020	3.841 ± 0.026	4.544 ± 0.056	5.306 ± 0.192	0.007 ± 0.003
3376.734	1.05	1"15	2.780 ± 0.019	3.926 ± 0.029	4.533 ± 0.058	5.379 ± 0.202	0.006 ± 0.003
3382.701	0.61	1"17	2.772 ± 0.022	4.012 ± 0.039	4.674 ± 0.082	5.468 ± 0.255	-0.017 ± 0.003
3394.741	0.61	0"98	2.779 ± 0.030	3.919 ± 0.064	4.908 ± 0.168	5.616 ± 0.426	-0.044 ± 0.003

(cont'd)

Table 3.3—Continued

HJD	$\chi^2/N_{dof}$	Seeing	QSO A	QSO B	QSO C	QSO D	$\langle \text{Stars} \rangle$
3403.751	1.00	0'98	2.801 ± 0.018	3.934 ± 0.028	4.733 ± 0.062	5.107 ± 0.141	0.003 ± 0.003
3410.781	0.99	1'13	2.767 ± 0.019	3.905 ± 0.028	4.681 ± 0.066	5.257 ± 0.183	-0.001 ± 0.003
3427.737	0.55	1'32	2.705 ± 0.041	4.025 ± 0.085	5.074 ± 0.247	5.181 ± 0.399	-0.031 ± 0.003
3435.698	1.29	0'99	2.793 ± 0.019	3.872 ± 0.029	4.666 ± 0.063	5.155 ± 0.158	-0.013 ± 0.003
3443.698	1.45	1'29	2.783 ± 0.024	3.900 ± 0.033	4.692 ± 0.080	4.858 ± 0.161	-0.006 ± 0.003
3450.662	0.66	1'20	2.701 ± 0.038	3.763 ± 0.066	5.006 ± 0.224	6.019 ± 0.807	-0.031 ± 0.003
3461.643	0.62	1'46	2.703 ± 0.029	3.953 ± 0.045	4.965 ± 0.141	5.626 ± 0.424	-0.025 ± 0.003
3468.550	0.95	1'28	2.766 ± 0.024	3.930 ± 0.035	4.732 ± 0.087	5.106 ± 0.200	-0.020 ± 0.003
3477.514	0.49	1'08	2.676 ± 0.024	3.846 ± 0.044	4.604 ± 0.099	5.900 ± 0.482	-0.033 ± 0.003
3490.481	0.77	1'06	2.670 ± 0.019	3.825 ± 0.030	4.689 ± 0.073	4.799 ± 0.136	-0.010 ± 0.003
3502.497	1.13	1'06	2.632 ± 0.020	3.776 ± 0.031	4.662 ± 0.075	4.938 ± 0.161	-0.013 ± 0.003
3520.515	0.85	1'34	2.520 ± 0.025	3.763 ± 0.038	4.739 ± 0.112	5.261 ± 0.306	-0.024 ± 0.003
3528.450	0.77	1'13	2.587 ± 0.027	3.743 ± 0.048	4.901 ± 0.152	5.322 ± 0.343	-0.034 ± 0.003

(cont'd)

Table 3.3—Continued

HJD	$\chi^2/N_{dof}$	Seeing	QSO A	QSO B	QSO C	QSO D	$\langle \text{Stars} \rangle$
3676.836	0.50	1".40	2.185 ± 0.020	3.529 ± 0.033	4.584 ± 0.114	5.174 ± 0.306	-0.030 ± 0.003
3686.836	0.77	1".22	2.120 ± 0.015	3.518 ± 0.025	4.375 ± 0.066	5.295 ± 0.258	-0.014 ± 0.003
3696.825	0.54	1".31	2.101 ± 0.025	3.614 ± 0.059	4.354 ± 0.140	5.088 ± 0.403	-0.043 ± 0.003
3704.817	0.76	1".13	2.184 ± 0.014	3.520 ± 0.022	4.364 ± 0.057	4.969 ± 0.164	-0.006 ± 0.003
3711.988	13.28	0".99	2.221 ± 0.007	3.538 ± 0.008	3.909 ± 0.011	5.206 ± 0.046	0.180 ± 0.003
3712.791	1.23	1".03	2.213 ± 0.013	3.505 ± 0.020	4.220 ± 0.044	5.099 ± 0.162	-0.001 ± 0.003
3719.804	0.54	1".13	2.173 ± 0.019	3.586 ± 0.041	4.506 ± 0.109	5.092 ± 0.279	-0.041 ± 0.003

Note. — HJD is the Heliocentric Julian Day – 2450000 days. The goodness of fit of the image,  $\chi^2/N_{dof}$ , is used to rescale the formal uncertainties when greater than unity (see text). The QSO A-D columns give the magnitudes of the quasar images relative to the comparison stars. The  $\langle \text{Stars} \rangle$  column gives the mean magnitude of the standard stars for that epoch relative to their mean for all epochs.

## CHAPTER 4

# SIMULTANEOUS ESTIMATION OF TIME DELAYS AND QUASAR STRUCTURE

### 4.1. INTRODUCTION

Variability in lensed quasar images comes from two very different sources. Changes in the quasar's intrinsic luminosity are observable as correlated, achromatic variability between images, while microlensing by the stars in the lens galaxy produces uncorrelated, chromatic variability. Measurements of the time delays between the lensed images from the correlated variability can be used to study cosmology (e.g. Refsdal 1964 and recently Saha et al. 2006; Oguri 2007) or the distribution of dark matter in the lens galaxy (e.g. Kochanek et al. 2006; Poindexter et al. 2007; Vuissoz et al. 2007). The microlensing variability can be used to study the structure of the quasar continuum emission region, the masses of the stars in the lens galaxy, and the stellar mass fraction near the lensed images (Schechter & Wambsganss 2002; Wambsganss 2006). It is now possible to use microlensing to measure the correlation of accretion disk size with black hole mass (Morgan et al. 2007), the wavelength dependence of the size of the accretion disk (Poindexter,

Morgan & Kochanek 2008) or the differing sizes of the thermal and non-thermal X-ray emission regions (Pooley et al. 2007; Dai et al. 2008).

The challenge is that most lensed quasars exhibit both intrinsic and microlensing variability. To measure a time delay, one must successfully model and remove the microlensing variability such that only intrinsic variability remains. If the microlensing variability has a sufficiently low amplitude or long timescale, it can be ignored (e.g. PG1115–080, Schechter et al. 1997), but this is a dangerous assumption for many systems. Eigenbrod et al. (2005) found that for an 80 day delay, adding microlensing perturbations with an amplitude of 5% (10%) to a light curve increased the uncertainty in the time delay by a factor of 2 (6). Existing time delay analyses for lenses with microlensing (e.g. Ofek & Maoz 2003; Paraficz et al. 2006; Kochanek et al. 2006; Poindexter et al. 2007) depend on the intrinsic and microlensing variability having different time scales. These analyses also require that the microlensing variability can be modeled by a simple polynomial function. This approach will clearly fail if the two sources of variability have similar time scales or if the microlensing variability cannot be easily parameterized. In their analysis of HE1104–1805, Ofek & Maoz (2003) used simulations of the the estimated microlensing variability to estimate its influence on the uncertainty in the delay measurement.

In this paper, we present a new technique for simultaneously estimating the time delay and size of the continuum emission region of lensed quasars that

exhibit strong microlensing. In essence, we assume a range of time delays and then determine the likelihood of the implied microlensing variability using the Bayesian Monte Carlo method of Kochanek (2004, see also Kochanek et al. 2007). This allows us to estimate the time delays and the quasar structural parameters simultaneously and include the effects of both phenomena on the parameter uncertainties. We apply the method to the two doubly-imaged lenses HE1104–1805 (Wisotzki et al. 1993) and QJ0158–4325 (Morgan et al. 1999). While HE1104–1805 has a well-measured time delay (Wyrzykowski et al. 2003; Ofek & Maoz 2003; Poindexter et al. 2007), the amplitude of the microlensing ( $\sim 0.05 \text{ mag yr}^{-1}$  over the past decade) and the fact that it exhibits variability on the 6 month scale of the time delay suggest that it is close to the limit where microlensing polynomial fitting methods (Burud et al. 2001; Kochanek et al. 2006) will break down. QJ0158–4325 clearly shows both correlated and uncorrelated variability, but the polynomial methods cannot reliably produce a time delay estimate. We describe the data and our models in §4.2, our new approach in §4.3 and the application to the two systems in §4.4. In § 4.5, we discuss the results and their limitations. We assume a flat  $\Omega_0 = 0.3$ ,  $\Lambda_0 = 0.7$ ,  $H_0 = 70 \text{ km s}^{-1} \text{ Mpc}^{-1}$  cosmology and that the lens redshift of QJ0158–4325 is  $z_l = 0.5$ . Reasonable changes in this assumed redshift have negligible consequences for the results.

## 4.2. OBSERVATIONS AND MODELS

We monitored QJ0158–4325 in the  $R$ -band using the SMARTS 1.3m telescope with the ANDICAM (DePoy et al. 2003)<sup>1</sup> optical/infrared camera ( $0''.369/\text{pixel}$ ) and using the 1.2m Euler Swiss Telescope ( $0''.344/\text{pixel}$ ). The Euler monitoring data was obtained as a part of the the COSMOGRAIL<sup>2</sup> project. A full description of our monitoring data reduction technique can be found in Kochanek et al. (2006), but we provide a brief summary here. We model the PSF of each quasar image using three nested, elliptical Gaussian components, keeping the relative astrometry fixed for all epochs. We use relative photometry, comparing the flux of each image to the flux of reference stars in each frame. For QJ0158–4325, we used 5 reference stars located at  $(-120''.6, -35''.0)$ ,  $(-40''.1, +137''.7)$ ,  $(+5''.2, -125''.1)$ ,  $(+81''.4, +108''.8)$  and  $(-86''.5, -78''.6)$  relative to image A with relative fluxes of  $1.0 : 0.568 : 0.437 : 0.136 : 0.0906$ , respectively. The lens galaxy flux is determined by optimizing its flux in observations with good seeing, and the light curves are then measured with the galaxy flux fixed to this optimal value. We eliminated all data points taken in seeing conditions worse than  $1''.7$ . Three points satisfying the seeing conditions and reported in Table 1 were not used in the analysis because the sky was too bright to measure the flux of image B accurately. The monitoring data are presented in Table 4.1, and the light curves

---

<sup>1</sup><http://www.astronomy.ohio-state.edu/ANDICAM/>

<sup>2</sup><http://www.cosmograil.org/>

are displayed in Figure 4.1. For HE1104–1805, we use the composite  $R$ - and  $V$ -band light curve data from Poindexter et al. (2007).

We created photometric models for the two systems from the WFPC2 and NICMOS  $V$ - (F555W),  $I$ - (F814W) and  $H$ -band (F160W) observations of the two systems by the CfA-Arizona Space Telescope Lens Survey (CASTLES<sup>3</sup>, Falco et al. 2001) following the methods of Lehár et al. (2000). The quasars are modeled as point sources and each lens galaxy as a de Vaucouleurs profile. We chose the de Vaucouleurs profile above other models since it provided the best fit. Table 4.2 summarizes the fits we use here, where the HE1104–1805 model is updated from that in Lehár et al. (2000) using a deeper  $H$ -band image obtained to study the quasar host galaxy (Yoo et al. 2006).

For each system we created a sequence of ten lens models using the *lensmodel* software package (Keeton 2001). Each model is the sum of concentric NFW (Navarro, Frenk & White 1996) and de Vaucouleurs components, where the NFW component simulates the dark matter halo and the de Vaucouleurs component represents the galaxy’s stellar content. We parameterize the model sequence by  $f_{M/L}$ , the mass of the stellar component relative to its mass in a constant mass-to-light ratio model with no contribution from the NFW halo. We generated model sequences covering the range  $0.1 \leq f_{M/L} \leq 1.0$ . With their time delay measurement, Poindexter et al. (2007) constrained the stellar mass fraction of HE1104–1805 to  $f_{M/L} = 0.30^{+0.04}_{-0.05}$ ,

---

<sup>3</sup><http://cfa-www.harvard.edu/glensdata/>

but we chose not to apply these limits to  $f_{M/L}$  for our present calculations. From these models for the mass distribution we extract the convergence ( $\kappa$ ), shear ( $\gamma$ ) and stellar surface density ( $\kappa_*$ ) for each image and then generate realizations of the microlensing magnification patterns at the location of each image using a variant of the ray-shooting (Schneider et al. 1992) method described in Kochanek (2004). A summary of the microlensing parameters is presented in Table 4.3. We assume a stellar mass function of  $dN(M)/dM \propto M^{-1.3}$  with a dynamic range of 50, which approximates the Galactic stellar mass function of Gould (2000). We present the results either making no assumption about the mean mass  $\langle M \rangle$  of the stars or by applying a prior that it lies in the range  $0.1 M_\odot \leq \langle M \rangle \leq 1.0 M_\odot$ . We used  $4096^2$  microlensing magnification patterns with an outer scale of  $20R_E$ . We used a prior for the relative motions of the observer, lens galaxy, lens galaxy stars and the source based on the projection of the CMB dipole (Kogut et al. 1993) for the observer, the stellar velocity dispersion of the lens set by its Einstein radius, and rms peculiar velocities for the lens and source of  $\sigma_p = 235/(1+z)$  km s $^{-1}$  (Kochanek 2004). We modeled the continuum emission source as a face-on thin accretion disk (Shakura & Sunyaev 1973) with the surface brightness profile

$$I(R) \propto \left\{ \exp \left[ (R/r_s)^{3/4} \right] - 1 \right\}^{-1}. \quad (4.1)$$

The scale radius  $r_s$  is the point where the disk temperature matches the rest frame wavelength of our monitoring band,  $kT = hc(1+z_s)/\lambda_{obs}$ . We really measure

a projected disk area with microlensing, so the true disk size will scale with inclination  $r_s \propto 1/h_{70}\sqrt{\cos i}$  for inclination angle  $i$  and  $H_0 = 70 \text{ km sec}^{-1} \text{ Mpc}^{-1}$ . For comparisons of these results to the predictions of other accretion disk models, the half-light radius of  $R_{1/2} = 2.44r_s$  should be used, since Mortonson et al. (2005) have shown that half-light radii estimated from microlensing depend little on the assumed surface brightness profile of the disk.

### 4.3. JOINT MONTE CARLO ANALYSIS

For our analysis we must generate light curve pairs with arbitrary delays. We always carry out the shifts on the less variable light curve (image A for both HE1104–1805 and QJ0158–4325). There are two issues for generating the light curves. First, we must define the algorithms for interpolating and extrapolating a light curve, and second we must decide how many extrapolated points should be used. When data points are shifted in the middle of an observing season, we estimate the flux at the shifted time using linear interpolation between the nearest bracketing data points. When shifted points lie in an inter-season gap or beyond either end of the observed lightcurve, we estimate the flux using extrapolation based on a linear fit to the five nearest data points. Data points requiring extrapolation for periods longer than seven days are discarded. We assign new uncertainties that combine the photometric errors with the uncertainties due to the temporal distance

of the new point from existing data points, where we model the source variability using the quasar structure function of Vanden Berk et al. (2004).

For a standard analysis, we wanted to use light curves with the same number of data points for each time delay and no points extrapolated by more than seven days. We limit the use of extrapolated points because they lead to a delay-dependent change in the statistical weights caused by the steadily growing probability distribution of the variance from the structure function. Given the delay range we wanted to test, we first found the limiting delay defined by the delay which yielded the minimum number of usable data points with our seven day extrapolation limit, leaving 242 epochs for HE1104–1805 and 102 epochs for QJ0158–4325. We then restricted all of the trial light curves to use only the epochs permissible at the limiting delay. For the very long delays of HE1104–1805, the limiting delay is not the longest delay, because the longest delays shift curves completely through the inter-season gaps. This forced us to restrict the HE1104–1805 analysis to the epochs permitted by both the limiting delay and the longest delay (219 total epochs), since some permissible times at the end of the limiting delay lightcurve are beyond the extrapolation limit in light curves with longer delays. We also experimented with simply allowing unlimited extrapolations; we compare the results for the two methods in § 4.4.

We then analyzed the light curves using the Bayesian Monte Carlo method of Kochanek (2004). In essence, we randomly select a time delay  $\Delta t$ , a lens model and

a disk model (size), generate a microlensing light curve and fit it to the microlensing light curve implied by the observed data and the selected time delay. This gives us a  $\chi^2$ -statistic for the goodness of fit for the trial  $\chi^2(\vec{p}, \Delta t)$  given the model parameters for the microlensing  $\vec{p} = (f_{M/L}, r_s, \text{velocities, masses etc.})$  and the time delay. Figure 4.1 shows an example of a good trial lightcurve fit to QJ 0158–4325 for a delay of  $\Delta t_{AB} = -20$  days. In essence, the probability of time delay  $\Delta t$  is the Bayesian integral

$$P(\Delta t|D) \propto \int P(D|\vec{p}, \Delta t)P(\vec{p})P(\Delta t)d\vec{p} \quad (4.2)$$

where  $P(D|\vec{p}, \Delta t)$  is the probability of fitting the data in a particular trial,  $P(\vec{p})$  sets the priors on the microlensing variables (see Kochanek 2004; Kochanek et al. 2007) and  $P(\Delta t)$  is the (uniform) prior on the time delay. The total probability is then normalized so that  $\int P(\Delta t|D)d\Delta t = 1$ . We evaluated the integral as a Monte Carlo sum over the trial light curves, where we created 4 independent sets of magnification patterns for each of the ten macroscopic mass models and generated  $4 \times 10^6$  trial light curves for each magnification pattern set.

#### 4.4. RESULTS

Poindexter et al. (2007) recently estimated a time delay for HE1104–1805 of  $\Delta t_{AB} = t_A - t_B = 152.2^{+2.8}_{-3.0}$  days, in the sense that image A lags image B, improving

on the earlier estimates by Ofek & Maoz (2003) and Wyrzykowski et al. (2003). The Poindexter et al. (2007) analysis used the Kochanek et al. (2006) polynomial method on light curves which combined the published data of Schechter et al. (2003), Ofek & Maoz (2003) and Wyrzykowski et al. (2003) with new  $R$ -band monitoring data. Poindexter et al. (2007) combined these data into a common light curve following the approach of Ofek & Maoz (2003). In this polynomial method, the source and microlensing variability are modeled as a set of Legendre polynomials that are then fit to the light curves. Ambiguities arise because the value of the delay depends weakly on the parameterization of the microlensing. Poindexter et al. (2007) used a Bayesian weighting scheme for the different polynomial orders, but obtained  $157.2 \pm 2.6$  days if they used the F-test to select among the different orders rather than a Bayesian weighting. The advantage of our present approach is that it uses a physical model for the microlensing rather than a polynomial parameterization of it.

We applied our joint Monte Carlo analysis technique to HE1104–1805 over a time interval range of  $125 \text{ days} \leq \Delta t_{AB} \leq 200 \text{ days}$  with a sampling in 1.5 day intervals and no extrapolation of the light curves past 7 days. Figs. 4.2 and 4.3 show the resulting probability distributions for the time delay and the disk size. We find a time delay of  $\Delta t_{AB} = t_A - t_B = 162.2_{-5.9}^{+6.3}$  days ( $1\sigma$ ) that is in marginal agreement with the formal Poindexter et al. (2007) result but in better agreement with the F-test selection of the best polynomial model than with the Bayesian result. Scaled to the mean disk inclination angle,  $\cos(i) = 1/2$ , the disk size estimate of

$\log[(r_s/\text{cm})\sqrt{\cos(i)/0.5}] = 15.7_{-0.5}^{+0.4}$  at  $0.2\ \mu\text{m}$  in the rest frame is little changed from the estimates in Morgan et al. (2007) and Poindexter, Morgan & Kochanek (2008) which held the delay fixed to the Poindexter et al. (2007) value. The uncertainties in the size are a factor of 1.6 larger in the present analysis. The difference in the source sizes at the redshifted centers of the  $V$ - and  $R$ -bands is small enough that the use of a composite lightcurve had little effect on the analysis (see Poindexter, Morgan & Kochanek 2008, for a detailed discussion of the wavelength dependence of microlensing in HE1104–1805). We also performed our analysis on a set of light curves generated with no limits on extrapolation, allowing some data points to be extrapolated for many months. The time delay and disk size estimates using these heavily extrapolated light curves show clear evidence of systematic problems, so we do not present these results.

In models of QJ0158–4325, we expect image A to lead image B by 2–3 weeks depending on the mass distribution and the actual lens redshift (we assumed  $z_l = 0.5$ ). For completeness, we tested a full range of negative and positive delays  $-50\ \text{days} \leq \Delta t_{AB} \leq 50\ \text{days}$  at 2 day intervals. We generated the positive and negative delay light curves separately in order to minimize the number of points lost due to the 7 day extrapolation limit at the price of making the data used for positive and negative delays somewhat different. For comparison, we also tried using all points with no extrapolation limits.

Figs. 4.4 – 4.6 show the results for the time delays and the source size. We have clearly failed to measure a time delay, and positive delays  $\Delta t_{AB} = t_A - t_B$  seem to be favored over negative delays, in direct disagreement with the predictions of the lens model. The relative likelihoods of positive and negative delays depend on the detailed treatment of the light curves, with the probability of positive delays being lower when we use all extrapolated points rather than restricting them to 7 days or less. In this case, the microlensing simply overwhelms the intrinsic variability. We expect additional monitoring data to continue to tighten the time delay probability distribution, but a successful delay measurement may not be possible for many seasons. We succeed, however, in estimating a size for the quasar despite the uncertainties in the time delay, finding a size of  $\log[(r_s/\text{cm})\sqrt{\cos(i)/0.5}] = 14.9 \pm 0.3$  at  $0.3 \mu\text{m}$  in the rest frame. The size estimate changes little compared to the uncertainties if we limit the analysis to either positive or negative delays. The microlensing amplitudes are large enough that interpreting varying amounts of the lower amplitude intrinsic variability as microlensing does not change the statistics of the microlensing enough to significantly affect the size estimate. One additional uncertainty in this result is that lens redshift of QJ0158–4325 is unknown. We experimented with running the Monte Carlo simulation at a range of lens redshifts ( $0.1 \leq z_l \leq 0.9$ ), and we found that the resulting shifts in the  $r_s$  estimates were negligible relative to the size of the existing uncertainties.

## 4.5. DISCUSSION AND CONCLUSIONS

Peng et al. (2006) used the width of the C IV ( $\lambda 1549\text{\AA}$ ) emission line to estimate the black hole mass  $M_{BH} = 2.37 \times 10^9 M_{\odot}$  in HE1104–1805 and the width of Mg II ( $\lambda 2798\text{\AA}$ ) emission line to estimate the black hole mass  $M_{BH} = 1.6 \times 10^8 M_{\odot}$  in QJ0158–4325. Using these black hole masses, the quasar accretion disk size - black hole mass relation of Morgan et al. (2007) predicts source sizes at  $2500\text{\AA}$  of  $\log[(r_s/\text{cm})\sqrt{\cos(i)/0.5}] = 15.9 \pm 0.2$  for HE1104–1805 and  $\log[(r_s/\text{cm})\sqrt{\cos(i)/0.5}] = 15.2 \pm 0.2$  for QJ0158–4325. If we scale our current disk size measurements to  $2500\text{\AA}$  using the  $R_{\lambda} \propto \lambda^{4/3}$  scaling of thin disk theory, we find  $\log[(r_s/\text{cm})\sqrt{\cos(i)/0.5}] = 15.9_{-0.5}^{+0.4}$  for HE1104–1805 and  $\log[(r_s/\text{cm})\sqrt{\cos(i)/0.5}] = 14.8 \pm 0.3$  for QJ0158–4325, fully consistent with the predictions of the Morgan et al. (2007) accretion disk size - black hole mass relation.

The mixing of intrinsic and microlensing variability in lensed quasar light curves can be a serious problem for estimating time delays (e.g. Eigenbrod et al. 2005) and previous microlensing analyses have been restricted to lenses with known time delays. In HE1104–1805, which must be close to the limits of measuring time delays in the presence of microlensing, we confirm that the approach of fitting polynomial models for the microlensing works reasonably well. However, the dependence of the delay on the assumed model was a warning sign that the formal errors on the delays were likely to be underestimates, as was recognized by Ofek & Maoz (2003)

and Poindexter et al. (2007). In our new, non-parametric microlensing analysis of HE1104–1805, we find a modestly longer delay of  $162.2_{-5.9}^{+6.3}$  days that quantifies those concerns. Estimates of the quasar accretion disk size are little affected by these small shifts in the time delay. In QJ0158–4325, the microlensing amplitude is larger relative to the intrinsic variability, and traditional methods for determining delays fail. Our new method also fails to measure a delay, but it does allow us to measure the size of the quasar accretion disk despite the uncertainties in the time delay.

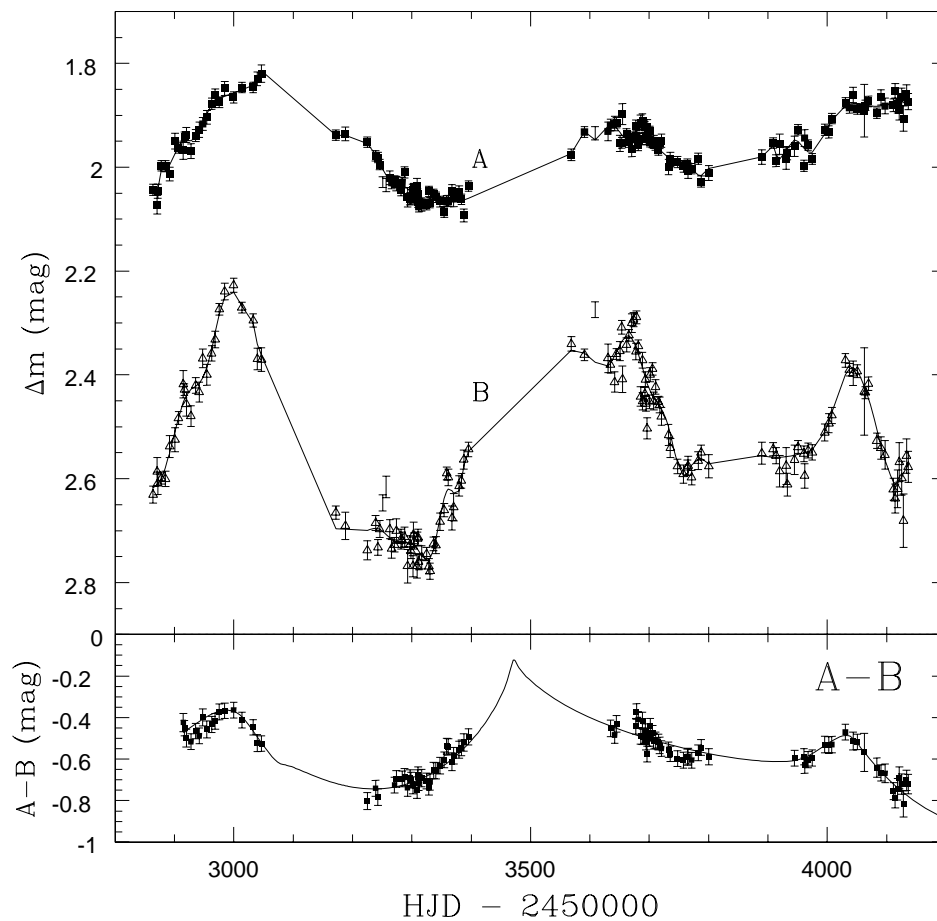


Fig. 4.1.— Top Panel: QJ0158–4325 *R*-band light curves for images A (squares) and B (triangles). The curves are a polynomial fit to guide the eye. Points with error bars only (no symbols) were not used in the analysis. Lower Panel: Example of a good fit to the implied A–B microlensing signal for a trial time delay of  $\Delta t_{AB} = -20$  days.

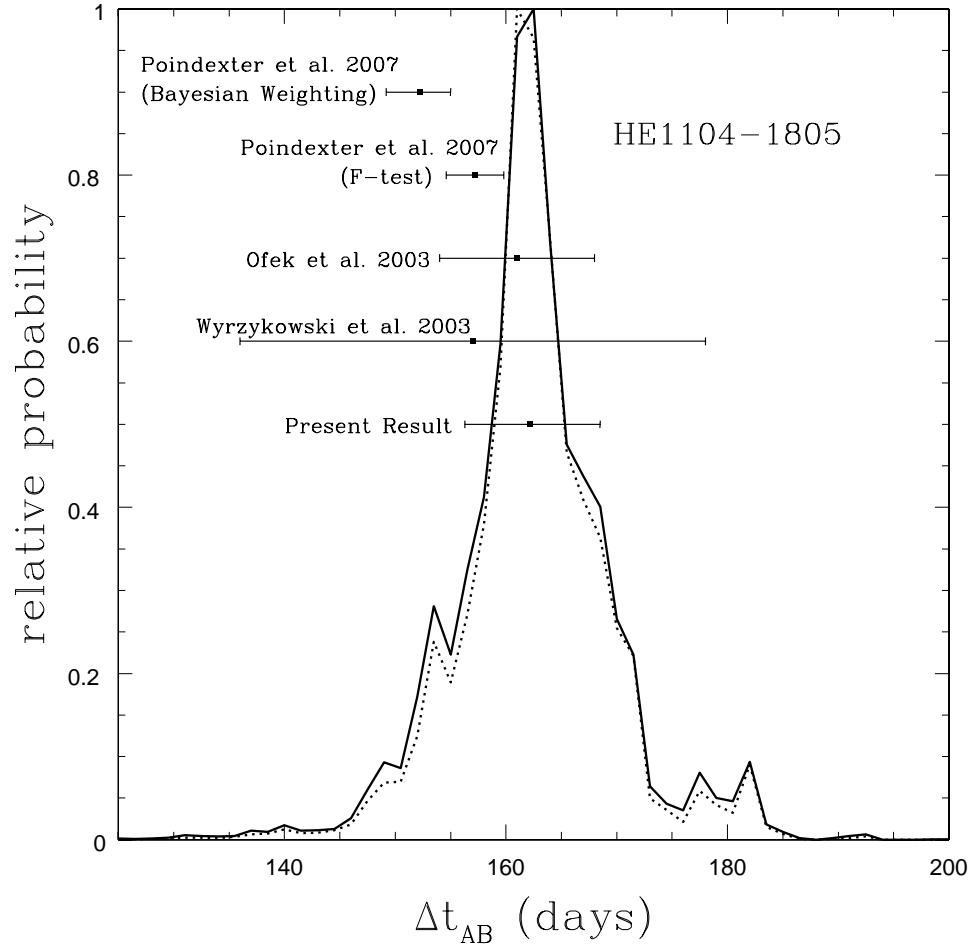


Fig. 4.2.— Probability distribution for the time delay of HE1104-1805, where  $\Delta t_{AB} = t_A - t_B$ . The solid curve has no prior on the microlens mass scale while the dotted curve assumes a uniform prior on the mass over the range  $0.1 M_{\odot} \leq \langle M \rangle \leq 1.0 M_{\odot}$ . Previous measurements of the time delay are also plotted with their  $1\sigma$  error bars. The dependence of the Poindexter et al. (2007) results on the statistical test used demonstrates the limitations of polynomial fitting methods.

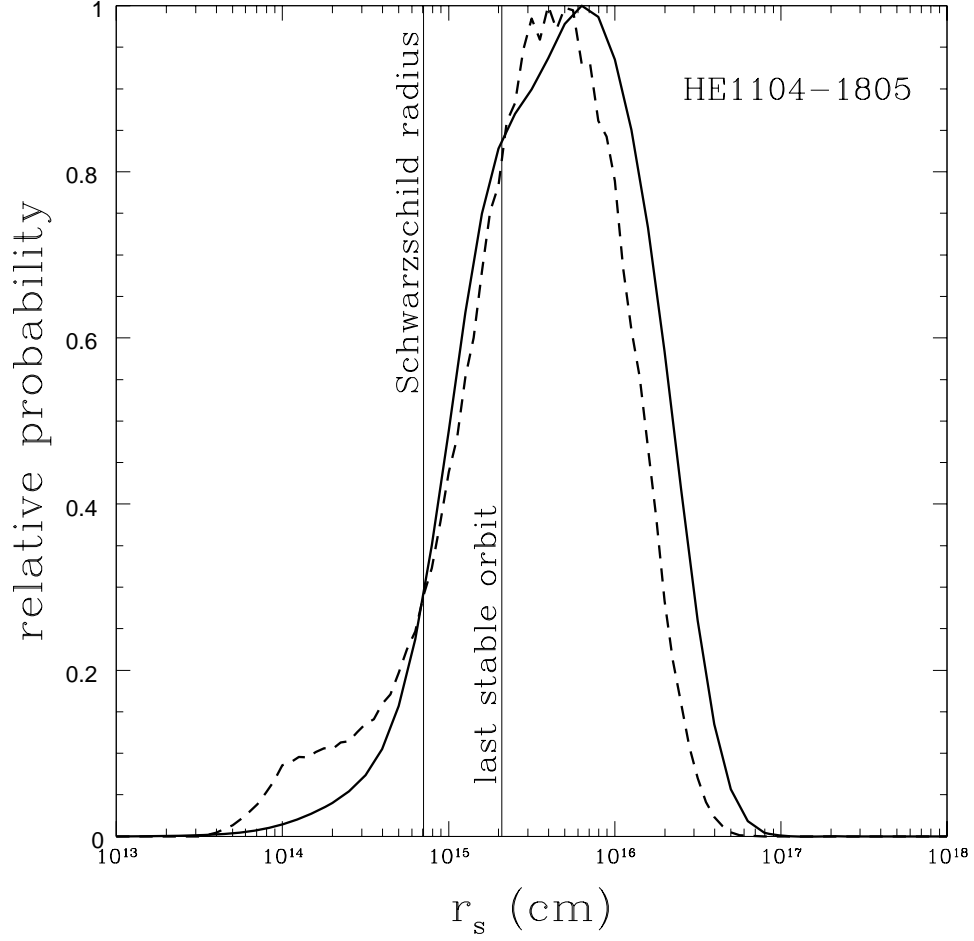


Fig. 4.3.— Probability distributions for the source size  $r_s$  of HE1104–1805. The dashed curve shows the estimate for  $r_s$  with a prior of  $0.1 M_\odot \leq \langle M \rangle \leq 1.0 M_\odot$  on the mean mass of the microlenses. The vertical line shows the Schwarzschild radius  $R_{BH} = 2GM_{BH}/c^2$  of the black hole, where the black hole mass  $M_{BH} = 2.37 \times 10^9 M_\odot$  was estimated by Peng et al. (2006) using the C IV emission line width. The last stable orbit for a Schwarzschild black hole is at  $3R_{BH}$ .

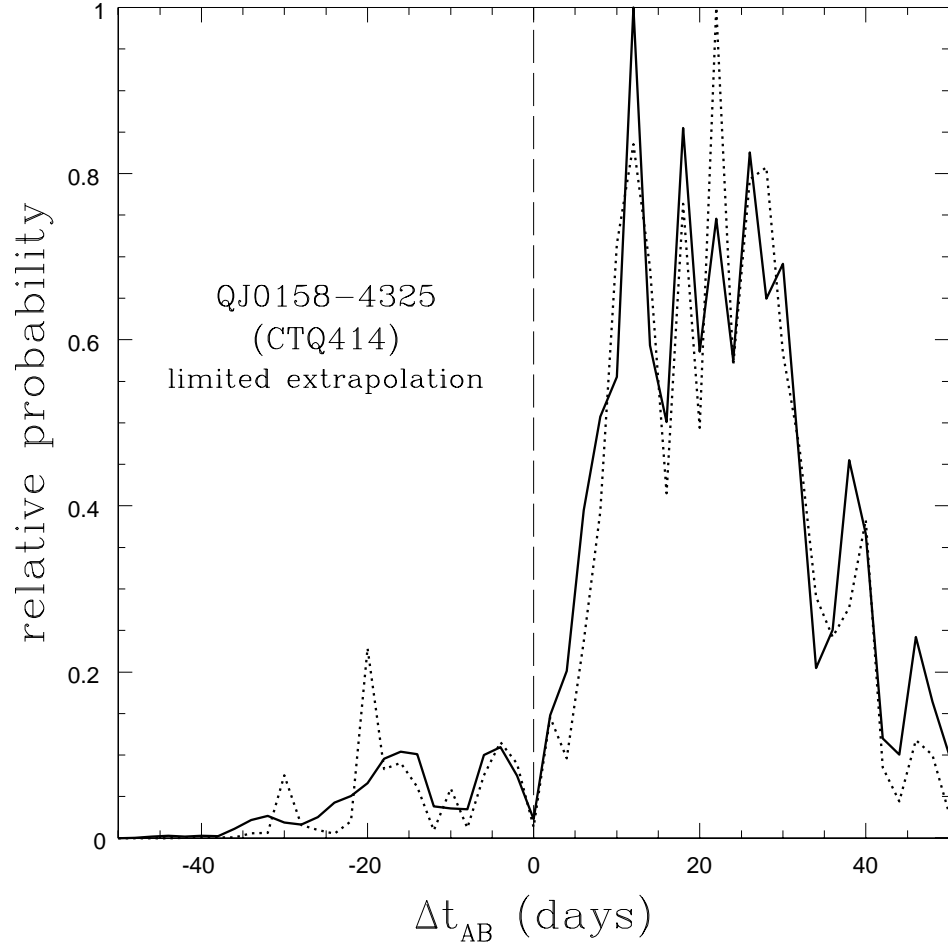


Fig. 4.4.— Probability distribution for the time delay  $\Delta t_{AB} = t_A - t_B$  in QJ0158–4325, where we restrict the extrapolation of the light curves to be less than 7 days. The solid curve assumes no prior on the microlens mass and the dashed curve assumes a uniform prior over the range  $0.1 M_\odot \leq \langle M \rangle \leq 1.0 M_\odot$ .

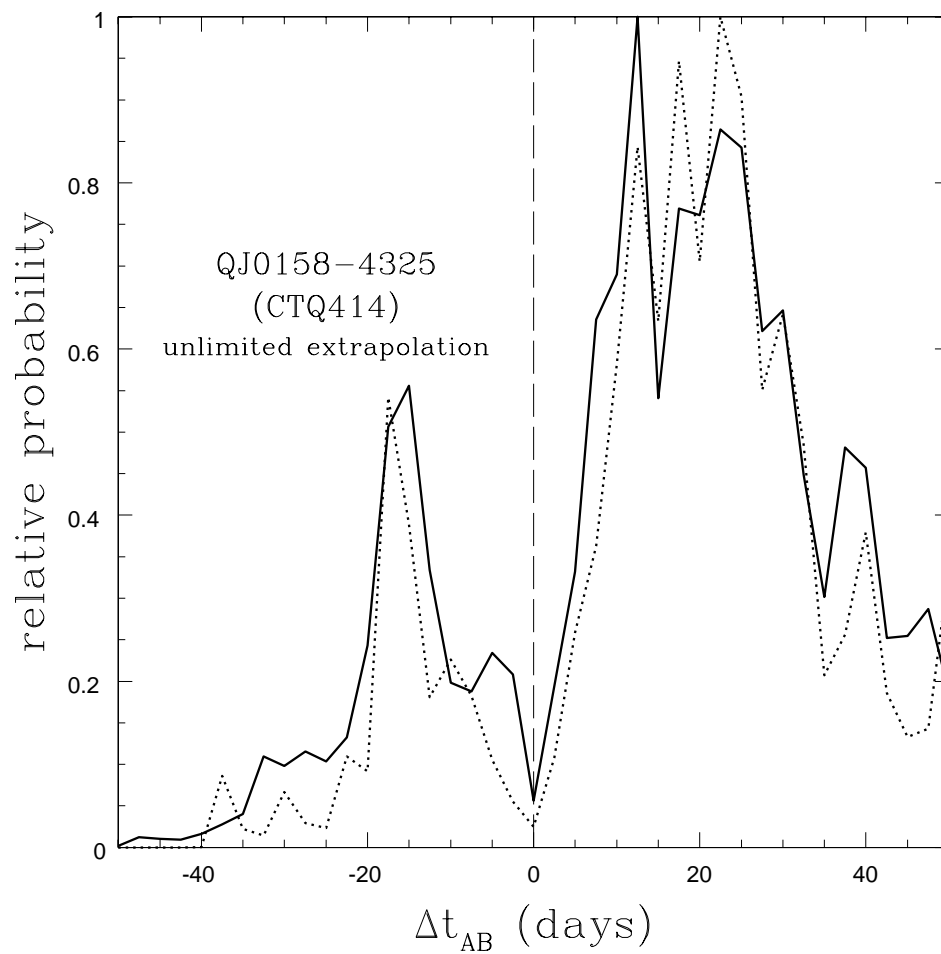


Fig. 4.5.— Same as Fig. 4.4, but the trial light curves were generated with no limits on extrapolation. Note the change in the relative probability of positive and negative delays.

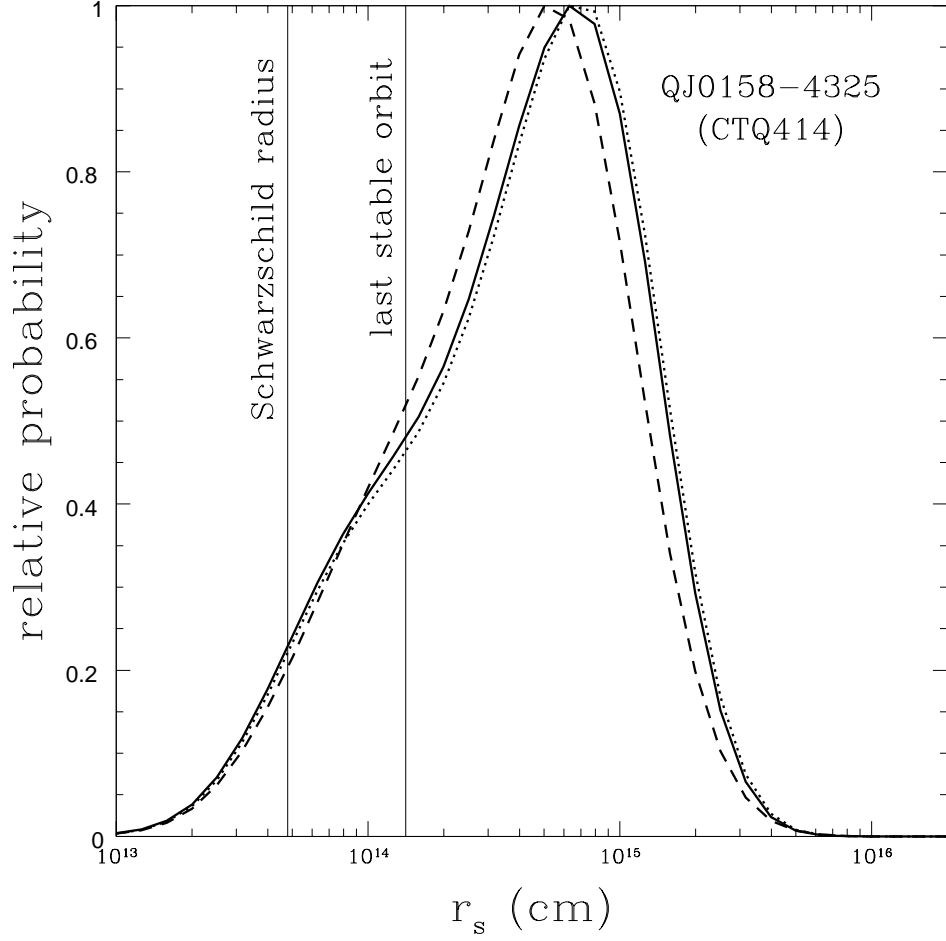


Fig. 4.6.— Probability distributions for source size  $r_s$  of QJ0158-4325. The dashed (dotted) curve shows the estimate for  $r_s$  using the set of negative (positive) trial time delays. The solid curve is the  $r_s$  estimate using all trial time delays. The vertical line shows the Schwarzschild radius  $R_{BH} = 2GM_{BH}/c^2$  of the black hole, where the black hole mass  $M_{BH} = 1.6 \times 10^8 M_\odot$  was estimated by Peng et al. (2006) using the Mg II emission line width. The last stable orbit for a Schwarzschild black hole is at  $3R_{BH}$ .

HJD	$\chi^2/N_{dof}$	QSO A (mags)	QSO B (mags)	$\langle \text{Stars} \rangle$	Source
2863.873	1.17	$2.043 \pm 0.010$	$2.631 \pm 0.015$	$-0.044 \pm 0.003$	SMARTS
2870.788	1.93	$2.072 \pm 0.013$	$2.585 \pm 0.020$	$-0.050 \pm 0.003$	SMARTS
2871.813	0.66	$2.046 \pm 0.014$	$2.609 \pm 0.022$	$-0.052 \pm 0.003$	SMARTS
2877.772	1.01	$1.997 \pm 0.008$	$2.600 \pm 0.011$	$0.043 \pm 0.002$	SMARTS
2884.771	2.15	$1.998 \pm 0.007$	$2.600 \pm 0.010$	$0.053 \pm 0.002$	SMARTS
2891.770	0.83	$2.014 \pm 0.013$	$2.537 \pm 0.021$	$-0.055 \pm 0.003$	SMARTS
2900.798	2.26	$1.950 \pm 0.010$	$2.524 \pm 0.015$	$-0.024 \pm 0.003$	SMARTS
2906.761	1.75	$1.962 \pm 0.007$	$2.483 \pm 0.009$	$0.052 \pm 0.002$	SMARTS
2914.653	0.49	$1.968 \pm 0.018$	$2.417 \pm 0.026$	$-0.038 \pm 0.004$	SMARTS
2916.766	1.00	$1.942 \pm 0.008$	$2.429 \pm 0.011$	$0.018 \pm 0.003$	SMARTS
2919.787	0.55	$1.938 \pm 0.014$	$2.455 \pm 0.023$	$-0.064 \pm 0.003$	SMARTS
2927.729	2.38	$1.969 \pm 0.009$	$2.479 \pm 0.013$	$-0.005 \pm 0.003$	SMARTS
2935.680	2.25	$1.939 \pm 0.008$	$2.420 \pm 0.010$	$0.034 \pm 0.003$	SMARTS
2941.674	3.82	$1.928 \pm 0.008$	$2.433 \pm 0.010$	$0.046 \pm 0.003$	SMARTS
2947.635	0.73	$1.916 \pm 0.012$	$2.368 \pm 0.018$	$-0.038 \pm 0.003$	SMARTS
2954.626	0.85	$1.903 \pm 0.013$	$2.400 \pm 0.020$	$-0.050 \pm 0.003$	SMARTS
2962.598	1.28	$1.878 \pm 0.010$	$2.359 \pm 0.013$	$-0.018 \pm 0.003$	SMARTS
2968.621	3.01	$1.862 \pm 0.007$	$2.332 \pm 0.009$	$0.015 \pm 0.003$	SMARTS
2975.577	2.02	$1.875 \pm 0.007$	$2.273 \pm 0.008$	$0.036 \pm 0.003$	SMARTS
2984.541	3.28	$1.848 \pm 0.007$	$2.239 \pm 0.009$	$0.041 \pm 0.003$	SMARTS
2999.619	1.54	$1.866 \pm 0.009$	$2.227 \pm 0.011$	$0.032 \pm 0.003$	SMARTS
3013.587	0.92	$1.846 \pm 0.008$	$2.271 \pm 0.011$	$-0.012 \pm 0.003$	SMARTS
3032.567	1.70	$1.846 \pm 0.008$	$2.295 \pm 0.010$	$0.033 \pm 0.003$	SMARTS
3039.534	1.34	$1.830 \pm 0.011$	$2.369 \pm 0.018$	$-0.051 \pm 0.003$	SMARTS
3046.543	4.29	$1.820 \pm 0.008$	$2.371 \pm 0.011$	$0.030 \pm 0.003$	SMARTS
3171.930	0.92	$1.938 \pm 0.008$	$2.666 \pm 0.013$	$0.020 \pm 0.003$	SMARTS
3187.869	0.65	$1.934 \pm 0.013$	$2.694 \pm 0.026$	$-0.050 \pm 0.003$	SMARTS
3224.869	0.70	$1.950 \pm 0.010$	$2.743 \pm 0.018$	$-0.001 \pm 0.003$	SMARTS
3238.825	0.99	$1.977 \pm 0.009$	$2.688 \pm 0.014$	$0.031 \pm 0.003$	SMARTS
3242.777	0.76	$1.981 \pm 0.009$	$2.732 \pm 0.015$	$0.004 \pm 0.003$	SMARTS
3245.784	0.61	$1.994 \pm 0.010$	$2.698 \pm 0.016$	$-0.036 \pm 0.003$	SMARTS
3250.779	1.29	$(2.029 \pm 0.009)$	$(2.646 \pm 0.014)$	$-0.025 \pm 0.003$	SMARTS
3256.852	0.80	$(2.035 \pm 0.013)$	$(2.616 \pm 0.021)$	$-0.025 \pm 0.003$	SMARTS
3262.779	3.42	$2.020 \pm 0.007$	$2.697 \pm 0.010$	$0.048 \pm 0.002$	SMARTS
3265.790	1.82	$2.030 \pm 0.008$	$2.735 \pm 0.013$	$0.021 \pm 0.003$	SMARTS
3270.792	1.46	$2.027 \pm 0.008$	$2.727 \pm 0.011$	$0.038 \pm 0.003$	SMARTS
3273.731	1.68	$2.031 \pm 0.011$	$2.701 \pm 0.018$	$-0.029 \pm 0.003$	SMARTS
3281.769	1.52	$2.043 \pm 0.010$	$2.716 \pm 0.016$	$-0.017 \pm 0.003$	SMARTS

(cont'd)

Table 4.1. QJ0158–4325 Light curves

Table 4.1—Continued

HJD	$\chi^2/N_{dof}$	QSO A (mags)	QSO B (mags)	$\langle \text{Stars} \rangle$	Source
3283.759	1.65	$2.029 \pm 0.008$	$2.718 \pm 0.011$	$0.026 \pm 0.003$	SMARTS
3287.633	0.73	$2.009 \pm 0.011$	$2.715 \pm 0.019$	$0.004 \pm 0.003$	SMARTS
3292.735	2.96	$2.057 \pm 0.011$	$2.769 \pm 0.019$	$-0.017 \pm 0.003$	SMARTS
3296.721	2.25	$2.061 \pm 0.008$	$2.726 \pm 0.011$	$0.037 \pm 0.003$	SMARTS
3298.691	1.36	$2.060 \pm 0.008$	$2.740 \pm 0.012$	$0.028 \pm 0.003$	SMARTS
3301.686	0.84	$2.044 \pm 0.011$	$2.769 \pm 0.020$	$-0.039 \pm 0.003$	SMARTS
3302.791	0.98	$2.045 \pm 0.013$	$2.700 \pm 0.024$	$-0.104 \pm 0.003$	EULER
3303.690	0.80	$2.041 \pm 0.010$	$2.720 \pm 0.016$	$-0.036 \pm 0.003$	SMARTS
3308.686	2.29	$2.028 \pm 0.009$	$2.761 \pm 0.015$	$-0.101 \pm 0.003$	EULER
3309.642	0.58	$2.051 \pm 0.009$	$2.717 \pm 0.013$	$-0.007 \pm 0.003$	SMARTS
3310.580	1.51	$2.060 \pm 0.008$	$2.706 \pm 0.012$	$-0.048 \pm 0.002$	EULER
3311.639	1.88	$2.076 \pm 0.008$	$2.760 \pm 0.011$	$0.041 \pm 0.003$	SMARTS
3316.694	0.59	$2.071 \pm 0.013$	$2.752 \pm 0.022$	$-0.034 \pm 0.003$	SMARTS
3324.630	1.37	$2.072 \pm 0.008$	$2.745 \pm 0.011$	$0.028 \pm 0.003$	SMARTS
3328.616	0.66	$2.046 \pm 0.009$	$2.769 \pm 0.015$	$-0.002 \pm 0.003$	SMARTS
3330.629	1.05	$2.068 \pm 0.009$	$2.779 \pm 0.015$	$-0.013 \pm 0.003$	SMARTS
3336.600	0.88	$2.052 \pm 0.009$	$2.726 \pm 0.013$	$-0.015 \pm 0.003$	SMARTS
3340.603	0.96	$2.058 \pm 0.010$	$2.728 \pm 0.016$	$0.017 \pm 0.003$	SMARTS
3347.574	0.83	$2.065 \pm 0.010$	$2.685 \pm 0.017$	$0.007 \pm 0.003$	SMARTS
3354.564	1.45	$2.086 \pm 0.008$	$2.661 \pm 0.011$	$0.031 \pm 0.003$	SMARTS
3358.560	1.00	$2.064 \pm 0.009$	$2.592 \pm 0.012$	$0.004 \pm 0.003$	SMARTS
3361.553	0.73	$2.063 \pm 0.011$	$2.600 \pm 0.016$	$-0.023 \pm 0.003$	SMARTS
3367.572	0.62	$2.046 \pm 0.014$	$2.677 \pm 0.023$	$-0.048 \pm 0.003$	SMARTS
3370.582	2.26	$2.057 \pm 0.011$	$2.658 \pm 0.018$	$-0.012 \pm 0.003$	SMARTS
3379.581	0.55	$2.046 \pm 0.012$	$2.619 \pm 0.020$	$0.004 \pm 0.003$	SMARTS
3383.581	1.32	$2.062 \pm 0.009$	$2.604 \pm 0.012$	$0.021 \pm 0.003$	SMARTS
3387.563	0.63	$2.092 \pm 0.012$	$2.566 \pm 0.018$	$-0.025 \pm 0.003$	SMARTS
3395.547	0.86	$2.036 \pm 0.010$	$2.544 \pm 0.014$	$-0.045 \pm 0.003$	SMARTS
3568.889	1.66	$1.976 \pm 0.009$	$2.340 \pm 0.011$	$0.000 \pm 0.003$	SMARTS
3590.890	1.19	$1.932 \pm 0.008$	$2.362 \pm 0.010$	$0.020 \pm 0.003$	SMARTS
3608.820	4.55	$(1.928 \pm 0.006)$	$(2.267 \pm 0.007)$	$0.050 \pm 0.002$	EULER
3630.626	0.75	$1.929 \pm 0.018$	$2.370 \pm 0.027$	$-0.041 \pm 0.003$	SMARTS
3634.802	0.86	$1.918 \pm 0.011$	$2.382 \pm 0.016$	$-0.047 \pm 0.003$	SMARTS
3641.753	2.01	$1.916 \pm 0.010$	$2.414 \pm 0.014$	$0.007 \pm 0.003$	SMARTS
3644.792	0.91	$1.914 \pm 0.008$	$2.360 \pm 0.010$	$0.015 \pm 0.003$	SMARTS
3653.595	1.43	$1.953 \pm 0.009$	$2.309 \pm 0.011$	$-0.007 \pm 0.003$	SMARTS

(cont'd)

Table 4.1—Continued

HJD	$\chi^2/N_{dof}$	QSO A (mags)	QSO B (mags)	$\langle\text{Stars}\rangle$	Source
3661.717	0.77	$1.936 \pm 0.010$	$2.342 \pm 0.013$	$-0.052 \pm 0.003$	SMARTS
3665.707	0.91	$1.952 \pm 0.009$	$2.324 \pm 0.011$	$-0.023 \pm 0.003$	SMARTS
3670.620	1.53	$1.964 \pm 0.011$	$2.302 \pm 0.015$	$-0.005 \pm 0.003$	SMARTS
3673.595	0.81	$1.942 \pm 0.011$	$2.294 \pm 0.013$	$-0.020 \pm 0.003$	SMARTS
3677.661	3.41	$1.915 \pm 0.007$	$2.348 \pm 0.009$	$0.080 \pm 0.002$	EULER
3678.644	1.28	$1.939 \pm 0.009$	$2.290 \pm 0.011$	$0.017 \pm 0.003$	SMARTS
3681.643	0.88	$1.958 \pm 0.009$	$2.345 \pm 0.012$	$-0.011 \pm 0.003$	SMARTS
3685.668	5.14	$1.907 \pm 0.006$	$2.435 \pm 0.008$	$0.011 \pm 0.002$	EULER
3688.633	0.50	$1.944 \pm 0.011$	$2.373 \pm 0.015$	$-0.050 \pm 0.003$	SMARTS
3688.676	4.26	$1.903 \pm 0.006$	$2.444 \pm 0.008$	$0.000 \pm 0.002$	EULER
3692.631	2.72	$1.916 \pm 0.006$	$2.429 \pm 0.008$	$0.032 \pm 0.002$	EULER
3693.560	2.10	$1.941 \pm 0.008$	$2.409 \pm 0.010$	$0.012 \pm 0.003$	SMARTS
3694.631	2.43	$1.939 \pm 0.007$	$2.448 \pm 0.009$	$0.058 \pm 0.002$	EULER
3696.623	5.99	$1.916 \pm 0.006$	$2.496 \pm 0.008$	$0.087 \pm 0.002$	EULER
3700.648	2.38	$1.924 \pm 0.006$	$2.445 \pm 0.009$	$0.068 \pm 0.002$	EULER
3701.605	1.01	$1.951 \pm 0.010$	$2.400 \pm 0.013$	$-0.001 \pm 0.003$	SMARTS
3705.652	1.12	$1.952 \pm 0.009$	$2.389 \pm 0.011$	$0.019 \pm 0.003$	SMARTS
3707.707	2.82	$1.944 \pm 0.007$	$2.443 \pm 0.010$	$0.066 \pm 0.002$	EULER
3710.605	0.99	$1.957 \pm 0.010$	$2.424 \pm 0.014$	$0.008 \pm 0.003$	SMARTS
3715.694	2.21	$1.960 \pm 0.006$	$2.445 \pm 0.007$	$0.047 \pm 0.002$	EULER
3717.573	0.68	$1.953 \pm 0.010$	$2.459 \pm 0.015$	$-0.048 \pm 0.003$	SMARTS
3720.644	3.80	$1.942 \pm 0.007$	$2.473 \pm 0.009$	$-0.006 \pm 0.002$	EULER
3732.631	4.36	$1.992 \pm 0.007$	$2.509 \pm 0.010$	$0.067 \pm 0.002$	EULER
3735.616	4.39	$1.978 \pm 0.006$	$2.534 \pm 0.009$	$0.074 \pm 0.002$	EULER
3747.614	3.03	$1.983 \pm 0.006$	$2.569 \pm 0.008$	$0.014 \pm 0.002$	EULER
3757.606	1.92	$1.991 \pm 0.008$	$2.584 \pm 0.013$	$0.023 \pm 0.002$	EULER
3764.534	0.80	$1.994 \pm 0.010$	$2.579 \pm 0.015$	$-0.015 \pm 0.003$	SMARTS
3765.570	6.22	$2.000 \pm 0.006$	$2.568 \pm 0.007$	$0.080 \pm 0.002$	EULER
3771.604	2.31	$1.996 \pm 0.006$	$2.591 \pm 0.009$	$0.031 \pm 0.002$	EULER
3782.557	1.59	$1.977 \pm 0.008$	$2.558 \pm 0.013$	$-0.043 \pm 0.002$	EULER
3787.531	2.82	$2.020 \pm 0.006$	$2.542 \pm 0.009$	$0.035 \pm 0.002$	EULER
3800.519	2.23	$2.004 \pm 0.010$	$2.569 \pm 0.015$	$-0.044 \pm 0.002$	EULER
3889.922	2.68	$1.973 \pm 0.008$	$2.544 \pm 0.013$	$0.036 \pm 0.002$	EULER
3908.910	2.44	$1.946 \pm 0.006$	$2.536 \pm 0.008$	$0.070 \pm 0.002$	EULER
3913.839	2.94	$1.980 \pm 0.007$	$2.548 \pm 0.009$	$0.042 \pm 0.002$	EULER
3919.880	5.01	$1.949 \pm 0.009$	$2.578 \pm 0.014$	$-0.052 \pm 0.002$	EULER

(cont'd)

Table 4.1—Continued

HJD	$\chi^2/N_{dof}$	QSO A (mags)	QSO B (mags)	$\langle \text{Stars} \rangle$	Source
3930.856	0.49	$1.983 \pm 0.021$	$2.577 \pm 0.036$	$-0.001 \pm 0.004$	SMARTS
3932.920	1.40	$1.966 \pm 0.011$	$2.604 \pm 0.019$	$-0.072 \pm 0.002$	EULER
3950.832	2.46	$1.921 \pm 0.006$	$2.532 \pm 0.008$	$0.085 \pm 0.002$	EULER
3960.817	1.23	$1.997 \pm 0.010$	$2.552 \pm 0.014$	$-0.034 \pm 0.003$	SMARTS
3961.922	6.26	$1.937 \pm 0.006$	$2.587 \pm 0.009$	$0.030 \pm 0.002$	EULER
3967.838	0.85	$1.957 \pm 0.010$	$2.546 \pm 0.014$	$-0.003 \pm 0.003$	SMARTS
3974.783	1.11	$1.984 \pm 0.010$	$2.550 \pm 0.014$	$-0.009 \pm 0.003$	SMARTS
3995.765	0.88	$1.927 \pm 0.011$	$2.511 \pm 0.016$	$-0.019 \pm 0.003$	SMARTS
4002.702	1.03	$1.931 \pm 0.012$	$2.494 \pm 0.018$	$-0.023 \pm 0.003$	SMARTS
4007.696	0.70	$1.905 \pm 0.010$	$2.479 \pm 0.015$	$-0.013 \pm 0.003$	SMARTS
4030.632	0.82	$1.876 \pm 0.010$	$2.372 \pm 0.013$	$-0.003 \pm 0.003$	SMARTS
4037.600	0.92	$1.886 \pm 0.009$	$2.390 \pm 0.012$	$-0.008 \pm 0.003$	SMARTS
4043.600	0.48	$1.861 \pm 0.015$	$2.397 \pm 0.023$	$-0.056 \pm 0.003$	SMARTS
4050.620	1.34	$1.888 \pm 0.008$	$2.393 \pm 0.011$	$0.002 \pm 0.003$	SMARTS

(cont'd)

Table 4.1—Continued

HJD	$\chi^2/N_{dof}$	QSO A (mags)	QSO B (mags)	$\langle\text{Stars}\rangle$	Source
4062.536	0.47	$1.891 \pm 0.051$	$2.432 \pm 0.084$	$0.151 \pm 0.004$	SMARTS
4064.646	0.84	$1.881 \pm 0.009$	$2.434 \pm 0.012$	$0.006 \pm 0.003$	SMARTS
4069.580	0.82	$1.872 \pm 0.009$	$2.419 \pm 0.013$	$-0.036 \pm 0.003$	SMARTS
4083.542	0.69	$1.895 \pm 0.010$	$2.527 \pm 0.015$	$-0.019 \pm 0.003$	SMARTS
4090.621	2.29	$1.865 \pm 0.010$	$2.541 \pm 0.014$	$-0.025 \pm 0.003$	SMARTS
4097.556	0.40	$1.882 \pm 0.015$	$2.554 \pm 0.027$	$-0.045 \pm 0.003$	SMARTS
4111.601	1.23	$1.880 \pm 0.011$	$2.622 \pm 0.019$	$-0.016 \pm 0.003$	SMARTS
4114.561	1.08	$1.842 \pm 0.013$	$2.664 \pm 0.027$	$-0.024 \pm 0.003$	SMARTS
4118.593	0.48	$1.873 \pm 0.018$	$2.628 \pm 0.036$	$-0.044 \pm 0.003$	SMARTS
4121.529	0.57	$1.888 \pm 0.020$	$2.571 \pm 0.038$	$-0.044 \pm 0.003$	SMARTS
4125.526	0.66	$1.863 \pm 0.017$	$2.602 \pm 0.033$	$-0.043 \pm 0.003$	SMARTS
4128.574	0.51	$1.900 \pm 0.024$	$2.696 \pm 0.052$	$-0.039 \pm 0.003$	SMARTS
4133.581	0.45	$1.858 \pm 0.017$	$2.557 \pm 0.033$	$-0.046 \pm 0.003$	SMARTS
4136.572	0.49	$1.873 \pm 0.015$	$2.578 \pm 0.030$	$-0.061 \pm 0.003$	SMARTS
4301.869	1.05	$1.815 \pm 0.008$	$2.565 \pm 0.012$	$0.021 \pm 0.003$	SMARTS
4307.824	0.70	$1.794 \pm 0.009$	$2.571 \pm 0.016$	$-0.026 \pm 0.003$	SMARTS

Note. — HJD is the Heliocentric Julian Day – 2450000 days. The number of degrees of freedom  $N_{dof}$  is set by the number of pixels used in the photometric measurement. Typical values are  $N_{dof} = 6003$  for Euler and  $N_{dof} = 4482$  for SMARTS/ANDICAM. The goodness of fit of the image,  $\chi^2/N_{dof}$ , is used to rescale the formal uncertainties when greater than unity. The QSO A&B columns give the magnitudes of the quasar images relative to the comparison stars. The  $\langle\text{Stars}\rangle$  column gives the mean magnitude of the standard stars for that epoch relative to their mean for all epochs. A few points in the lightcurves (in parentheses) were not used in the analysis.

Lens	Component	Astrometry			Photometry		
		$\Delta RA$	$\Delta Dec$	H=F160W	I=F814W	V=F555W	
QJ0158-4325	A	$\equiv 0$	$\equiv 0$	$16.47 \pm 0.03$	$17.81 \pm 0.04$	$18.10 \pm 0.13$	
	B	$-1''.156 \pm 0''.003$	$-0''.398 \pm 0''.003$	$17.27 \pm 0.03$	$18.62 \pm 0.11$	$18.91 \pm 0.17$	
	G	$-0''.780 \pm 0''.016$	$-0''.234 \pm 0''.006$	$16.67 \pm 0.13$	$18.91 \pm 0.06$	$20.36 \pm 0.18$	
HE1104-1805	A	$\equiv 0$	$\equiv 0$	$15.91 \pm 0.01$	$16.40 \pm 0.03$	$16.92 \pm 0.06$	
	B	$+2''.901 \pm 0''.003$	$-1''.332 \pm 0''.003$	$17.35 \pm 0.03$	$17.95 \pm 0.04$	$18.70 \pm 0.08$	
	G	$+0''.965 \pm 0''.003$	$-0''.500 \pm 0''.003$	$17.52 \pm 0.09$	$20.01 \pm 0.10$	$23.26 \pm 0.27$	

Table 4.2. HST Astrometry and Photometry of QJ0158-4325 and HE1104-1805

Lens	$f_{M/L}$	$\kappa$		$\gamma$		$\kappa_*/\kappa$	
		A	B	A	B	A	B
QJ0158–4325	0.1	0.73	0.99	0.19	0.29	0.030	0.074
	0.2	0.66	0.96	0.22	0.38	0.064	0.15
	0.3	0.63	0.94	0.23	0.44	0.086	0.20
	0.4	0.54	0.89	0.28	0.57	0.15	0.32
	0.5	0.48	0.86	0.30	0.67	0.21	0.42
	0.6	0.42	0.82	0.32	0.76	0.30	0.54
	0.7	0.35	0.78	0.35	0.85	0.41	0.65
	0.8	0.29	0.75	0.37	0.94	0.57	0.78
	0.9	0.23	0.72	0.39	1.03	0.81	0.92
	1.0	0.20	0.70	0.41	1.08	1.00	1.00
HE1104–1805	0.1	0.86	0.58	0.26	0.18	0.036	0.012
	0.2	0.80	0.53	0.33	0.18	0.079	0.027
	0.3	0.73	0.47	0.40	0.19	0.12	0.044
	0.4	0.67	0.41	0.47	0.19	0.18	0.064
	0.5	0.61	0.35	0.53	0.20	0.24	0.093
	0.6	0.55	0.30	0.60	0.20	0.32	0.13
	0.7	0.49	0.25	0.67	0.20	0.41	0.18
	0.8	0.43	0.19	0.73	0.21	0.53	0.26
	0.9	0.37	0.14	0.80	0.21	0.68	0.40
	1.0	0.30	0.07	0.88	0.21	1.00	1.00

Note. — Convergence  $\kappa$ , shear  $\gamma$  and the fraction of the total surface density composed of stars  $\kappa_*/\kappa$  at each image location for the series of macroscopic mass models.

Table 4.3. Lens Galaxy Mass Models

## CHAPTER 5

# THE QUASAR ACCRETION DISK SIZE – BLACK HOLE MASS RELATION

### 5.1. INTRODUCTION

Despite nearly 40 years of work on accretion disk physics, the simple Shakura & Sunyaev (1973) thin disk model and its relativistic cousins (e.g. Page & Thorne 1974; Hubeny & Hubeny 1997; Li et al. 2005) remain the standard model despite many theoretical alternatives (e.g. Narayan, Barret & McClintock 1997; De Villiers, Hawley & Krolik 2003; Blaes 2007) and some observational reservations (see Francis et al. 1991; Koratkar & Blaes 1999; Collin et al. 2002). Quasar accretion disks cannot be spatially resolved with ordinary telescopes, so we have been forced to test accretion physics through time variability (e.g. Vanden Berk et al. 2004; Sergeev et al. 2005; Cackett, Horne & Winkler 2007) and spectral modeling (e.g. Sun & Malkan 1989; Collin et al. 2002; Bonning et al. 2007). One notable success is the use of reverberation mapping (Peterson et al. 2004) of quasar broad line emission to calibrate the relation between emission line widths and black hole masses. The line emission, though, comes from scales much larger than the accretion disk, and

attempts to use similar methods on the continuum emission have had limited success, largely because quasars show little optical variability on the the disk light-crossing timescale (Collin et al. 2002; Sergeev et al. 2005).

Gravitational telescopes do, however, provide the necessary resolution to study the structure of the quasar continuum source. Each gravitationally lensed quasar image is observed through a magnifying screen created by the stars in the lens galaxy. Sources that are smaller than the Einstein radius of the stars, typically  $\sim 10^{16}$  cm, show time variable fluxes whose amplitude is determined by the source size (see the review by Wambsganss 2006). Smaller sources have larger variability amplitudes than larger sources. In this paper, we exploit the optical microlensing variability observed in eleven gravitationally lensed quasar systems to measure the size of their accretion disks, and we find that disk sizes are strongly correlated with the masses of their central black holes.

In §5.2 we describe the monitoring data, the lens models we use based on Hubble Space Telescope (HST) images of each system and our microlensing analysis method. In §5.3 we describe our accretion disk model and our results for the relationship between disk size and black hole mass. While we analyze and discuss the results in terms of a simplified thin disk model, they can be compared to any other model by comparing our measurement of the half light radius to that expected from the model of choice because Mortonson et al. (2005) demonstrate that the half-light radius measured from microlensing is essentially independent of

the assumed disk surface brightness profile. The surface brightness profile is best probed by measuring the dependence of the microlensing amplitude on wavelength (see Poindexter, Morgan & Kochanek 2008). In §5.4, we discuss the results and their implications for thin accretion disk theory. All calculations in this paper assume a flat  $\Lambda$ CDM cosmology with  $h = 0.7$ ,  $\Omega_M = 0.3$  and  $\Omega_\Lambda = 0.7$ .

## 5.2. DATA AND ANALYSIS

We monitored the gravitationally lensed quasars QJ0158–4325, HE 0435–1223, SDSS 0924+0219, FBQ 0951+2635, SDSS 1004+4112, HE 1104–1805, PG 1115+080, RXJ 1131–1231, SDSS 1138+0314, SBS 1520+530 and Q 2237+030 in the  $r$ -,  $R$ - and  $V$ -bands on the SMARTS 1.3m using the ANDICAM optical/infrared camera (DePoy et al. 2003)<sup>1</sup>, the Wisconsin-Yale-Indiana (WIYN) observatory using the WIYN Tip–Tilt Module (WTTM)<sup>2</sup>, the 2.4m Hiltner telescope at the MDM Observatory using the MDM Eight-K<sup>3</sup>, Echelle and RETROCAM<sup>4</sup> (Morgan et al. 2005) imagers and the 6.5m Magellan Baade telescope using IMACS (Bigelow et al. 1999). We supplemented our monitoring data with published quasar light curves from Paraficz et al. (2006), Schechter et al. (1997), Wyrzykowski et al. (2003), Ofek & Maoz (2003), Gaynullina et al. (2005), Fohlmeister et al. (2007) and Morgan et

---

<sup>1</sup><http://www.astronomy.ohio-state.edu/ANDICAM/>

<sup>2</sup>[http://www.wiyn.org/wttm/WTTM\\_manual.html](http://www.wiyn.org/wttm/WTTM_manual.html)

<sup>3</sup><http://www.astro.columbia.edu/~arlin/MDM8K/>

<sup>4</sup><http://www.astronomy.ohio-state.edu/MDM/RETROCAM>

al. (2007). We measured the flux of each image by comparison to the flux from reference stars in the field of each lens. Our analysis of the monitoring data is described in detail by Kochanek et al. (2006). In systems with published time delays, we offset the lightcurves by the delays to eliminate the intrinsic source variability. SDSS 0924+0219, SDSS 1138+0314 and Q 2237+030 do not have published time delays but are all quadruply lensed quasars with short ( $\lesssim 15$  days) estimated delays. Since the typical timescale for microlensing is significantly longer than this ( $\gtrsim 1$  year), we ignored the delays in these systems and used their raw lightcurves in our microlensing analysis. For QJ0158–4325 we have developed an analysis method that allows us to simultaneously estimate the time delays and disk sizes including their mutual uncertainties, the details of which are described in Morgan et al. (2007).

All eleven lenses have been observed in the  $V$ - (F555W),  $I$ - (F814W) and  $H$ -bands (F160W) using the WFPC2, ACS/WFC and NICMOS instruments on *HST*. We fit these images as combinations of point sources for the quasars and (generally) de Vaucouleurs models for the lenses as described in Lehár et al. (2000). These provided the astrometry used for lens models and defined a constant mass-to-light ( $M/L$ ) ratio model for the mass distribution in the lens models. We modeled each system using the *GRAVLENS* software package (Keeton 2001). For all systems except the cluster lens SDSS 1004+4112, we generate a series of ten models starting from a constant  $M/L$  model and then add an NFW (Navarro, Frenk & White 1996) halo. The sequence is parameterized by  $f_{M/L}$ , the mass

fraction represented by the visible lens galaxy relative to a constant  $M/L$  model. In general, we start with the constant  $M/L$  model,  $f_{M/L} = 1$ , and then reduce its mass in increments of  $\Delta f_{M/L} = 0.1$  with the NFW halo's mass rising to compensate. For the cluster-lensed quasar SDSS 1004+4112, we use the fixed mass model from Fohlmeister et al. (2007), and we assume a set of 10 evenly spaced stellar mass fractions in the range  $0.1 \leq \kappa_*/\kappa \leq 1.0$ . Thus, our results average over the uncertainties in the dark matter halos of the lenses.

These lens models then provide the convergence  $\kappa$ , shear  $\gamma$  and stellar surface density  $\kappa_*$  needed to define the microlensing magnification patterns. We assume a lens galaxy stellar mass function  $dN(M)/dM \propto M^{-1.3}$  with a dynamic range of a factor of 50 that approximates the Galactic disk mass function of Gould (2000). For the typical lens we generated 4 magnification patterns for each image in each of the 10 lens models. We gave the magnification patterns an outer scale of  $20\langle R_E \rangle$ , where  $\langle R_E \rangle$  is the Einstein radius for the mean stellar mass  $\langle M \rangle$ . This outer dimension is large enough to fairly sample the magnification pattern while the pixel scale of the  $4096^2$  magnification patterns is small enough to resolve the accretion disk. We determined the properties of the accretion disk by modeling the observed light curves using the Bayesian Monte Carlo method of Kochanek (2004) (also see Kochanek et al. 2007). For a given disk model we randomly generate light curves, fit them to the observations and then use Bayesian methods to compute probability distributions for the disk size averaged over the lens models, the likely velocities of the observer,

lens, source, stars and the mass. We used the velocity model from Kochanek (2004), which used the projected CMB dipole (Kogut et al. 1993) for the observer, a stellar velocity dispersion set by the Einstein radius of the lens and peculiar velocity scales for the lens and source of  $235/(1+z)$  km s<sup>-1</sup>. We use a prior on the mean microlens mass of  $0.1M_{\odot} < \langle M \rangle < 1.0M_{\odot}$ , but the disk size estimates are insensitive to this assumption (see Kochanek 2004).

We use black hole mass estimates for the quasars that are based on observed quasar emission line widths and continuum luminosities and the locally calibrated virial relations for black hole masses, for which we adopt the combined normalizations of Onken et al. (2004) and Greene & Ho (2007). For most systems we simply used the black hole mass estimates from Peng et al. (2006) based on the C IV ( $\lambda 1549\text{\AA}$ ), Mg II ( $\lambda 2798\text{\AA}$ ) and H $\beta$  ( $\lambda 4861\text{\AA}$ ) mass-linewidth relations. For SDSS 1138+0314, we measured the width of the C IV ( $1549\text{\AA}$ ) line in optical spectra from the Sloan Digital Sky Survey (Adelman-McCarthy et al. 2006) and for Q 2237+030 we used the C IV line width measurement from Yee & De Robertis (1991). We estimated the black hole masses for these systems using the virial relation of Vestergaard & Peterson (2006). For SDSS 1004+4112, we measured the width of the Mg II ( $\lambda 2798\text{\AA}$ ) emission line in spectra from Inada et al. (2003) and Richards et al. (2004) and used the McLure & Jarvis (2002) Mg II virial relation to estimate its black hole mass. These mass estimates are reliable to approximately 0.3 dex (see McLure & Jarvis 2002; Kollmeier et al. 2006; Vestergaard & Peterson 2006; Peng et al. 2006).

### 5.3. RESULTS

We model the surface brightness profile of the accretion disk as a power law temperature profile,  $T \propto R^{-3/4}$ , matching the outer regions of a Shakura & Sunyaev (1973) thin disk model. We neglect the central depression of the temperature due to the inner edge of the disk and corrections from general relativity to avoid extra parameters. The effect of this simplification on our size estimates is small compared to our measurement uncertainties provided the disk size we obtain is several times larger than the radius of the inner disk edge. We will compare three disk size estimates in the context of the this simple model. First, there is our size measurement from the microlensing,  $R_S$ . This microlensing size should be viewed as a measurement of the half-light radius, but we parameterize the results in terms of the simple thin disk model in order to facilitate comparisons to the thin disk model. Converted to a half-light radius,  $R_{1/2} = 2.44R_S$ , the measurements will be nearly model-independent (see Mortonson et al. 2005). Second, there is the theoretically expected size as a function of black hole mass in the thin disk model. Third, there is the thin-disk size which would yield the observed optical flux assuming thermal radiation and a  $T \propto R^{-3/4}$  temperature profile. Collin et al. (2002) have previously noted that these theoretical and flux sizes may be discrepant.

We assume that the disk radiates as a black body, so the surface brightness at rest wavelength  $\lambda_{rest}$  is

$$f_\nu = \frac{2h_p c}{\lambda_{rest}^3} \left[ \exp \left( \frac{R}{R_{\lambda_{rest}}} \right)^{3/4} - 1 \right]^{-1} \quad (5.1)$$

where the scale length

$$\begin{aligned} R_{\lambda_{rest}} &= \left[ \frac{45G\lambda_{rest}^4 M_{BH} \dot{M}}{16\pi^6 h_p c^2} \right]^{1/3} \\ &= 9.7 \times 10^{15} \left( \frac{\lambda_{rest}}{\mu\text{m}} \right)^{4/3} \left( \frac{M_{BH}}{10^9 M_\odot} \right)^{2/3} \left( \frac{L}{\eta L_E} \right)^{1/3} \text{ cm} \end{aligned} \quad (5.2)$$

is the radius at which the disk temperature matches the wavelength,

$kT_{\lambda_{rest}} = h_p c / \lambda_{rest}$ ,  $h_p$  is the Planck constant,  $k$  is the Boltzmann constant,

$M_{BH}$  is the black hole mass,  $\dot{M}$  is the mass accretion rate,  $L/L_E$  is the luminosity in units of the Eddington luminosity, and  $\eta = L/(\dot{M}c^2)$  is the accretion efficiency.

We can also compute the size under the same model assumptions based on the magnification-corrected  $I$ -band quasar fluxes measured in HST observations as

$$R_I = 2.83 \times 10^{15} \frac{1}{\sqrt{\cos i}} \left( \frac{D_{OS}}{r_H} \right) \left( \frac{\lambda_{I,obs}}{\mu\text{m}} \right)^{3/2} 10^{-0.2(I-19)} h^{-1} \text{ cm} \quad (5.3)$$

where  $D_{OS}/r_H$  is the angular diameter distance to the quasar in units of the Hubble radius,  $I$  is the magnification-corrected magnitude and  $i$  is the disk inclination angle.

Our results are shown in Figures 5.1 through 5.3 and summarized in Table 5.1.

For the comparison with theory and the figures, we corrected the measured sizes

to  $\lambda_{rest} = 2500\text{\AA}$  assuming the  $\lambda^{4/3}$  scaling of thin disk theory and the mean inclination  $\langle \cos i \rangle = 1/2$ . We chose  $2500\text{\AA}$  because it was typical of the actual rest-frame wavelength (see Table 5.1), minimizing the sensitivity of our estimates to any uncertainty in the true wavelength scaling. Only the size of RXJ1131–1231 is strongly affected by changing the scaling of size with wavelength, becoming 20% smaller or 28% larger if we make the temperature profile significantly shallower,  $T \propto R^{-1/2}$  (e.g. Francis et al. 1991), or steeper,  $T \propto R^{-1}$ . For all other systems the effect is much smaller and introduces scaling uncertainties  $\lesssim 5\%$ .

Although we use a face-on disk model, we need to consider the role of inclination. Both the microlensing size and the flux size (Eqn. 5.3) are set by the projected area of the disk, so the true microlensing disk scale should be  $1/\sqrt{\cos i}$  of the face-on estimate. When we average over an ensemble of systems, we are averaging projected area measurements  $\langle R_{fit}^2 \rangle = \langle R_{true}^2 \cos i \rangle = (1/2 \pm 1/2\sqrt{3})R_{true}^2$ , so we correct our measurements by  $R_{true} = \sqrt{2}R_{fit}$ . In Table 5.1 and Figs. 5.1 and 5.3, we use this average correction for both the microlensing and flux sizes. The gray band in Fig. 5.1 shows the expected extra variance of  $1/2\sqrt{3}$  arising from the inclination if we view our fits as matching the predicted and observed projected areas.

There are two striking facts illustrated by the figures. First, we clearly see from Fig. 5.1 that the microlensing sizes are well correlated with the black hole mass. A power-law fit between  $R_{2500}$  and  $M_{BH}$  yields:

$$\log\left(\frac{R_{2500}}{\text{cm}}\right) = (15.70 \pm 0.16) + (0.64 \pm 0.18) \log\left(\frac{M_{BH}}{10^9 M_{\odot}}\right) \quad (5.4)$$

which is consistent with the predicted slope from thin disk theory ( $R \propto M_{BH}^{2/3}$ ) and implies a typical Eddington factor of  $\log(L/\eta L_E) = 1.54 \pm 0.36$  if we fix the slope with mass to  $2/3$  (see Fig. 5.2). Kollmeier et al. (2006) estimate that the typical quasar has  $L/L_E \approx 1/3$ , which would indicate a radiative efficiency of  $\eta = L/(\dot{M}c^2) \simeq 0.01$ . This efficiency is low compared to standard models (e.g. Gammie 1999). The goodness of fit,  $\chi^2 = 7.0$  for 9 degrees of freedom without including any effects from the spread in inclination suggests that we are slightly overestimating the size uncertainties by 13%. If we rescale the the uncertainties so that  $\chi^2/N_{DOF} = 1.0$  at the minimum, then the scale and slope uncertainties are reduced to  $\pm 0.11$  and  $\pm 0.15$ , respectively.

Second, we find that microlensing sizes are also correlated with sizes estimated from thin disk theory and from the observed flux (Figs. 5.1 and 5.3), but the three size estimates show systematic offsets in scale. Most of the offset between the microlensing disk size measurements and thin disk theory size estimates could be explained by the existing uncertainties, but the offset from the estimate based on the quasar flux is more significant (Fig. 5.1). While the microlensing and flux sizes

are well-correlated, the measured disk sizes are significantly larger than the flux sizes in all systems except QJ 0158–4325. Despite the one anomalous system, the microlensing sizes are still an average of  $0.6 \pm 0.3$  dex larger than predicted from the observed flux. Simply put, the quasars are not sufficiently luminous to have the sizes estimated from microlensing and to be radiating as black bodies with a  $T \propto R^{-3/4}$  temperature profile. Pooley et al. (2006) also noticed this problem in their more qualitative study of lensed quasars with X-ray observations.

#### 5.4. DISCUSSION

Are the discrepancies between our measurements and the size estimated from the disk flux due to a problem in the measurements, an oversimplification of the disk model or a fundamental problem in the thin disk model? We have tested our approach using Monte Carlo simulations of light curves and verified that we recover the input disk sizes. Our results are also only weakly sensitive to the assumed prior on the microlens masses (see Kochanek 2004, for a discussion). We will overestimate the source size if a significant fraction of the observed flux comes not from the continuum emission of the disk but from the larger and minimally microlensed line emitting regions (e.g. Sugai et al. 2007). This includes not only the obvious broad lines but also the broad Fe II and Balmer continuum emission that can represent  $\sim 30\%$  of the apparent continuum flux at some wavelengths (Netzer & Willis 1983;

Grandi 1982). We have experimented with adding a fraction of unmicrolensed light and found that 30% contamination does not lead to sufficiently large size changes to resolve the problem. The sizes shrink by approximately 20%. Conservatively, black hole mass estimates from the virial technique have a scatter of a factor of  $\sim 3$  (McLure & Jarvis 2002; Kollmeier et al. 2006; Vestergaard & Peterson 2006; Peng et al. 2006), which contributes only 0.3 dex of scatter to the disk size estimates. The size estimates from the flux could be affected by misestimating the magnification or failing to correct for extinction in the lens galaxy, but the uncertainties in the magnifications are only a factor of  $\sim 2$  at worst (or  $\sqrt{2}$  for the size) and none of these lenses shows significant extinction (Falco et al. 1999; Elíasdóttir et al. 2006) relative to the magnitude of the discrepancy.

The problem is also not a consequence of the obvious flaws in our simplified disk model – the neglect of the inner edge and the different temperature profile of a relativistic disk (e.g. Page & Thorne 1974). For observations at a fixed wavelength, neglecting the inner edge does not have a dramatic effect on the effective source size and the effects of relativity on the temperature profile are modest. Studies of the temperature profile in the disk with microlensing are best done by measuring the variation in source size with wavelength because size ratios can be measured much more accurately than absolute sizes. Poindexter, Morgan & Kochanek (2008) have used the wavelength dependence of the microlensing in HE 1104–1805 to derive a slope  $T \propto R^{-\beta}$  or  $R_\lambda \propto \lambda^{1/\beta}$  of  $\beta = 0.61_{-0.17}^{+0.21}$  that is consistent with thin

disk theory but would also allow a shallower temperature profile that would reduce the differences between the microlensing relativity and model atmospheres such as Hubeny & Hubeny (1997) or Li et al. (2005). Mortonson et al. (2005) have argued that microlensing essentially measures the half-light radius ( $R_{1/2} = 2.44R_\lambda$  for our model), so the first step should be to try to simultaneously match our size estimates and the observed fluxes assuming this to be the case, since the many additional parameters of the full disk models will make their direct inclusion in the microlensing calculations a major computational challenge.

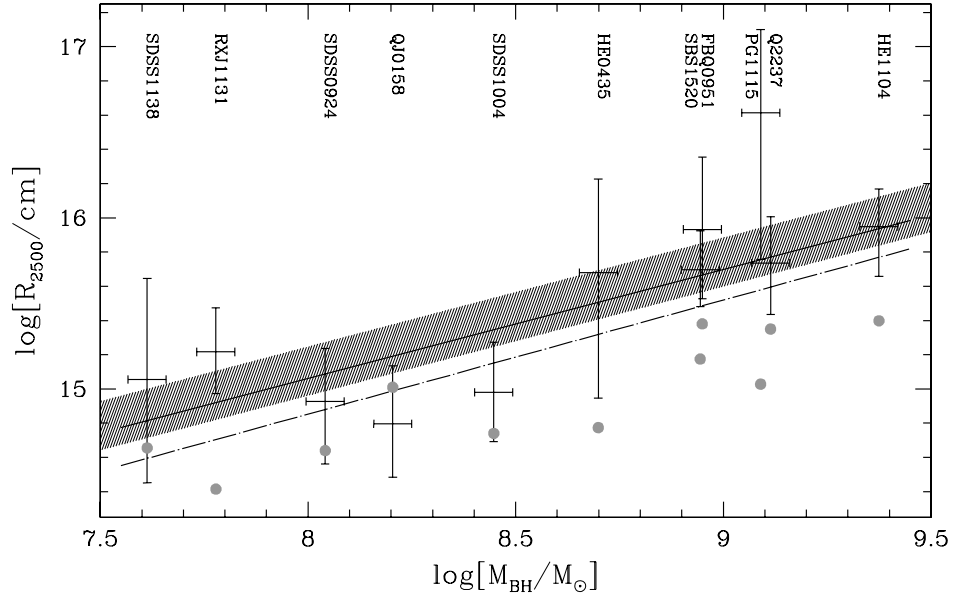


Fig. 5.1.— Inclination-corrected accretion disk size  $R_{2500}$  versus black hole mass  $M_{BH}$ . The solid line shows our best power-law fit to the data and the dot-dashed line shows the prediction from thin disk theory ( $L/L_E = 1$  and  $\eta = 0.1$ ). The shaded band surrounding the best fit shows the expected variance due to inclination. Disk sizes are corrected to a rest wavelength of  $\lambda_{rest} = 2500\text{\AA}$  and the black hole masses were estimated using emission line widths. The filled points without error bars are  $R_{2500}$  estimates based on the observed, magnification-corrected  $I$ -band fluxes. They have typical uncertainties of 0.1-0.2 dex.

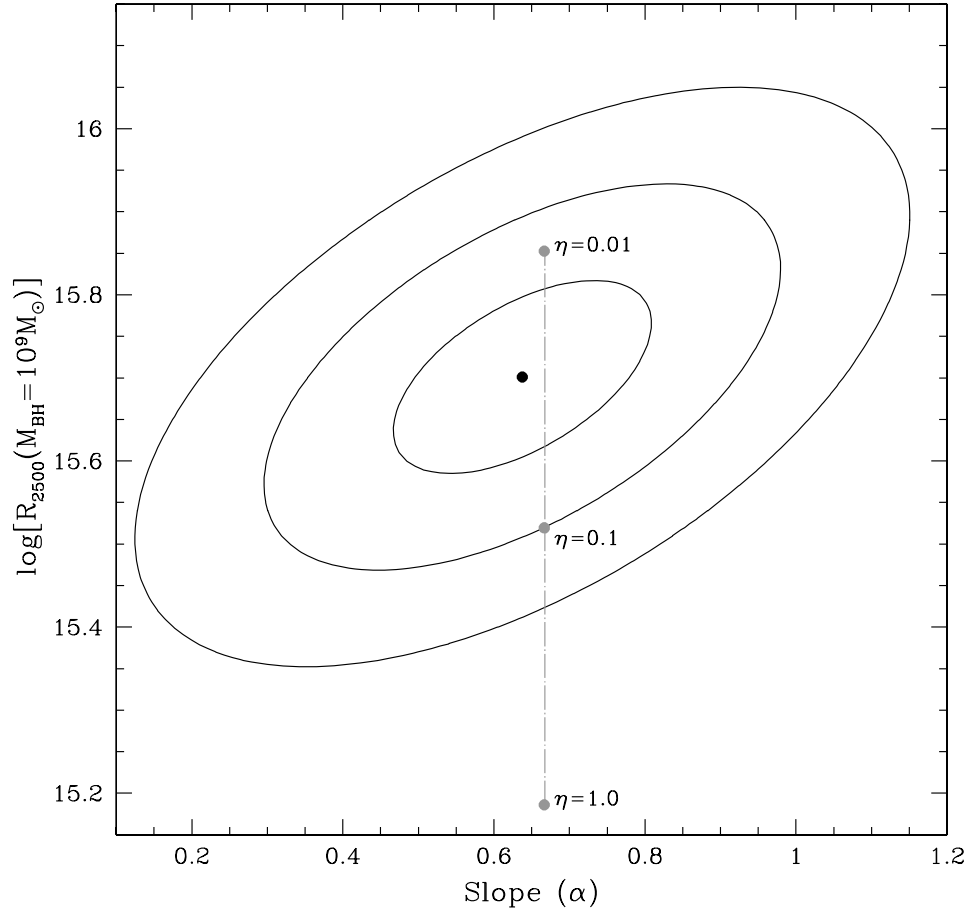


Fig. 5.2.— Results of the power-law fit to  $R_{2500}$  as a function of black hole mass. The contours show the  $1 - 3\sigma$  one-parameter confidence intervals for the slope  $\alpha$  and the normalization  $R_{2500}(M_{BH} = 10^9 M_{\odot})$  for the  $2500\text{\AA}$  accretion disk size corresponding to  $M_{BH} = 10^9 M_{\odot}$ . The best-fit value is indicated with a black point. The filled points along the dot-dashed line are theoretical thin disk sizes for quasars radiating at the Eddington limit and with efficiencies of  $\eta = L/(\dot{M}c^2) = 0.01, 0.1$  or  $1.0$ .

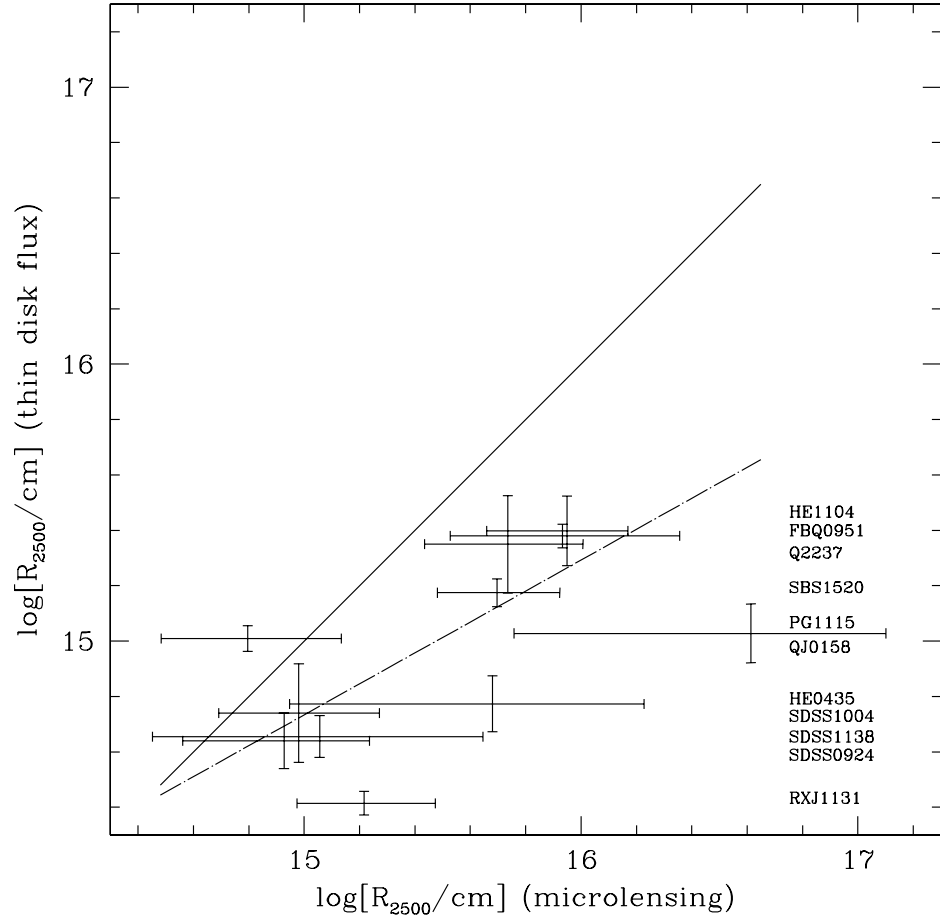


Fig. 5.3.— Thin disk flux size estimates versus accretion disk sizes from microlensing. For reference, the solid line indicates a one-to-one relationship between thin disk flux size estimates and the microlensing measurements. The dot-dashed line is the best fit to the data. Since the data points have large errors relative to their dynamic range, the best-fit slope is consistent with unity and its average offset from the solid line is 0.6 dex.

Object	Line	FWHM Å (observed)	$M_{BH}$ ( $10^9 M_{\odot}$ )	$\log(R_S/\text{cm})$ (microlensing)	$\lambda_{rest}$ ( $\mu\text{m}$ )	$I_{corr}$ (mag)	$\log(R_S/\text{cm})$ (thin disk flux)
QJ0158-4325	Mg II	40	0.16	$14.9^{+0.3}_{-0.3}$	0.306	$19.09 \pm 0.12$	$15.2 \pm 0.1$
HE0435-1223	C IV	70	0.50	$15.7^{+0.5}_{-0.7}$	0.260	$20.76 \pm 0.25$	$14.9 \pm 0.1$
SDSS0924+0219	Mg II	61	0.11	$15.0^{+0.3}_{-0.4}$	0.277	$21.24 \pm 0.25$	$14.8 \pm 0.1$
FBQ0951+2635	Mg II	70	0.89	$16.1^{+0.4}_{-0.4}$	0.313	$17.16 \pm 0.11$	$15.6 \pm 0.1$
SDSS1004+4112	Mg II	134	0.39	$14.9^{+0.3}_{-0.3}$	0.228	$20.97 \pm 0.44$	$14.9 \pm 0.2$
HE1104-1805	C IV	103	2.37	$15.9^{+0.2}_{-0.3}$	0.211	$18.17 \pm 0.31$	$15.4 \pm 0.1$
PG1115+080	Mg II	127	1.23	$16.6^{+0.5}_{-0.9}$	0.257	$19.52 \pm 0.27$	$15.1 \pm 0.1$
RXJ1131-1231	H $\beta$	90	0.06	$15.5^{+0.3}_{-0.2}$	0.422	$20.73 \pm 0.11$	$14.8 \pm 0.1$
SDSS1138+0314	C IV	25	0.04	$14.9^{+0.6}_{-0.6}$	0.203	$21.97 \pm 0.19$	$14.6 \pm 0.1$
SBS1520+530	C IV	75	0.88	$15.7^{+0.2}_{-0.2}$	0.245	$18.92 \pm 0.13$	$15.3 \pm 0.1$
Q2237+030	C IV	48	0.9 <sup>a</sup>	$15.6^{+0.3}_{-0.3}$	0.208	$18.03 \pm 0.44$	$15.5 \pm 0.2$

Note. —  $R_S$  from microlensing is the accretion disk size at  $\lambda_{rest}$ , the rest-frame wavelength corresponding to the center of the monitoring filter used for that quasar's lightcurve. Use half-light radii ( $R_{1/2} = 2.44R_S$ ) to compare these size measurements to other disk models.  $I_{corr}$  is the corrected (unmagnified)  $I$ -band magnitude. Typical  $I$ -band measurement errors are  $\lesssim 0.1$  mag, but the larger errors on  $I_{corr}$  come from uncertainties in the lens magnification.  $R_S$  calculated using corrected  $I$ -band magnitude and thin disk theory is also unscaled; it is the disk size at the rest-frame wavelength corresponding to the center of the *HST*  $I$ -band filter (F814W). Both disk sizes assume an average inclination angle  $i = 60^\circ$ .

<sup>a</sup>The C IV emission line width from Yee & De Robertis (1991) depends strongly on the fit to several blended C IV absorption features, so we report  $M_{BH}$  at lower precision.

Table 5.1. Measured and Derived Quantities

## CHAPTER 6

# X-RAY AND OPTICAL MICROLENSING IN THE LENSED QUASAR PG 1115+080

### 6.1. INTRODUCTION

When Blaes (2007) recently reviewed the state of accretion disk physics, he found that one of the most glaring problems in even the most sophisticated accretion disk models (e.g. Hubeny et al. 2000, 2001; Hirose, Krolik & Stone 2006) is their failure to support a hot corona or to produce X-rays at all. While there are models for producing the X-rays, (e.g. Haardt & Maraschi 1991, 1993; Maraschi & Tavecchio 2003; Hirose et al. 2004; Nayakshin, Cuadra & Sunyaev 2004), they do so on very different physical scales relative to the gravitational radius  $r_g = GM_{BH}/c^2$  of the black hole. For example, the magnetohydrodynamic (MHD) simulations of Hawley & Balbus (2002) predict the dragging of hot ionized gas from a jet across the surface of a cooler accretion disk resulting in bremsstrahlung. In this model, much of the emission comes from an inner torus with radius  $r \lesssim 20r_g$ , but the continuum emission region extends to very large radii ( $r \approx 200r_g$ ). On much smaller scales, the model of Hirose et al. (2004) suggests a relativistic MHD accretion disk model in the

Kerr metric whose inner torus ( $r \lesssim 10r_g$ ) supports a large current density capable of emitting a moderate X-ray flux. The disk-corona model of Haardt & Maraschi (1991, see also Merloni 2003) produces X-rays via inverse Compton scattering in a corona which extends over much of the optical/UV accretion disk, while the “lamp-post” (Martocchia et al. 2002) and “aborted jet” (Ghisellini et al. 2004) models predict a significantly smaller emission structure ( $r \lesssim 3.0r_g$ ).

Given their small angular size, few traditional observational constraints can be placed on the size of quasar X-ray continuum emission regions apart from simple and often inconclusive variability timescale arguments (e.g. Vaughan, Fabian & Nandra 2003). Fabian et al. (1995) demonstrated that the broad Fe K $\alpha$  X-ray emission line in Seyfert 1 spectra is probably emitted from the region immediately surrounding the black hole. The width and variability of Fe K $\alpha$  emission has now been measured in a number of systems to study the innermost regions of those accretion disks (e.g. Iwasawa et al. 1999; Lee et al. 1999; Fabian et al. 2002; Iwasawa et al. 2004). Motivated by this work, Young & Reynolds (2000); Ballantyne et al. (2005) and others have proposed the use of *Constellation-X* to measure the size of the Fe K $\alpha$  X-ray reflection region by reverberation mapping. Fortunately, gravitationally lensed quasars can be studied on these scales at all wavelengths because the quasar is microlensed by the stars in the lens galaxy. The Einstein radius  $R_E$  of the stars is comparable to the expected near-IR sizes of accretion disks, so most disk emission will be significantly microlensed with the amplitude of the variability increasing

rapidly for source components that are small compared to  $R_E$  due to the presence of caustic curves on which the microlensing magnification diverges (see the review by Wambsganss 2006).

More generally, microlensing variability is a function of the relative tangential velocity  $v_e$  between source, lens and observer, the macroscopic lensing properties of the lens galaxy (the convergence  $\kappa$ , the stellar surface density fraction  $\kappa_*/\kappa$  and the shear  $\gamma$ ) and the relative sizes of the source and the source plane projection of the Einstein radius  $R_E$  of an average mass star  $\langle M \rangle$  in the lens galaxy. Since the size of the X-ray emitting region is expected to be much smaller than the optical accretion disk, we expect that the effects of microlensing will be more pronounced at X-ray wavelengths than in the optical (e.g. Jovanović et al. 2008). This effect has now been observed in many lensed quasars (e.g. Morgan et al. 2001; Chartas et al. 2002; Dai et al. 2003; Blackburne et al. 2006; Chartas et al. 2007; Pooley et al. 2007) and was documented specifically in PG 1115+080 by Pooley et al. (2006).

The quadruply-lensed quasar PG 1115+080 was discovered over 25 years ago (Weymann et al. 1980). Since then, it has been the subject of a large number of investigations at multiple wavelengths. In particular, the closely separated A1 and A2 images bracket a critical line so we expect their flux ratio to be approximately unity, but Impey et al. (1998) and others have measured an anomalously low flux ratio in the optical and NIR (e.g.  $A_2/A_1 = 0.64 \pm 0.02$  in the  $H$ -band). Chiba et al. (2005) showed that the  $A_2/A_1$  flux ratio returns to nearly unity in the mid-IR

( $A_2/A_1 = 0.93 \pm 0.06$  at  $11.7\mu\text{m}$ ), demonstrating that stellar microlensing is the likely cause of the anomaly rather than millilensing (e.g. Kochanek & Dalal 2004).

Recently, Pooley et al. (2006) conducted a study of the system's anomalous X-ray flux ratios as measured in two *Chandra X-Ray Observatory* (*Chandra*) observations. Pooley et al. (2006) demonstrated that microlensing is the likely cause of the X-ray flux ratio anomaly in PG 1115+080 and qualitatively argued that its X-ray continuum emission region must be significantly smaller than its optical accretion disk. In this paper, we combine these 2 epochs of X-ray data from *Chandra* with our optical monitoring data to make simultaneous measurements of the system's optical and X-ray continuum emission regions using the Monte Carlo microlensing analysis technique of Kochanek (2004).

In § 6.2, we describe our optical monitoring data and the X-ray flux measurements. In § 6.3, we review our microlensing analysis technique and describe its application to PG 1115+080. In § 6.4 we present the results of our calculations and discuss their implications for the sizes of the quasar emission regions and the stellar content of the lens galaxy. We assume a flat cosmology with  $\Omega_0 = 0.3$ ,  $\Lambda_0 = 0.7$  and  $H_0 = 70 \text{ km s}^{-1} \text{ Mpc}^{-1}$ .

## 6.2. *Hubble Space Telescope* OBSERVATIONS, *Chandra* AND OPTICAL MONITORING DATA

We observed PG 1115+080 in the *V*- (F555W), *I*- (F814W) and *H*- (F160W) bands using the *Hubble Space Telescope* (*HST*) for the CfA-Arizona Space Telescope Survey (CASTLES<sup>1</sup>, Falco et al. 2001). The *V*- and *I*-band images were taken using the Wide-Field Planetary Camera 2 (WFPC2). The *H*-band images, originally reported in Yoo et al. (2006), were taken using the Near-Infrared Camera and Multi-Object Spectrograph (NICMOS). We made photometric and astrometric fits to the *HST* imagery with *imfitfits* (Lehár et al. 2000), using a de Vaucouleurs model for the lens galaxy, an exponential disk model for the quasar host galaxy and point sources for the quasar images. The astrometric fits are consistent with those of Impey et al. (1998). Our *HST* astrometry and photometry are presented in Table 6.1.

We monitored PG 1115+080 in the *R*-band over multiple seasons with the SMARTS 1.3m telescope using the ANDICAM optical/infrared camera (DePoy et al. 2003)<sup>2</sup>, the Wisconsin-Yale-Indiana (WIYN) observatory using the WIYN Tip-Tilt Module (WTTM)<sup>3</sup>, the 2.4m telescope at the MDM Observatory using the MDM

---

<sup>1</sup><http://cfa.harvard.edu/castles/>

<sup>2</sup><http://www.astronomy.ohio-state.edu/ANDICAM/>

<sup>3</sup>[http://www.wiyn.org/wttm/WTTM\\_manual.html](http://www.wiyn.org/wttm/WTTM_manual.html)

Eight-K<sup>4</sup>, Echelle and RETROCAM<sup>5</sup> (Morgan et al. 2005) imagers and the 6.5m Magellan Baade telescope using IMACS (Bigelow et al. 1999). A detailed discussion of our lensed quasar monitoring data reduction pipeline can be found in Kochanek et al. (2006), but we briefly summarize our technique here. We hold the lens astrometry fixed to the *HST* *H*-band measurements. We treat each quasar image as a point source and model the point-spread function with three nested, elliptical Gaussian profiles. We measure the flux of each image by comparison to the flux of 5 reference stars in the field. We assume that the lens galaxy flux remains constant and fix its value to the flux found by minimizing the residuals in a fit to the complete set of measurements from each instrument. We supplemented our optical lightcurves with *V*-band data published by Schechter et al. (1997). We applied magnitude offsets to the Schechter et al. (1997) data and data from the other observatories to match the *R*-band measurements from SMARTS. The wavelength differences between monitoring bands are small enough to have little effect on the results given the expected  $\lambda^{4/3}$  scaling of the optical accretion disk size (Shakura & Sunyaev 1973) and our measurement uncertainties.

PG 1115+080 is a particularly challenging system to monitor because the A1 and A2 images are separated by a mere  $0''.48$ . The seeing in our ground-based observations was rarely better than  $1''.0$ , so we were forced to sum the flux from images A1 and A2. We refer to this summed lightcurve as  $A12 = A1 + A2$ . As

---

<sup>4</sup><http://www.astro.columbia.edu/~arlin/MDM8K/>

<sup>5</sup><http://www.astronomy.ohio-state.edu/MDM/RETROCAM>

documented by Pooley et al. (2006), the strongest effect of optical microlensing appears in the A1/A2 flux ratio, so we supplemented our lightcurves with 5 epochs of data from the literature in which the A1 and A2 images are clearly resolved (Schechter et al. 1997; Courbin et al. 1997; Impey et al. 1998; Pooley et al. 2006). We present our optical monitoring data in Table 6.3.

We complement our optical lightcurves with X-ray fluxes from the two epochs of 0.5 – 8 keV *Chandra* imagery published by Pooley et al. (2006), although here we used the refined flux measurements presented in Pooley et al. (2007). The details of the X-ray data reduction and flux ratio calculations are found in those papers.

### 6.3. MICROLENSING MODELS

Microlensing statistics are strongly influenced by the presence of smoothly distributed dark matter (Schechter & Wambsganss 2002), typically parameterized as the ratio of the stellar surface density to the total surface density  $\kappa_*/\kappa$ . We considered a range of possible stellar mass fractions in our calculations. We used the *GRAVLENS* software package (Keeton 2001) to generate a series of ten models that match the *HST* astrometry and reproduce the mid-infrared (11.7  $\mu\text{m}$ ) flux ratios from Chiba et al. (2005). Each model consists of concentric de Vaucouleurs and NFW (Navarro, Frenk & White 1996) profiles, and we vary the mass in the de Vaucouleurs component over the range  $0.1 \leq f_{M/L} \leq 1.0$  in steps of  $\Delta f_{M/L} = 0.1$ ,

where  $f_{M/L} = 1.0$  represents a constant mass-to-light ratio (de Vaucouleurs) model with no dark matter halo. Table 6.2 summarizes the microlensing parameters as a function of  $f_{M/L}$ . Treu & Koopmans (2002) found that the best fit to the system’s large stellar velocity dispersion ( $\sigma_* = 281 \pm 25 \text{ km s}^{-1}$ , Tonry 1998) is provided by a steep mass profile  $\rho \propto r^{-2.35}$ , implying a large stellar mass component, and for  $H_0 = 72 \text{ km s}^{-1} \text{ Mpc}^{-1}$ , the best fit to the (Schechter et al. 1997) time delays is provided by the  $f_{M/L} = 0.8$  model.

We generated a set of microlensing magnification patterns at each image location for each of the 10 macroscopic mass models using a variant of the ray-shooting method (Schneider et al. 1992, see Kochanek 2004 for the details of our technique). The patterns are  $8192 \times 8192$  images of the source-plane projection of the magnification patterns from an ensemble of typical lens galaxy stars at each image location. We approximated the Galactic stellar mass function of Gould (2000) as a power law, assuming  $dN(M)/dM \propto M^{-1.3}$  with a dynamic range in mass of a factor of 50. The mean stellar mass in the lens galaxy  $\langle M \rangle$  is initially unknown, so magnification patterns are produced in units of the Einstein radius with an outer scale of  $20 R_E$ . For PG 1115+080, the Einstein radius is  $R_E = 6.6 \times 10^{16} \langle M/M_\odot \rangle^{1/2} \text{ cm}$ . To convert to physical units, all results are eventually scaled by some factor of  $\langle M/M_\odot \rangle$ . Henceforth, quantities in Einstein units will be given the “hat” accent to distinguish them from quantities in physical units. So the physical source size  $r_s$  is

related to the scaled source size  $\hat{r}_s$  by  $r_s = \hat{r}_s \langle M/M_\odot \rangle^{1/2}$ , and the physical effective velocity  $v_e$  is related to the scaled velocity  $\hat{v}_e$  by  $v_e = \hat{v}_e \langle M/M_\odot \rangle^{1/2}$ .

In order to eliminate the quasar's intrinsic variability, we shifted the optical light curves by the measured time delays (Schechter et al. 1997), so that any remaining variability in the flux ratios must be attributed to microlensing. It is impossible to offset the sparse X-ray flux measurements by the time delays, so we assume that X-ray flux ratios can be treated as simultaneous in a statistical sense. The time delay between the A1 and A2 images is less than one day, so there was no need to apply a time delay correction to the 5 epochs of individually resolved A1 and A2 data.

As described in detail by Kochanek (2004) (see also Morgan et al. 2007; Poindexter, Morgan & Kochanek 2008), our Monte Carlo microlensing analysis searches for trajectories across the magnification pattern that fit the observed light curves. We used a thin accretion disk surface brightness profile for the source model (Shakura & Sunyaev 1973) with

$$I(R) \propto \left\{ \exp \left[ (R/r_s)^{3/4} \right] - 1 \right\}^{-1}, \quad (6.1)$$

where the scale radius  $r_s$  is the radius at which the disk temperature matches the rest-frame wavelength of our monitoring band,  $kT = hc(1 + z_s)/\lambda_{obs}$ . We neglect the central hole in the emission profile, the effect of which is negligible at optical

wavelengths. Microlensing primarily depends on the projected area of the source while the true scale lengths also depend on the shape of the source and its inclination. We will refer to a radius where we have ignored the shape and inclination of the source as an “effective” radius that defines a projected area  $\pi r_{eff}^2$ . For a thin disk, the effective radius is related to the source scale length by  $r_{eff}^2 = r_s^2 \cos i$  where  $i$  is the inclination angle. The X-ray emission presumably has a different emission profile and shape. Fortunately, Mortonson et al. (2005) demonstrated that the half-light radius measured with microlensing is essentially independent of the surface brightness profile, so we will characterize the X-ray emission by the effective half-light radius. For our thin disk model, the half-light radius is related to the disk scale length by  $R_{1/2} = 2.44r_s$ . In summary, to compare the sizes of the optical and X-ray emitting regions we will use the ratio of the effective radii  $r_{opt}/r_X$ , to characterize the optical emission we will use the thin disk scale length  $r_{s,opt}$  and an inclination angle  $\cos i$ , and for the X-ray emission we will use the effective (i.e. no shape corrections) half-light radius  $r_{1/2,X}$ .

We generated 8 trial magnification patterns for each of the 10 macroscopic mass models. For each trial and model we produced 50,000 trial light curves for a  $16 \times 21$  grid of X-ray and optical source sizes. These source sizes  $\hat{r}_s$  are scaled sizes that depend on the microlens mass  $r_s = \hat{r}_s \langle M/M_\odot \rangle^{1/2}$ . We used logarithmic grids spanning the region producing acceptable fits with a grid spacing of 0.2 dex. In total there were  $4 \times 10^6$  trial light curves for each combination of X-ray and

optical source sizes. When assessing the quality of our fits to the observed flux ratios, we allowed for only 0.1 mag of systematic uncertainty in the flux ratios of the macro models because the mid-IR flux ratios of Chiba et al. (2005) are a close approximation to the intrinsic flux ratios in this system. In selecting trial light curves we gave equal statistical weight to the optical data where A1 and A2 could not be separately measured, optical data where A1 and A2 could be separately measured, and the X-ray data so that we would isolate trials with reasonable fits to all three classes of data. The final goodness of fit was evaluated with a  $\chi^2$  fit to the light curves where all data have their true statistical weights and we discard all fits with  $\chi^2/N_{dof} > 4.0$  as they make no significant contribution to the final Bayesian integrals (see Kochanek 2004). Figures 6.1 and 6.2 show two examples of good fits to the data. The stronger flux anomalies in the X-ray data force the X-ray source to be more compact than the optical, leading to the much larger variability predicted for the X-ray bands relative to the optical.

To convert the results to physical units, we must either assume a prior on the mean mass of the microlenses  $\langle M \rangle$  or a probability distribution for the transverse velocity between source, lens and observer  $v_e$  since the scaled and actual velocities are related by  $v_e = \hat{v}_e \langle M/M_\odot \rangle^{1/2}$ . For a mean stellar mass prior, we assume  $0.1 M_\odot \leq \langle M \rangle \leq 1.0 M_\odot$ . We model the effective velocity of the system with three components. We set the velocity of the observer  $v_o = 94 \text{ km s}^{-1}$  to be the projection of the CMB dipole velocity (Kogut et al. 1993) onto the lens plane. We calculate

a one-dimensional stellar velocity dispersion in the lens galaxy of  $\sigma_* = 220 \text{ km s}^{-1}$  based on the Einstein radius of its macroscopic mass model and we assume a lens galaxy peculiar velocity dispersion of  $\sigma_p = 235/(1 + z_l) \text{ km s}^{-1} = 179 \text{ km s}^{-1}$  (Kochanek 2004). In general these two methods give similar physical size estimates because the sizes depend only weakly on the mass scale  $\langle M \rangle$ . Microlensing depends only on the size and velocity of the source in Einstein units,  $\hat{r}_s = r_s/\langle M/M_\odot \rangle^{1/2}$  and  $\hat{v}_e = v_e/\langle M/M_\odot \rangle^{1/2}$ . A given level of variability can be produced either by moving a small source slowly (both  $\hat{r}_s$  and  $\hat{v}_e$  small) or a large source rapidly (both  $\hat{r}_s$  and  $\hat{v}_e$  large) with (roughly)  $\hat{r}_s \propto \hat{v}_e$ . But the mass scale implied by a given Einstein velocity scales as  $\langle M/M_\odot \rangle = (v_e/\hat{v}_e)^2$  so the dependence of the physical scale on the mass essentially cancels given some knowledge of the physical velocity  $v_e$ , with  $r_s = \hat{r}_s \langle M/M_\odot \rangle^{1/2} \propto \langle M \rangle^0$  (see Kochanek 2004). The poor temporal overlap of the optical and X-ray light curves means that the differences between the priors are larger than we have found for most other lenses (e.g. Morgan et al. 2007; Poindexter, Morgan & Kochanek 2008).

## 6.4. RESULTS AND DISCUSSION

Figure 6.3 shows the ratio of the effective radii of the optical and X-ray sources where the effective radius should be viewed as the square root of the projected source area. The results depend little on whether we use the mass or the velocity

prior, so we present quantitative results only for the mass prior. The advantage of the size ratio is that it has no direct dependence on the mass of the microlenses (in the sense that  $\hat{r}_{opt}/\hat{r}_X = r_{opt}/r_X$ ). We find that  $\log[r_{opt}/r_X] = 1.3_{-0.5}^{+1.1}$ . Figure 6.4 shows the estimates for the physical sizes, where we show the inclination corrected disk scale length for the optical source and the effective half-light radius for the X-ray source. Recall from § 6.3 that the disk scale length is the point where the temperature equals the photon energy  $kT = hc/\lambda_{rest}$  and that the effective half-light radius has no shape or inclination corrections. Thus, at  $0.3\mu\text{m}$  or  $T = 4.8 \times 10^4$  K, the disk scale length is  $\log[(r_{s,opt}/\text{cm})\sqrt{\cos(i)/0.5}] = 16.1_{-0.8}^{+0.6}$ , and in the (rest-frame) 1.4-21.8 keV band the effective X-ray half light radius is  $\log(r_{1/2,X}/\text{cm}) = 15.6_{-0.9}^{+0.6}$ .

We can compare these size estimates to theoretical expectations given the estimated black hole mass of  $1.23 \times 10^9 M_\odot$  from Peng et al. (2006) based on the quasar luminosity and the width of the Mg II ( $\lambda 2798\text{\AA}$ ) emission line, where black hole mass estimates using this technique have a typical uncertainties of  $\sim 0.3$  dex (see McLure & Jarvis 2002; Peng et al. 2006). Fig. 6.4 shows the gravitational radius  $r_g = 1.9 \times 10^{14}$  cm for this mass, which is the innermost stable circular orbit for a maximally rotating Kerr black hole. For reference, we also plot the innermost stable circular orbit for a Schwarzschild black hole at  $6r_g$ . The optical emission comes from well outside the inner edge of the disk ( $\sim 86r_g$ ), justifying our neglect of the inner edge of the disk in Eqn. 6.1. Thin disk theory (Shakura & Sunyaev 1973) predicts that the optical size for a face-on quasar radiating with

10% efficiency at the Eddington limit should be  $\log[r_{s,opt}/\text{cm}] = 15.6$ , and our black hole mass/accretion disk size scaling from Morgan et al. (2007) predicts a scale radius of  $\log[(r_{s,opt}/\text{cm})\sqrt{\cos(i)/0.5}] = 15.8 \pm 0.3$ . Thus, our current result is consistent with the Morgan et al. (2007) black hole mass/accretion disk size scaling and is slightly larger than the theoretical thin disk size (see Morgan et al. 2007, for a detailed comparison of microlensing disk size estimates in 11 systems). The far more compact X-ray emission comes from a region very close to the inner disk edge, with a half-light radius of  $\sim 10r_g$ . This result seems to favor models with a smaller emission structure (e.g. Martocchia et al. 2002; Ghisellini et al. 2004; Hirose et al. 2004) and disfavor the standard disk-corona model (Haardt & Maraschi 1991; Merloni 2003) and others with an extended X-ray continuum emission region (e.g. Hawley & Balbus 2002).

We also obtain some information on the structure of the lens galaxy, as illustrated in Figure 6.5 where we show our estimates of the stellar fraction  $f_{M/L}$ . We do not find a strong peak in the  $f_{M/L}$  distribution, but we do detect a weak trend favoring models with lower  $f_{M/L}$  and a low stellar surface density (Fig. 6.5), as we would expect. Both the Schechter et al. (1997) time delays (see Kochanek 2002) and the Tonry (1998) velocity dispersion (see Treu & Koopmans 2002) require mass models with little dark matter near the radius of the lensed images (although see Romanowsky & Kochanek 1999 for examples of dynamical models consistent with both a significant dark matter halo and the high velocity dispersion). While

Figure 6.5 is not conclusive, it is probable that with better X-ray light curves we will be able to measure  $f_{M/L}$  and either confirm or reject the time delay and velocity dispersion measurements.

We are expanding our analyses to include all 10 lensed quasars with archival X-ray data (see Pooley et al. 2007) as well as three systems (HE 1104–1805, RX J1131–1231 and Q 2237+0305) where we have obtained X-ray light curves. For many of these systems (RX J1131–1231, Q 2237+0305, WFI J2033–4723, SDSS 0924+0219 and H 1413+117) we have optical light curves comparable to those used here (see Morgan et al. 2006; Dai et al. 2008), but for the remainder we will have to rely on sparse, archival optical data. The main challenge we face is that the computational intensity of modeling the two bands simultaneously is a significant bottleneck for completing the analyses. Nonetheless, we see no fundamental barriers to complementing our correlations between optical disk size and black hole mass (Morgan et al. 2007) with their X-ray equivalents. The pattern suggested by PG 1115+080 is that the X-ray continuum emission region tracks the inner edge of the accretion disk. We hope to determine if this model is universal.

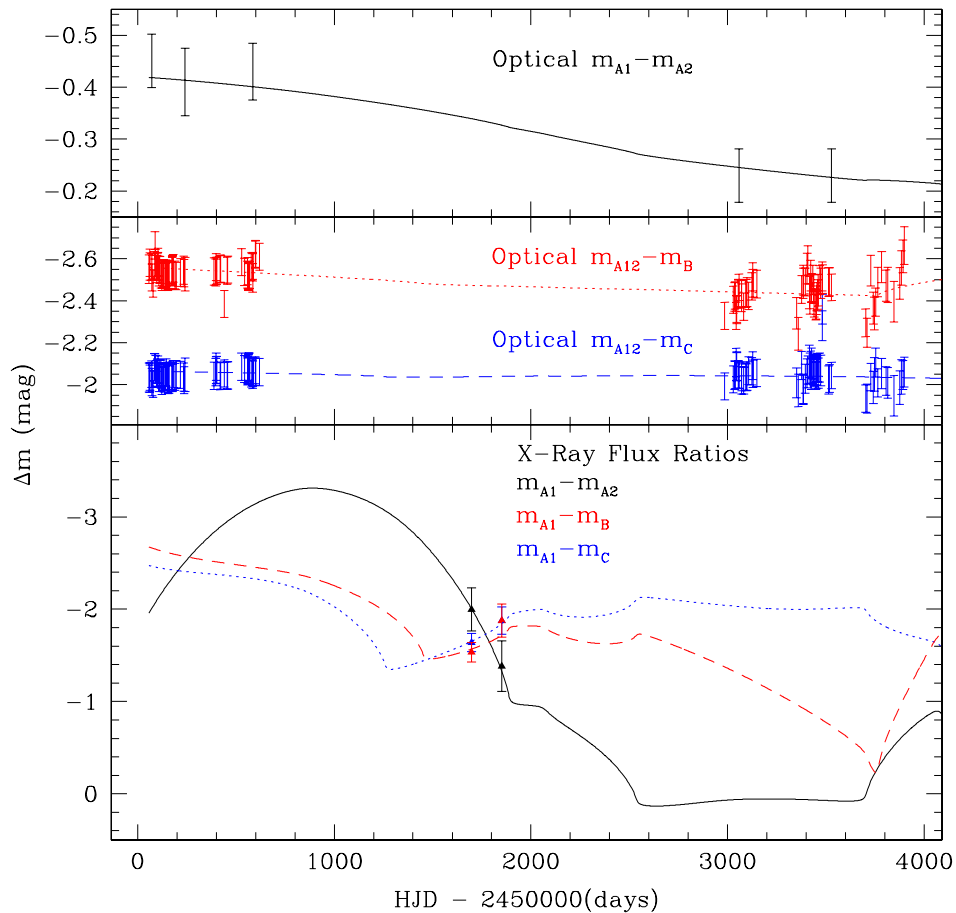


Fig. 6.1.— Examples of good fits to the observed flux ratios. Top panel: We fit the 5 epochs of data with a resolved A1/A2 flux ratio individually. The error bars are the data, and the black curve is the fit. Middle panel: Dotted red and dashed blue curves are best fits to the A12/B and A12/C flux ratios, respectively. Data are plotted with error bars in the same color scheme. The A12/B and A12/C flux ratios varied little over the last decade. Bottom panel: The best fits to the observed A1/A2, A1/B, and A1/C X-ray flux ratios are plotted using solid black, dotted red and dashed blue curves, respectively. Data are plotted using triangular points in the same color scheme.

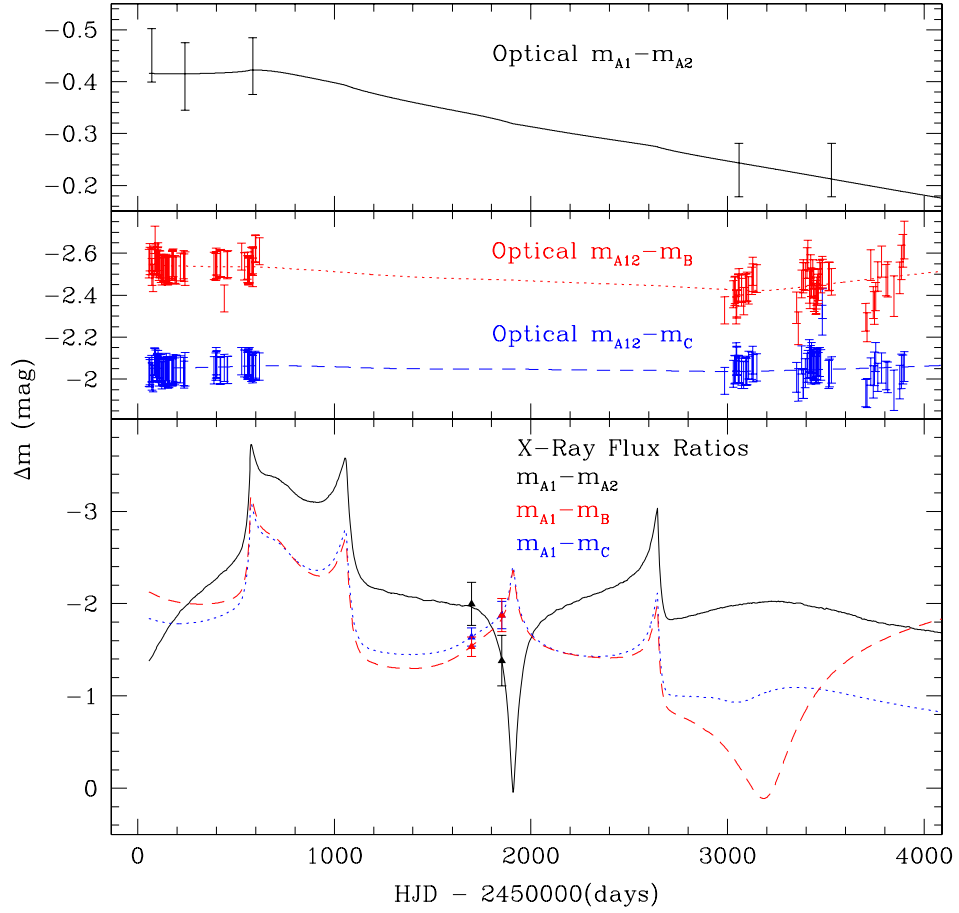


Fig. 6.2.— A second solution plotted as in Fig. 6.1. The short timescale of the X-ray variability in this solution means that it has a higher effective velocity  $\hat{v}_e$  than the solution in Fig. 6.1.

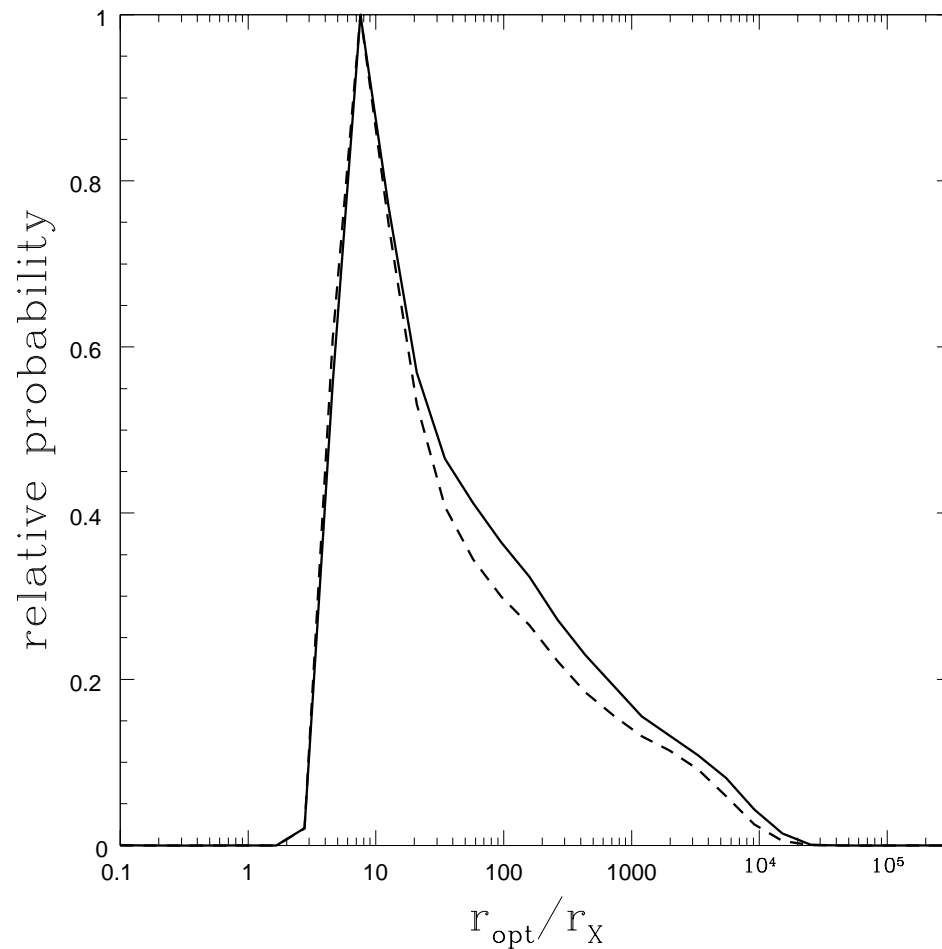


Fig. 6.3.— Probability distribution for the ratio of effective radii of the optical and X-ray sources. The solid curve uses the velocity prior. The dashed curve uses the prior on the microlens masses  $0.1 M_{\odot} < \langle M \rangle < 1.0 M_{\odot}$ .

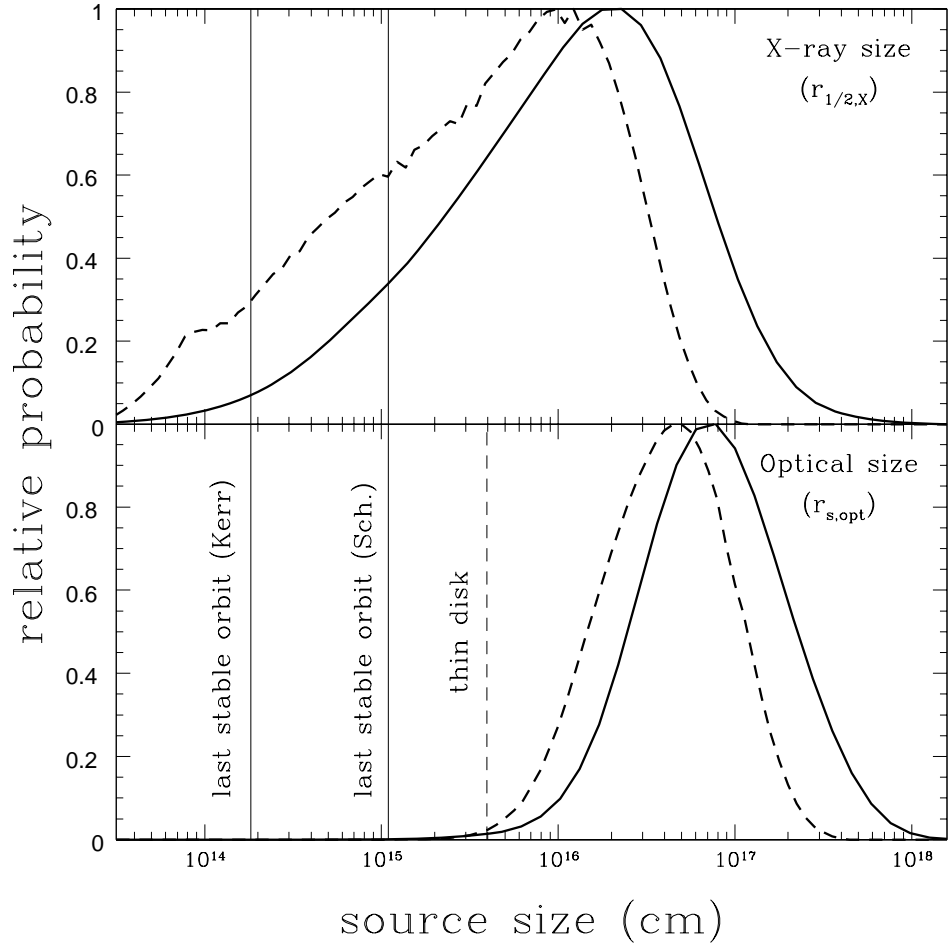


Fig. 6.4.— Probability distributions for the effective X-ray half light radius  $r_{1/2,X}$  (top) and optical thin disk scale radius  $r_{s,opt}$  (bottom). For the thin disk, we assumed an inclination of  $\cos i = 1/2$ . The solid curves use only the velocity prior while the dashed curves add the prior on the microlens masses of  $0.1 M_{\odot} < \langle M \rangle < 1.0 M_{\odot}$ . Given the black hole mass estimate of  $1.23 \times 10^9 M_{\odot}$  for PG 1115+080 from Peng et al. (2006), the solid vertical lines indicate the innermost stable circular orbit  $r_g = GM_{BH}/c^2$  for a maximally rotating Kerr black hole and the innermost stable circular orbit for a Schwarzschild black hole at  $6r_g$ . The dashed vertical line is the prediction of thin disk theory for the scale radius at  $0.26 \mu\text{m}$  for an Eddington-limited accretion disk radiating at 10% efficiency.

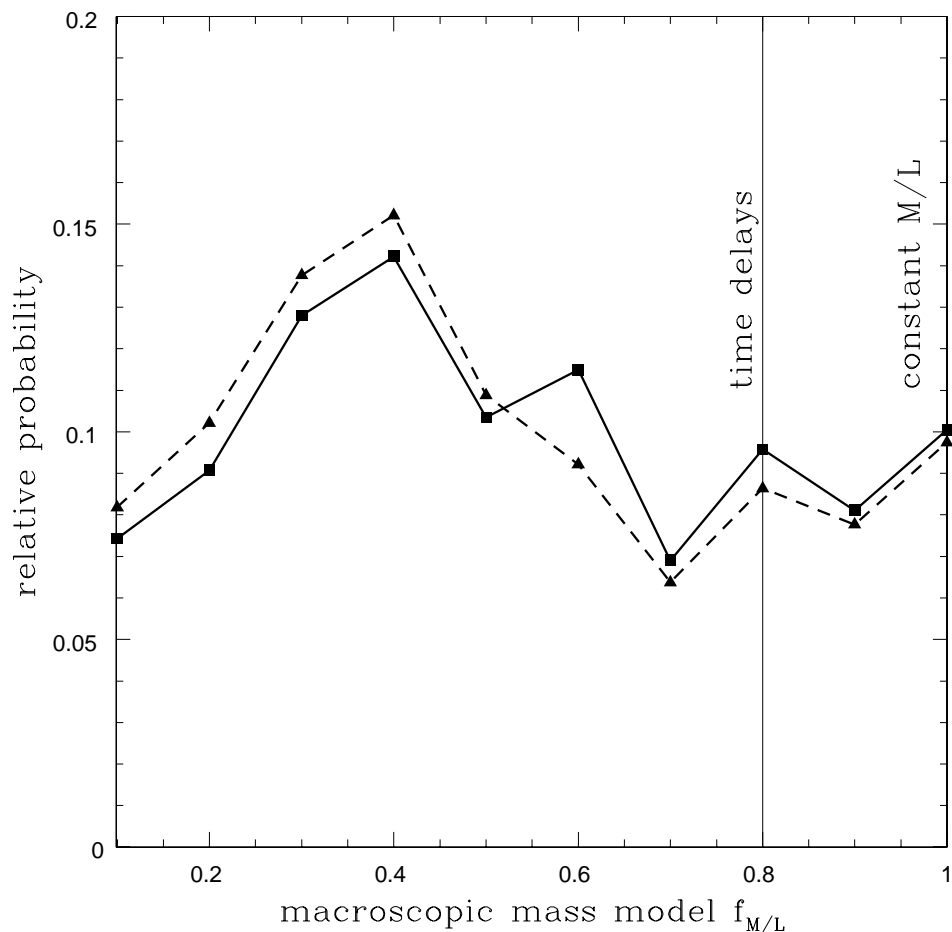


Fig. 6.5.— Probability distribution for  $f_{M/L}$ , the fraction of the lens galaxy mass in the constant M/L ratio (de Vaucouleurs) component.  $f_{M/L}$  can be related to the stellar surface density fraction  $\kappa_*/\kappa$  at each image location using the data in Table 6.2. The  $f_{M/L}$  value implied by the time delays is plotted with a solid vertical line.

Component	Astrometry		$\Delta\text{Dec}$	H=F160W	Photometry	
	$\Delta\text{RA}$				I=F814W	V=F555W
A1	$1''.328 \pm 0''.003$	$-2''.034 \pm 0''.003$		$15.71 \pm 0.02$	$16.42 \pm 0.02$	$16.90 \pm 0.11$
A2	$1''.477 \pm 0''.004$	$-1''.576 \pm 0''.003$		$16.21 \pm 0.02$	$16.85 \pm 0.01$	$17.62 \pm 0.09$
B	$-0''.341 \pm 0''.003$	$-1''.961 \pm 0''.003$		$17.70 \pm 0.02$	$18.37 \pm 0.01$	$18.95 \pm 0.12$
C	$\equiv 0$	$\equiv 0$		$17.23 \pm 0.03$	$17.91 \pm 0.02$	$18.39 \pm 0.06$
G	$0''.381 \pm 0''.003$	$-1''.344 \pm 0''.003$		$16.66 \pm 0.04$	$18.92 \pm 0.02$	$20.74 \pm 0.03$

Table 6.1. HST Astrometry and Photometry of PG1115+080

$f_{M/L}$	Convergence $\kappa$			Shear $\gamma$			$\kappa_*/\kappa$					
	A1	A2	C	A1	A2	C	A1	A2	C			
0.1	0.75	0.76	0.84	0.69	0.22	0.27	0.32	0.18	0.021	0.023	0.031	0.016
0.2	0.69	0.71	0.79	0.64	0.27	0.33	0.41	0.20	0.046	0.050	0.066	0.034
0.3	0.64	0.66	0.74	0.59	0.31	0.39	0.49	0.23	0.075	0.081	0.105	0.055
0.4	0.59	0.61	0.69	0.54	0.36	0.44	0.58	0.25	0.11	0.12	0.15	0.08
0.5	0.54	0.56	0.63	0.49	0.40	0.50	0.66	0.28	0.15	0.16	0.20	0.11
0.6	0.49	0.51	0.59	0.44	0.44	0.56	0.74	0.30	0.20	0.21	0.25	0.14
0.7	0.45	0.46	0.54	0.39	0.48	0.61	0.81	0.32	0.25	0.27	0.31	0.18
0.8	0.40	0.41	0.49	0.34	0.52	0.66	0.89	0.35	0.32	0.34	0.39	0.24
0.9	0.36	0.38	0.44	0.30	0.55	0.71	0.96	0.36	0.40	0.42	0.46	0.29
1.0	0.31	0.33	0.40	0.26	0.60	0.76	1.03	0.39	0.51	0.54	0.57	0.39

Note. — Convergence  $\kappa$ , shear  $\gamma$  and the fraction of the total surface density composed of stars  $\kappa_*/\kappa$  at each image location for the series of macroscopic mass models where  $f_{M/L} = 1.0$  corresponds to a constant mass-to-light ratio model for the lens galaxy.

Table 6.2. PG1115+080 Lens Galaxy Mass Models

HJD	$\chi^2/N_{dof}$	Images A1+A2	Image B	Image C	$\langle \text{Stars} \rangle$	Source
2994.927	1.00	-1.095 ± 0.006	1.192 ± 0.010	0.896 ± 0.008	0.019 ± 0.004	MDM
3038.714	1.23	-1.071 ± 0.008	1.319 ± 0.012	0.971 ± 0.010	-0.014 ± 0.005	SMARTS
3045.790	1.18	-1.078 ± 0.014	1.323 ± 0.018	1.064 ± 0.024	-0.046 ± 0.005	SMARTS
3047.003	1.69	-1.078 ± 0.004	1.336 ± 0.007	0.938 ± 0.007	0.148 ± 0.004	WIYN
3055.690	1.46	-1.077 ± 0.009	1.321 ± 0.012	0.973 ± 0.010	-0.003 ± 0.004	SMARTS
3055.753	1.09	-1.080 ± 0.004	1.314 ± 0.008	0.950 ± 0.007	0.068 ± 0.004	MAGELLAN
3063.677	1.47	-1.082 ± 0.008	1.362 ± 0.011	0.968 ± 0.009	0.004 ± 0.004	SMARTS
3064.824	1.55	-1.077 ± 0.005	1.235 ± 0.008	0.900 ± 0.007	0.066 ± 0.004	MDM
3080.640	1.90	-1.083 ± 0.008	1.374 ± 0.011	0.993 ± 0.009	0.005 ± 0.004	SMARTS
3091.573	1.14	-1.078 ± 0.009	1.309 ± 0.012	0.938 ± 0.010	-0.006 ± 0.004	SMARTS
3101.647	1.11	-1.102 ± 0.011	1.377 ± 0.017	0.918 ± 0.012	-0.041 ± 0.005	SMARTS
3104.646	2.85	-1.105 ± 0.004	1.297 ± 0.007	0.917 ± 0.007	0.172 ± 0.004	WIYN
3108.540	3.46	-1.119 ± 0.008	1.289 ± 0.012	0.964 ± 0.010	0.000 ± 0.004	SMARTS
3116.582	1.02	-1.119 ± 0.009	1.337 ± 0.013	0.953 ± 0.010	-0.002 ± 0.004	SMARTS
3132.534	1.07	-1.107 ± 0.009	1.300 ± 0.012	0.961 ± 0.010	-0.021 ± 0.005	SMARTS
3136.717	5.84	-1.132 ± 0.005	1.255 ± 0.008	0.893 ± 0.007	0.062 ± 0.004	MDM
3138.476	1.34	-1.093 ± 0.009	1.322 ± 0.013	1.004 ± 0.011	-0.016 ± 0.005	SMARTS
3359.787	2.12	-0.929 ± 0.011	1.350 ± 0.014	1.085 ± 0.011	-0.006 ± 0.004	SMARTS
3368.759	0.66	-0.888 ± 0.023	1.445 ± 0.034	1.251 ± 0.026	-0.021 ± 0.005	SMARTS
3393.988	3.54	-0.867 ± 0.009	1.690 ± 0.012	1.245 ± 0.009	0.032 ± 0.004	MDM

(cont'd)

Table 6.3. PG1115+080 Optical Light Curves

Table 6.3—Continued

HJD	$\chi^2/N_{def}$	Images A1+A2	Image B	Image C	$\langle \text{Stars} \rangle$	Source
3394.754	0.80	$-0.870 \pm 0.015$	$1.531 \pm 0.019$	$1.117 \pm 0.031$	$-0.040 \pm 0.005$	SMARTS
3403.785	1.00	$-0.850 \pm 0.011$	$1.555 \pm 0.014$	$1.199 \pm 0.011$	$-0.011 \pm 0.004$	SMARTS
3413.792	2.84	$-0.850 \pm 0.009$	$1.694 \pm 0.014$	$1.286 \pm 0.011$	$0.001 \pm 0.004$	SMARTS
3417.760	1.55	$-0.832 \pm 0.009$	$1.637 \pm 0.013$	$1.307 \pm 0.015$	$-0.019 \pm 0.004$	SMARTS
3424.727	0.60	$-0.818 \pm 0.022$	$1.672 \pm 0.035$	$1.216 \pm 0.038$	$-0.026 \pm 0.005$	SMARTS
3428.737	1.19	$-0.791 \pm 0.014$	$1.709 \pm 0.024$	$1.354 \pm 0.031$	$-0.042 \pm 0.005$	SMARTS
3431.786	1.51	$-0.836 \pm 0.014$	$1.772 \pm 0.020$	$1.282 \pm 0.014$	$-0.030 \pm 0.005$	SMARTS
3433.726	1.44	$-0.832 \pm 0.010$	$1.689 \pm 0.015$	$1.230 \pm 0.011$	$-0.009 \pm 0.004$	SMARTS
3435.754	1.71	$-0.830 \pm 0.008$	$1.634 \pm 0.013$	$1.224 \pm 0.010$	$0.006 \pm 0.004$	SMARTS
3442.691	2.05	$-0.833 \pm 0.011$	$1.607 \pm 0.015$	$1.245 \pm 0.011$	$-0.010 \pm 0.004$	SMARTS
3445.734	2.31	$-0.845 \pm 0.009$	$1.696 \pm 0.015$	$1.254 \pm 0.011$	$-0.005 \pm 0.004$	SMARTS
3447.633	0.82	$-0.833 \pm 0.013$	$1.630 \pm 0.017$	$1.199 \pm 0.012$	$-0.018 \pm 0.005$	SMARTS
3449.741	1.39	$-0.823 \pm 0.010$	$1.630 \pm 0.014$	$1.232 \pm 0.011$	$-0.013 \pm 0.004$	SMARTS
3458.682	0.96	$-0.819 \pm 0.012$	$1.675 \pm 0.017$	$1.264 \pm 0.013$	$-0.032 \pm 0.005$	SMARTS
3459.599	0.81	$-0.818 \pm 0.015$	$1.604 \pm 0.020$	$1.244 \pm 0.014$	$-0.030 \pm 0.005$	SMARTS
3461.676	0.86	$-0.825 \pm 0.012$	$1.641 \pm 0.016$	$1.211 \pm 0.012$	$-0.010 \pm 0.005$	SMARTS
3468.600	2.00	$-0.828 \pm 0.009$	$1.630 \pm 0.014$	$1.253 \pm 0.011$	$-0.001 \pm 0.004$	SMARTS
3470.608	2.68	$-0.837 \pm 0.011$	$1.543 \pm 0.015$	$1.324 \pm 0.012$	$-0.006 \pm 0.004$	SMARTS
3478.556	0.83	$-0.810 \pm 0.014$	$1.595 \pm 0.018$	$1.214 \pm 0.013$	$-0.033 \pm 0.005$	SMARTS
3483.539	1.05	$-0.793 \pm 0.017$	$1.603 \pm 0.026$	$1.677 \pm 0.030$	$-0.037 \pm 0.005$	SMARTS

(cont'd)

Table 6.3—Continued

HJD	$\chi^2/N_{dof}$	Images A1+A2	Image B	Image C	$\langle \text{Stars} \rangle$	Source
3490.600	1.49	$-0.822 \pm 0.011$	$1.653 \pm 0.015$	$1.256 \pm 0.011$	$-0.013 \pm 0.004$	SMARTS
3491.594	1.34	$-0.808 \pm 0.011$	$1.688 \pm 0.015$	$1.263 \pm 0.011$	$-0.011 \pm 0.004$	SMARTS
3523.497	0.97	$-0.754 \pm 0.012$	$1.703 \pm 0.017$	$1.270 \pm 0.012$	$-0.017 \pm 0.005$	SMARTS
3527.474	1.20	$-0.761 \pm 0.011$	$1.753 \pm 0.016$	$1.318 \pm 0.012$	$-0.014 \pm 0.005$	SMARTS
3718.838	0.92	$-0.787 \pm 0.015$	$1.562 \pm 0.018$	$1.174 \pm 0.013$	$-0.024 \pm 0.005$	SMARTS
3737.018	4.71	$-0.885 \pm 0.004$	$1.434 \pm 0.007$	$1.127 \pm 0.007$	$0.099 \pm 0.004$	MDM
3750.790	0.68	$-0.795 \pm 0.022$	$1.663 \pm 0.035$	$1.331 \pm 0.026$	$-0.030 \pm 0.005$	SMARTS
3755.748	0.63	$-0.784 \pm 0.023$	$1.613 \pm 0.037$	$1.186 \pm 0.024$	$-0.020 \pm 0.005$	SMARTS
3761.765	1.09	$-0.820 \pm 0.010$	$1.579 \pm 0.013$	$1.183 \pm 0.010$	$0.005 \pm 0.004$	SMARTS
3772.763	1.71	$-0.828 \pm 0.009$	$1.547 \pm 0.013$	$1.175 \pm 0.010$	$0.007 \pm 0.004$	SMARTS
3792.766	2.47	$-0.845 \pm 0.011$	$1.706 \pm 0.017$	$1.240 \pm 0.012$	$-0.006 \pm 0.004$	SMARTS
3815.678	1.48	$-0.851 \pm 0.010$	$1.721 \pm 0.017$	$1.116 \pm 0.012$	$-0.012 \pm 0.005$	SMARTS
3823.631	2.25	$-0.885 \pm 0.013$	$1.646 \pm 0.018$	$1.228 \pm 0.013$	$-0.016 \pm 0.005$	SMARTS

(cont'd)

Table 6.3—Continued

HJD	$\chi^2/N_{dof}$	Images A1+A2	Image B	Image C	$\langle \text{Stars} \rangle$	Source
3855.526	0.59	$-0.883 \pm 0.030$	$1.522 \pm 0.058$	$0.996 \pm 0.051$	$0.023 \pm 0.006$	SMARTS
3884.450	1.00	$-0.908 \pm 0.019$	$1.502 \pm 0.024$	$1.118 \pm 0.024$	$-0.033 \pm 0.005$	SMARTS
3893.475	0.64	$-0.921 \pm 0.025$	$1.655 \pm 0.035$	$1.130 \pm 0.022$	$-0.032 \pm 0.005$	SMARTS
3900.490	0.94	$-0.919 \pm 0.012$	$1.548 \pm 0.017$	$1.159 \pm 0.012$	$-0.023 \pm 0.005$	SMARTS

Note. — HJD is the Heliocentric Julian Day  $-2450000$  days. The goodness of fit of the image,  $\chi^2/N_{dof}$ , is used to rescale the formal uncertainties by a factor of  $(\chi^2/N_{dof})^{1/2}$ . The Image columns give the magnitudes of the quasar images relative to the comparison stars. The magnitudes in the Images A1+A2 column use the sum of the flux from both images. The  $\langle \text{Stars} \rangle$  column gives the mean magnitude of the standard stars for that epoch relative to their mean for all epochs. All A1 and A2 magnitudes in parentheses are the sum of the flux from both images. At these epochs the fluxes could not be measured individually.

## CHAPTER 7

### PROSPECTS FOR FUTURE WORK

#### 7.1. MULTI-WAVELENGTH MONITORING AND QUASAR EMISSION PROFILES

The quasar accretion disk - black hole mass relation presented in Chapter 5 is merely a first step. We are currently using RETROCAM on the MDM 2.4m telescope to collect  $g$ -,  $r$ -,  $i$ - and  $z$ -band data and ANDICAM on the SMARTS 1.3m telescope to collect  $B$ -,  $V$ -,  $R$ -,  $I$ -, and  $J$ -band monitoring data in  $\sim 30$  lenses. Additionally, we have just begun to monitor a number of northern systems in the  $R$ -band on the USNO Flagstaff 61 inch telescope, and we plan to expand this monitoring program to the near infrared (NIR) ( $J$ -,  $H$ - and  $K$ -bands) during the next year. Analysis of microlensing in multiple wavelength bands will yield accretion disk size measurements at the temperatures corresponding to the redshifted center of each monitoring band. Multiple ( $\gtrsim 3$ ) such measurements in one system permit a fit to the temperature profile. While the slope of the  $R_{2500} - M_{BH}$  relation provides some independent support for the  $T \propto R^{-3/4}$  temperature profile of Shakura &

Sunyaev (1973) (see Fig. 5.1), the large uncertainties certainly leave room for other spectral slopes. Poindexter, Morgan & Kochanek (2008) performed a detailed multi-wavelength analysis in the lens HE 1104–1805 and found a temperature profile  $T \propto R^{-\beta}$  where  $\beta = 0.61^{+0.21}_{-0.17}$ , supporting the findings of Francis et al. (1991) that typical quasar temperature profiles are shallower ( $\beta \approx 1/2$ ) than predicted by thin disk theory. Furthermore, the disagreement between thin disk sizes based on flux measurements and the sizes from microlensing in all systems except QJ 0158–4325 (see Figure 5.3) also suggests that the  $\beta = 3/4$  temperature profile is probably too steep for most accretion disks. Multi-wavelength analysis of an ensemble of systems will help to resolve this discrepancy.

## 7.2. THE STRUCTURE OF QUASAR X-RAY EMISSION REGIONS

In Chapter 6, we presented a measurement of the size of the X-ray continuum emission region in one lensed quasar, PG 1115+080. We plan to use the the single-epoch or sparse *Chandra* imagery from Pooley et al. (2007) in conjunction with our optical monitoring data to make a similar measurement in  $\sim 12$  systems. This set of measurements will provide a completely new constraint for quasar X-ray emission models. Previously, a plausible X-ray emission model needed only to reproduce the observed luminosity and spectral slope of a given quasar, leaving room for a variety of emission modes. Observational constraints on the size will likely

rule out entire categories of emission models, and will enable new progress toward an accretion disk model which reproduces the full spectral energy distribution of quasars.

### 7.3. THE MASS PROFILES OF LENS GALAXIES

Time delays from gravitationally lensed quasars cannot be used to measure the Hubble constant  $H_0$  unless the distribution of mass in the lens galaxy is known. Specifically, the surface density  $\kappa$  in the annulus between the images must be accurately measured (Kochanek 2002). Fitting the lens astrometry and photometry alone leaves several degrees of freedom in the lens galaxy mass model, and this degeneracy must be broken by some independent measurement. Lens galaxy velocity dispersion (e.g. Tonry 1998; Romanowsky & Kochanek 1999; Treu & Koopmans 2002, 2004; Treu et al. 2006; Jiang & Kochanek 2007) and weak lensing (e.g. Guzik & Seljak 2002; Gavazzi et al. 2007) measurements have been used to constrain some lens galaxy mass models, but the application of these constraints to some lenses (e.g. PG 1115+080) has lead to conflicting results, possibly because of problems in the measurements (see § 6.4). We have demonstrated that with sufficient monitoring data, especially at multiple wavelengths, our microlensing analysis technique can be used to discriminate between lens galaxy mass models. Given an accurate measurement of the local stellar surface density fraction  $\kappa_*/\kappa$ , a quasar time delay

can be used to measure the Hubble constant. Such measurements may also serve to resolve conflicts between time delays and stellar velocity dispersions.

## BIBLIOGRAPHY

- Adelman-McCarthy, J. et al. 2006, *ApJS*, 162, 38
- Alcock, C. et al. 1995, *AJ*, 109, 1653
- Alcock, C. et al. 2000, *ApJ*, 542, 281
- Ballantyne, D.R., Turner, N.J. & Young, A.J. 2005, *ApJ*, 619, 1028
- Beaulieu, J.-P. et al. 2006, *Nature*, 439, 437
- Bigelow, B.C., Dressler, A.M., Schechtman, S.A. & Epps, H.W. 1999, *SPIE*, 3355, 12
- Blackburne, J.A., Pooley, D. & Rappaport, S. 2006, *ApJ*, 640, 569
- Blaes, O. 2007, in *ASP Conf. Ser. 373, The Central Engine of Active Galactic Nuclei*, ed. L.C. Ho & J.-M. Wang (San Francisco: ASP), 75
- Bonning, E.W., Cheng, L., Shields, G.A., Salviander, S. & Gebhardt, K. 2007, *ApJ*, 659, 211
- Burud, I., Magain, P., Sohy, S. & Hjorth, J. 2001, *A&A*, 380, 805
- Browne, I.W.A., et al. 2003, *MNRAS*, 341, 13
- Cackett, E.M., Horne, K. & Winkler, H. 2007, *MNRAS*, in press (astro-ph/07061464)
- Chang, K. & Refsdal, S. 1979, *Nature*, 282, 561
- Chartas, G., Agol, E., Eracleous, M., Garmire, G., Bautz, M.W., & Morgan, N.D. 2002, *ApJ*, 568, 509
- Chartas, G., Eracleous, M., Dai, X., Agol, E., & Gallagher, S. 2007, *ApJ*, 661, 678
- Chiba, M., Minezaki, T., Kashikawa, N., Katata, H. & Inoue, K.T. 2005, *ApJ*, 627, 53
- Collin, S., Boisson, C., Mouchet, M., Dumont, A.-M., Coupé, S., Porquet, D. & Rokaki, E. 2002, *A&A*, 388, 771

- Courbin, F., Magain, P., Keeton, C.R., Kochanek, C.S., Vanderriest, C., Jaunsen, A.O. & Hjorth, J. 1997, A&A, 324, L1
- Dai, X., Chartas, G., Agol, E., Bautz, M.W., & Garmire, G.P. 2003, ApJ, 589, 100
- Dai, X. Kochanek, C.S., Chartas, G., Morgan, N.D. Morgan, C.W. & Garmire, G.P.. 2008, in preparation
- Dalal, N. & Kochanek, C.S. 2002, ApJ, 572, 25
- De Villiers, J.-P., Hawley, J.F. & Krolik, J.F. 2003, ApJ, 599, 1238
- DePoy, D.L., Atwood, B., Belville, S.R., Brewer, D.F., Byard, P.L., Gould, A., Mason, J.A., O'Brien, T.P., Pappalardo, D.P., Pogge, R.W., Steinbrecher, D.P., & Tiega, E.J., 2003, SPIE, 4841, 827
- Derue, F., et al. 1999, A&A, 351, 87
- Dyson, F.W., Eddington, A.S. & Davidson, C.R. 1920, MmRAS, 62, 291
- Eigenbrod, A., Courbin, F., Dye, S., Meylan, G., Sluse, D., Saha, P., Vuissoz, C. & Magain, P. 2006, A&A, 451, 747
- Einstein, A. 1916, Annalen der Physik, 49, 769
- Elíasdóttir, Á., Hjorth, J., Toft, S., Burud, I. & Paraficz, D. 2006, ApJS, 166, 443
- Fabian, A.C., Nandra, K., Reynolds, C.S., Brandt, W.N. Otani, C., Tanaka, K. Inoue, H. & Iwasawa, K. 1995, MNRAS, 277, L11
- Fabian, A.C. Vaughan, S., Nandra, K., Iwasawa, K., Ballantyne, D.R., Lee, J.C., De Rosa, A., Turner, A., Young, A.J. 2002, MNRAS, 335, L1
- Falco, E.E. et al. 1999, ApJ, 523, 617
- Falco, E.E., et al. 2001, in ASP Conf. Ser. 237, Gravitational Lensing: Recent Progress and Future Goals, Ed. T.G. Brainerd & C.S. Kochanek (San Francisco: ASP), 25
- Fohlmeister, J. et al. 2007, ApJ, 662, 62
- Francis, P.J., Hewett, P.C., Foltz, C.B, Chaffee, F.H., Weymann, R.J. & Morris, S.L. 1991, ApJ, 373, 465
- Freedman, W. et al., 2001, ApJ, 553, 47
- Fukugita, M., Ichikawa, T., Gunn, J.E., Doi, M., Shimasaku, K. & Schneider, D.P. 1996, AJ, 111, 1748

- Gao, L., White, S.D.M., Jenkins, A., Stoehr, F. & Springel, V. 2004, MNRAS, 355, 819
- Gammie, C.F. 1999, ApJ, 522, L57
- Gavazzi, R., Treu, T., Rhodes, J.D., Koopmans, L.V.E., Bolton, A.S, Burles, S. Massey, R.J., Moustakas, L.A. 2007, ApJ, 667, 176
- Gaynullina, E.R. et al. 2005, A&A, 440, 53
- Ghisellini, G. Haardt, F. & Matt, G. 2004, A&A, 413, 535
- Gould, A. 2000, ApJ, 535, 928
- Gould, A. et al. 2006, ApJ, 644, L37
- Grandi, S.A. 1982, ApJ, 255, 25
- Greene, J.E. & Ho, L.C. 2006, ApJ, 641, L21
- Guzik, J. & Seljak, U. 2002, MNRAS, 335, 311
- Haardt, F. & Maraschi, L. 1991, ApJ, 380, L51
- Haardt, F. & Maraschi, L. 1993, ApJ, 413, 507
- Hawley, J.F. & Balbus, S.A. 2002, ApJ, 573, 738
- Hirose, S., Krolik, J.H., De Villiers, J.-P. & Hawley, J.F. 2004, ApJ, 606, 1083
- Hirose, S., Krolik, J.H. & Stone, J.M. 2006, ApJ, 640, 901
- Hubeny, I., Agol, E., Blaes, O. & Krolik, J.H. 2000, ApJ, 533, 710
- Hubeny, I., Blaes, O., Krolik, J.H & Agol, E. 2001, ApJ, 559, 680
- Hubeny, I. & Hubeny, V. 1997, ApJ, 484, L37
- Huchra, J., Gorenstein, M., Kent, S., Shapiro, I., Smith, G., Horine, E. & Perley, R. 1985, AJ, 90, 691
- Impey, C.D., Falco, E.E., Kochanek, C.S., Lehár, J., McLeod, B.A., Rix, H.-W., Peng, C.Y. & Keeton, C.R. 1998, ApJ, 509, 551
- Inada, N., et al. 2003, AJ, 126, 666
- Irwin, M.J., Webster, R.L., Hewett, P.C., Corrigan, R.T & Jedrzejewski, R.I. 1989, AJ, 98, 1989

- Iwasawa, K., Fabian, A.C., Young, A.J., Inoue, H. & Matsumoto, C. 1999, MNRAS, 306, L19
- Iwasawa, K., Lee, J.C., Young, A.J., Reynolds, C.S. & Fabian, A.C. 2004, MNRAS, 347, 411
- Jiang, G. & Kochanek, C.S. 2007, ApJ, 671, 1568
- Jovanović, P., Zakharov, A.F., Popović, L.Č, Petrović, T. 2008, MNRAS, in press (astro-ph/08014473)
- Kaspi, S. Smith, P.S., Netzer, H., Maoz, D., Jannuzi, B.T. & Giveon, U. 2000, ApJ, 553, 631
- Kayser, R. Refsdal, S. & Stabell, R. 1986, A&A, 166, 36
- Keeton, C.R. 2001, preprint, [astro-ph/0102340]
- Keeton, C.R., Gaudi, B.S., & Petters, A.O. 2005, ApJ, 635, 35
- Keeton, C. R., Burles, S., Schechter, P.L. & Wambsganss, J. 2006, ApJ, 639, 1
- Klypin, A., Kravtsov, A.V., Valenzuela, O. & Prada, F. 1999, ApJ, 522, 8
- Kochanek, C.S., 2002, ApJ, 578, 25
- Kochanek, C.S. 2004, ApJ, 605, 58
- Kochanek, C.S., 2005, Strong Gravitational Lensing, Part 2 of Gravitational Lensing: Strong, Weak & Micro, Proceedings of the 33rd Saas-Fe Advanced Course, G. Meylan, P. Jetzer & P. North, eds. (Springer Verlag: Berlin) [astro-ph/0407232]
- Kochanek, C.S. & Dalal, N. 2004, ApJ, 610, 69
- Kochanek, C.S., Dai, X., Morgan, C.W., Morgan, N.D., Poindexter, S.A., Chartas, G. 2007, in ASP Conf. Series 371, Statistical Challenges in Astronomy IV, ed. G.J. Babu & E.D. Feigelson, (San Francisco:ASP), 43
- Kochanek, C.S., Keeton, C.R. & McLeod, B.A. 2001 ApJ, 547, 50
- Kochanek, C.S., Morgan, N.D., Falco, E.E. McLeod, B.A., Winn, J. Demibicky, J. & Ketzeback, B. 2006, ApJ, 640, 47
- Kogut, A., et al. 1993, ApJ, 419, 1
- Kollmeier, J.A. et al. 2006, ApJ, 648, 128
- Koratkar, A & Blaes, O. 1999, PASP, 111, 1

- Lee, J.C., Iwasawa, K, Houck, J.C., Fabian, A.C., Marshall, H.L. & Canizares, C.R. 1999, ApJ, 570, L47
- Lehár, J., Falco, E.E, Kochanek, C.S., McLeod, B.A., Impey, C.D., Rix, H.-W., Keeton, C.R. & Peng, C.Y. 2000, ApJ, 536, 584
- Li, L.-X., Zimmerman, E.R., Narayan, R. & McClintock, J.E. 2005, ApJS, 157, 335
- Maraschi, L. & Tavecchio, F. 2003, ApJ, 593, 667
- Martocchia, A., Matt, G. & Karas, V. 2002, A&A, 383, L23
- Matheson, T., et al. 2003, ApJ, 599, 394
- McLure, R.J. & Jarvis, M.J. 2002, MNRAS, 337, 109
- Merloni, A. 2003, MNRAS, 341, 1051
- Moore, B., Ghigna, S., Governato, F., Lake, G., Quinn, T., Stadel, J. & Tozzi, P. 1999, ApJ, 524, L19
- Morgan, C.W., Byard, P.L., DePoy, D.L., Derwent, M., Kochanek, C.S., Marshall, J.L., O'Brien, T.P. & Pogge, R.P. 2005, AJ, 129, 2504
- Morgan, C.W., Kochanek, C.S. Morgan, N.D. & Falco, E.E. 2006, ApJ, 647, 874
- Morgan, C.W., Kochanek, C.S., Morgan, N.D. & Falco, E.E. ApJ, submitted, [astro-ph/07070305]
- Morgan, N.D., Caldwell, J.A.R., Schechter, P.L., Dressler, A., Egami, E. & Rix, H.-W. 2004, AJ, 127, 2617
- Morgan, N.D., Dressler, A., Maza, J., Schechter, P.L. & Winn, J.N. 1999, AJ, 118, 1444
- Mortonson, M.J., Schechter, P.L. & Wambsganss, J. 2005, ApJ, 628, 594
- Myers, S.T. 2003, MNRAS, 341, 1
- Narayan, R., Barret, D. & McClintock, J.E. 1997, ApJ, 482, 448
- Nayakshin, S., Cuadra, J. & Sunyaev, R. 2004, A&A, 413, 173
- Netzer, H & Wills, B. 1983, ApJ, 275, 445
- Navarro, J.F. Frenk, C.S. & White S.D.M. 1996, ApJ, 462, 563
- Ofek, E.O. & Maoz, D. 2003, ApJ, 594, 101

- Ofek, E.O., Maoz, D., Rix, H.-W., Kochanek, C.S., & Falco, E.E. 2005, ApJ, submitted, [astro-ph/0510465]
- Oguri, M. 2007, ApJ, 660, 1
- Onken, C.A. et al. 2004, ApJ, 615, 645
- Page, D.N. & Thorne, K.S. 1974, ApJ, 191, 499
- Paraficz D., Hjorth J., Burud I., Jakobsson P., Elíasdóttir Á. 2006, A&A, 455, L1
- Peng, C.Y., Impey, C.D., Rix, H.-W., Kochanek, C.S., Keeton, C.R., Falco, E.E., Lehár, J. & McLeod, B.A. 2006, ApJ, 649, 616
- Peterson, B.M., et al. 2004, ApJ, 613, 682
- Poindexter, S. Morgan, N.D., Kochanek, C.S. & Falco, E.E 2007, ApJ, 660, 146
- Poindexter, S. Morgan, N.D. & Kochanek, C.S. 2008, ApJ, 673, 34
- Pooley, D., Balckburne, Jeffrey, A., Rappaport, S., Schechter, P.L. & Fong, W.-F. 2006, ApJ, 648, 67
- Pooley, D., Blackburne, J. A., Rappaport, S. & Schechter, P.L. 2007 ApJ, 661, 19
- Rauch, K.P. & Blandford, R.D. 1991, ApJ, 381, L39
- Refsdal, S. 1964, MNRAS, 128,307
- Richards, G.T., et al. 2004, ApJ, 610, 679
- Romanowsky, A.J. & Kochanek, C.S. 1999, ApJ, 516, 86
- Romanowski, A.J., Douglas, N.G., Arnaboldi, W. Kuijken, K., Merrifield, M.R., Napolitano, N.R., Capaccioli, M. & Freeman, K.C. 2003, Science, 301, 1696
- Rusin, D., Kochanek, C.S., Falco, E.E., Keeton, C.R., McLeod, B.A., Impey, C.D., Lehár, J., Muñoz, J.A., Peng, C.Y., Rix, H.-W. 2003, ApJ, 587, 143
- Rusin, D. & Kochanek, C.S. 2005, ApJ, 623, 666
- Saha, P, Coles, J., Macció, A.V. & Williams, L.L.R. 2006, ApJ, 650, L17
- Schechter, P.L. et al. 1997, ApJ, 475, L85
- Schechter, P. L., & Wambsganss, J. 2002, ApJ, 580, 685
- Schechter, P.L., et al. 2003, ApJ, 584, 657

- Schmidt, M. 1963, *Nature*, 197, 1040
- Schneider, P., Ehlers, J. & Falco, E.E. 1992, *Gravitational Lenses* (Berlin:Springer)
- Sergeev, S.G., Doroshenko, V.T., Golubinskiy, Y.V., Merkulova, N.I. & Sergeeva, E.A. 2005, *ApJ*, 622, 129
- Shakura, N.I. & Sunyaev, R.A., *A&A*, 24, 337
- Smith, A.J., et al. 2002, *AJ*, 123, 2121
- Sugai, H. et al. 2007, *ApJ*, 660, 1016
- Sun, W.-H. & Malkan, M.A. 1989, *ApJ*, 346, 68
- Taylor, J.E. & Babul, A. 2005, *MNRAS*, in press
- Tonry, J.L. 1998, *AJ*, 115, 1
- Treu, T. & Koopmans, L.V.E. 2002, *MNRAS*, 337, 6
- Treu, T. & Koopmans, L.V.E. 2004, *ApJ*, 611, 739
- Treu, T., Koopmans, L.V.E., Bolton, A.S., Burles, S., & Moustakas, L.A. 2006, *ApJ*, 640, 662
- Udalski, A., Kubiak, M. & Szymanski, M. 1997, *Acta Astron.*, 47, 319
- Vanden Berk, D.E. et al. 2004, *ApJ*, 601, 692
- Vaughan, S., Fabian, A.C., & Nandra, K. 2003, *MNRAS*, 339, 1237
- Vestergaard, M. & Peterson, B.M. 2002, *ApJ*, 641, 689
- Vuissoz, C. et al. 2007, *A&A*, 464, 845
- Walsh, D., Carswell, R.F. & Weymann, R.J. 1979, *Nature*, 279, 381
- Wambsganss, J. 2006, in *Saas-Fee Advanced Course 33, Gravitational Lensing: Strong, Weak and Micro*, ed. G. Meylan, P. Jetzer. & P. North, (Berlin:Springer), 453
- Wambsganss, J., Paczyński, B. & Schneider, P. 1990, *ApJ*, 358, L33
- Weymann, et al. 1980, *Nature*, 285, 641
- White, S.D.M & Rees M.J. 1978, *MNRAS*, 183, 341
- Winn, J.N., Rusin, D. & Kochanek, C.S. 2004, *Nature*, 6975, 613

- Wisotzki, L., Koehler, T., Kayser, R & Reimers, D. 1993, *A&A*, 278, L15
- Wyithe J. S. B., Turner E. L. 2001, *MNRAS*, 320, 21
- Wyrzykowski, L. et al. 2003, *Acta. Astron.*, 53, 229
- Yee, H.K.C. & De Robertis, M.M. 1991, *ApJ*, 381, 386
- Yoo, J. Kochanek., C.S., Falco, E.E. & McLeod, B.A. 2006, *ApJ*, 642, 22
- York, D.G., Adelman, J., Anderson, J.E., et al. 2000, *AJ*, 120, 1579
- Young, A. & Reynolds, C.S. 2000, *ApJ*, 529, 101
- Zentner, A.R., Berlind, A.A., Bullock, J.S., Kravtsov, A.V. & Wechsler, R.S. 2005, *ApJ*, 625, 505